Cosmological beam plasma instabilities

by

Mohamad Shalaby

A thesis
presented to the University of Waterloo
in fulfillment of the
thesis requirement for the degree of
Doctoral of Science
in
Physics

Waterloo, Ontario, Canada, 2017

Examining Committee Membership

The following served on the Examining Committee for this thesis. The decision of the Examining Committee is by majority vote.

- External Examiner: Professor Anatoly Spitkovsky
- Supervisors: Professors Avery Broderick and Niayesh Afshordi
- Internal Members: Professors Brian McNamara and James Taylor
- Internal-external Member: Professor Francis Poulin

This thesis consists of material all of which I authored or co-authored: see Statement of Contributions included in the thesis. This is a true copy of the thesis, including any required final revisions, as accepted by my examiners.

I understand that my thesis may be made electronically available to the public.

Statement of Contributions

This dissertation is partially the product of co-authored publications:

- Chapter 2 and parts of Chapter 1 are base on:
  Shalaby, M., Broderick, A.E., Chang, P., Pfrommer, C., Lamberts, A. and Puchwein, E., "SHARP: Spatially Higher-order Accurate, Relativistic PIC code", *ApJ* 841 52

- Chapter 3 is based on:
  Shalaby, M., Broderick, A.E., Chang, P., Pfrommer, C., Lamberts, A. and Puchwein, E., "Importance of resolving the spectral support of beam-plasma instabilities in simulations", arXiv:1704.00014

Abstract

Blazars are the main source of extragalactic very high energy gamma-rays. These gamma rays annihilate on the extragalactic background light, producing electron-positron pair beams with TeV energies. The pair beams are very dilute, with beam-IGM density ratio of $\alpha \sim 10^{-15}$, ultra-relativistic, $\gamma \sim 10^6$, and energetically subdominant ($\gamma\alpha \sim 10^{-9}$). Such pair beams suffer from prevailing cosmological scale, linear beam-plasma instabilities. The associated instability growth rates suggest that at least initially these overwhelmingly dominate inverse Compton cooling, currently the only alternative mechanism by which the pair beams lose energy. Therefore, the full non-linear evolution of the instabilities is key to determining the mechanism by which these pair-beams lose their energy. Kinetic numerical simulations are the only method by which we can currently study the full non-linear evolution of the blazar-induced beam-plasma instabilities. However, the extreme parameters of the pair beams make direct simulations via existing particle-in-cell (PIC) codes infeasible.

To address this, we developed a new Spatially Higher-order Accurate, Relativistic PIC algorithm (SHARP). A one dimensional implementation of the SHARP algorithm (SHARP-1D) is given in detail. We show explicitly that SHARP-1D can overcome a number of the limitations of existing PIC algorithms.

Using SHARP-1D, we demonstrate a number of points that are important to correctly simulate the full evolution of beam-plasma instabilities. We show that convergence for PIC algorithms requires increasing both spatial resolution and the number of particles per cell concurrently. For a beam-plasma system, we show that the spectral resolution is another important resolution criteria and under-resolved simulations can lead to erroneous physical conclusions. We quantify the required box sizes to faithfully resolve the spectral support of the instabilities. When the background plasmas contain structure, we show that a significant fraction of beam energy (similar to that in uniform plasma simulations; $\sim 20\%$) is, still, lost during the linear evolution of the electrostatic unstable modes. Compared to uniform plasma growth rates, we find lower growth rates, however, the non-uniform

systems stay longer in the linear regime. Therefore, the IGM inhomogeneities are unlikely to affect the efficiency of beam-plasma instabilities to cool the blazar-induced pair beams.

Acknowledgments

I would like to acknowledge the considerable support I received from my advisor, Avery Broderick. Through plenty of conversations we had, my understanding of physics, math and many other aspects of life are greatly deepened.

I would like to thank my collaborators, Philip Chang, Christoph Pfrommer, Astrid Lamberts and Ewald Puchwein, non of this work would have been possible without the many discussions we had.

To my parents
who give me the most support and encouragement throughout my life

Table of Contents

List of Tables

List of Figures

Chapter 1

Introduction

The TeV-bright blazars are a subclass of active galactic nuclei (AGN) which induce cosmological beam-plasma instabilities through the emission of gamma rays. These photons annihilate on the infrared-ultraviolet extra-galactic background light (EBL) producing electron/positron pair-beams which drive the growth of linearly unstable beam-plasma waves during their propagation through the ionized intergalactic medium (IGM) leading to depositing their energy as a thermal energy in the IGM. There are, however, another possible mechanism that could dominate the energy loss of these pair-beams. Through inverse Compton cascades (ICC) with the Cosmic microwave background (CMB) photons, the pair-beams could lose their energy and produce photons with GeV energies. Which of these mechanisms will dominate the cooling of the pair-beams is still a subject of debate, and each have different physical implications for the thermal history of the IGM, affecting our understanding of cosmological structure formation, interpretation of Lyα forest, etc.

The full evolution of the beam-plasma system is described by the Vlasov-Maxwell equations: a complicated system of non-linear partial differential equations. The full nonlinear solution of these is not known. However, using perturbation theory, the evolution of linear perturbations around equilibrium plasma configurations can be computed in many cases. For the beam-plasma system, these solutions show that a subset of plasma wavemodes[1] are unstable, i.e., grow exponentially fast with some rate.

The growth rates of these wavemodes depend on the parameters which characterize the equilibrium configuration of the beam-plasma system, i.e., temperatures of the plasmas, velocity of the beam, density contrast of the beam plasmas to the background plasmas. Using the fluid approximation of plasma, in Appendix B, the derivation of the dispersion

[1] In the linear regime, all plasma wavemodes evolve independently.

relation of linear perturbations in beam-plasma systems is presented. The dependence of the growth rates of the instabilities on different parameters of the equilibrium configuration is then studied.

The regime where the instabilities obtained using linear perturbation theory are valid (dictate the evolution) is called the linear phase of the beam-plasma instabilities. Due to the instabilities, however, different wavemode[2] grow exponentially and thus non-linear effects become important to the evolution of the plasmas. Non-linear effects such as wave-particles and wave-wave interactions can also be studied in such systems. However, it is much more complicated to study compared to the linear regime solutions. We show an example of this below (Section 1.3.1).

During the linear phase of beam-plasma instabilities, the rate of cooling via beam-plasma instabilities is much faster than the cooling rate via ICC (Broderick et al., 2012). Therefore, the correct evolution of these pair-beams will depend primarily on the non-linear evolution of the beam-plasma instabilities. Here we explore these two possibilities, and then argue for the dominance of the cooling via beam-plasma instabilities by showing evidence for its implications and the lack of the evidence for the implications of the ICC mechanism.

In Section 1.1, the production of pair-beams by TeV blazars is elaborated on, then we present estimates which show that the rate of energy loss due to the linear phase of plasma instabilities is, typically, much larger than the energy loss due to ICC in Section 1.2. In Section 1.3.1, we include an important non-linear effect (non-linear Landau damping) on the growth rate of the plasma instability and show that even after taking that into account, the rate of energy loss due to plasma instabilities is still typically larger than that due to ICC.

The full non-linear evolution is still a subject of debate, however, the possibility of ICC dominance in the energy loss of pair-beams can be directly checked if we search for some of its implications, e.g., extended halos of GeV photons surrounding TeV-bright blazars. In Section 1.3.2, we present a search for such halos, and show that their existence was excluded for typical cases at high significance. Studying the full non-linear evolution using analytical or semi-analytical methods (such as the one presented in Section 1.3.1) is infeasible, thus, understanding the full non-linear evolution requires numerical simulations. The simulations are typically done using the particles in cell method, we elaborate on that method and its limitations in Section 1.3.3.

[2]The unstable wavemodes in the beam plasma systems are a large zoo of modes: modes traveling in the beam direction (longitudinal modes), perpendicular to the beam (Weibel and filamentation modes), and at an angle with respect to the beam (oblique modes).

1.1 The gamma ray sky – blazars

The extra galactic gamma-ray sky at TeV energies is dominated by the unresolved emission of a subset of active galactic nuclei (AGNs) (Ackermann et al., 2016). The vast majority of them are blazars – objects with relativistic jets pointed in our direction (see, e.g., Table 5 of Ackermann et al., 2011). The relativistic jets are powered by accretion onto a central nucleus, presumably a super-massive black hole.

The propagation of the very high energy gamma rays (VHEGRs) through the cosmos has provided an invaluable means to probe the intervening universe (Gould & Schréder, 1967; Stecker et al., 1992; de Jager et al., 1994; Salamon & Stecker, 1998; Domínguez et al., 2011; Gilmore et al., 2012; Vovk et al., 2012). The mechanisms by which the VHEGRs are produced remain unclear (Mannheim, 1993; Ghisellini et al., 1998; Böttcher, 2007), and in the unified picture of AGNs[3], the emission properties depend on the orientation of the AGN relative to the line of sight (Urry & Padovani, 1995): there are two classes of AGNs that differ in their accretion modes

- Thermal/disk-dominated AGNs. In-falling matter assembles in a thin disk and radiates thermal emission with a range of temperatures. This emission is then Comptonized by a hot corona above the disk producing X-ray emission, defining the class of quasars or Seyfert galaxies.

- Non-thermal/jet-dominated AGNs. Highly energetic electrons that have been accelerated in the relativistic jet interact with the jet magnetic field and emit synchrotron radiation from the radio to X-ray regime. In addition, the same population of electrons can Compton up-scatter seed photons that are either provided by the synchrotron radiation itself or by an external photon field into the gamma-ray regime. Hence, the broadband spectral energy distribution of these objects is characterized by two peaks. This defines the class of radio-loud AGNs which can furthermore be subdivided into blazars (with the line of sight intersecting the jet opening angle) and non-aligned non-thermal dominated AGNs.

Extra-galactic VHEGR sources are observed to be strongly biased towards low redshifts, with the number of known sources peaking at a redshift of 0.1-0.2 (see, e.g., the red-shift distribution of high-synchrotron-peak sources in Ackermann et al., 2011, 2015). This is a

[3]In the unified picture, different observational classes of AGNs are a single type of physical object observed under different conditions, most popular classification is the classification based on the orientation with respect to the observer.

natural consequence of the annihilation of VHEGR on the nearly-homogeneous infrared-ultraviolet extra-galactic background light (EBL) that permeates the universe, generated by previous generations of stars and quasars (Gould & Schréder, 1967), therefore, the EBL can be probed by the propagating VHEGRs (Ackermann et al., 2012; Domínguez et al., 2011; Gilmore et al., 2012; Domínguez et al., 2013) .

When the energies of VHEGRs, E_γ, and the infrared EBL photons, $E_{\rm IR}$, exceeds the rest mass energy of $e^\pm$ in their centre of momentum frame, i.e. $E_\gamma E_{\rm IR}(1-\cos\theta) > 4m_e^2c^4$ where θ is the relative angle between the incident gamma-ray and the produced $e^\pm$ pair, an $e^\pm$ pair is produced with energy

$$E_b \approx \frac{E_\gamma}{2} \quad \text{or} \quad \gamma_b \approx \frac{E_\gamma}{2m_ec^2} \approx 10^6 \frac{E_\gamma}{\rm TeV}, \tag{1.1}$$

where γ_b is the Lorentz factor of the pair-beams and m_ec^2 is the rest mass energy of electrons. Momentum conservation, on the other hand, ensures that these ultra-relativistic pair-beams propagate in the same direction as the original VHEGRs.

The mean-free path to pair-creation, $D_{\rm pp}$, depends on both the energy and the red-shift. The higher the energy density of the EBL (which peaks near $z = 1$), the shorter the pair creation mean-free path. Thus, the dependence of $D_{\rm pp}$ on the energy of the VHEGRs and the red-shift of their source, is given by

$$D_{\rm pp}(E_\gamma, z) = 35 \left(\frac{1+z}{2}\right)^{-\zeta} \left(\frac{E_\gamma}{\rm TeV}\right)^{-1} \ {\rm Mpc}\,, \tag{1.2}$$

where $\zeta = 4.5$ for $z < 1$ and $\zeta = 0$ for $z \geq 1$ (Kneiske et al., 2004; Neronov & Semikoz, 2009). The length of pair creation mean free path and the homogeneity of EBL imply that the majority of beam-pairs are created within the intergalactic voids.

The momentum dispersion of the pair-beams ($\delta p_\perp$ and $\delta p_\parallel$ with respect to the beam-direction) is primarily set by the heating due to the pair-production, i.e., in the beam-frame the dispersion in the momenta is roughly m_ec. Thus, in the IGM frame, $\delta p_\perp/\delta p_\parallel \sim 10^{-6}(E_\gamma/{\rm TeV})^{-1}$ (see, e.g., Broderick et al., 2012). Hence, the transverse beam temperature in the IGM frame, T_b, is given by

$$k_B T_b = \frac{\delta p_\parallel}{2}\left(\frac{\delta p_\perp}{\delta p_\parallel}\right)^2 \approx 5\times 10^{-7}\left(\frac{E_\gamma}{\rm TeV}\right)^{-1} m_ec^2, \tag{1.3}$$

where k_B is the Boltzmann constant. The number density of the pair-beams, n_b, with a given energy, E_b, can be calculated by balancing the rate of the pair-production and the

rate by which they lose energy, Γ, if we assume that they reach steady state and neglect their advection (Broderick et al., 2012). This gives

$$n_b\,\Gamma = 7.88\times10^{-35}\left(\frac{1+z}{2}\right)^{3\zeta}\left(\frac{E_\gamma}{\mathrm{TeV}}\right)^{2}\left(\frac{E_\gamma L_{E_\gamma}}{10^{45}\ \mathrm{erg\ s^{-1}}}\right)\ \ \mathrm{cm^{-3}s^{-1}}, \tag{1.4}$$

where L_{E_γ} is the isotropic-equivalent luminosity (per unit energy) of a source located at a distance $D_{\rm pp}$ from the region where n_b is being calculated.

These pair-beams are very diluted compared to the free-electron number density of the IGM,

$$n_{\rm IGM} = 2.2\times10^{-7}\ (1+z)^3\ (1+\delta)\ \mathrm{cm^{-3}}, \tag{1.5}$$

where δ is the over-density. As mentioned before, the density of pair-beams depends on the rate of pair-beams energy loss, and we compute these cooling rate due to the two mechanisms in the Section 1.2.

However, using typical cooling rates for the two mechanisms discussed above, the typical values for pair-beams number density were found in Broderick et al. (2012) to be,

$$\frac{n_b}{n_{\rm IGM}} \approx 10^{-16} - 10^{-18}. \tag{1.6}$$

Therefore, the produced pair-beams form a cold, highly an anisotropic and dilute plasma beams propagating through the ionized intergalactic medium (IGM).

1.2 Fate of pair-beams

Here, we compute the energy loss due to both plasma instabilities (in the linear phase) and inverse Compton cascades. A comparison between these rates for different redshifts, IGM density and gamma-ray energies are then presented.

1.2.1 Cooling via plasma instabilities

As the pair-beams propagate through the ionized IGM, they can lose energy through collective interaction with the background plasma of the IGM via beam-plasma instabilities. The instabilities generate plasma waves in the IGM, whose energy are eventually converted to thermal energy in the background plasma.

For parameters relevant for the pair-beams, the fastest growing modes are the kinetic oblique modes (Bret et al., 2010b; Broderick et al., 2012; Chang et al., 2016): modes that propagate at an angle with respect to the pair-beams direction in the kinetic limit of the instability. The growth rate of fastest growing oblique wavemode, $\Gamma_{\rm obl}$, is given by (using Equations (1.1))

$$\Gamma_{\rm obl} \;=\; 2\times 0.34\times\gamma_b\frac{n_b}{n_{\rm IGM}}\sqrt{\frac{n_{\rm IGM}\;e^2}{m_e\epsilon_0}} \approx 4.416\times10^{10}\frac{n_b}{\sqrt{n_{\rm IGM}}}\left(\frac{E_\gamma}{\rm TeV}\right)\;{\rm cm}^{3/2}\;{\rm s}^{-1}. \tag{1.7}$$

Note, the factor of 2 above, is because the rate of energy loss is twice the rate of the instability growth, and we also assumed that the temperature of the beam at the beam frame $T_{\rm b}^{\rm com}$ is such that $k_BT_{\rm b}^{\rm com}=m_ec^2$. The number density of pair-beams depends on the cooling rate as mentioned above, therefore, setting $\Gamma=\Gamma_{\rm obl}$ in Equation (1.4), and using Equation (1.5), the cooling rate due to the linear growth rate of the oblique modes is given

$$\Gamma_{\rm obl} = 4.723\times10^{-11}(1+\delta)^{-1/4}\left(\frac{1+z}{2}\right)^{(6\zeta-3)/4}\left(\frac{E_\gamma}{\rm TeV}\right)^{3/2}\left(\frac{E_\gamma L_{E_\gamma}}{10^{45}\;{\rm erg\;s^{-1}}}\right)^{1/2}\;{\rm s}^{-1} \tag{1.8}$$

The rate of pair-beams energy loss if the plasma instabilities dominates, $\Gamma_{\rm obl}$, is a very weak function of number over-density δ, i.e., the rate of energy loss is marginally faster in low-density regions.

1.2.2 Cooling via inverse Compton scattering

The possible interaction of the pair-beams with the cosmic microwave background (CMB) photons could lead to up-scattering of some CMB photons to higher energies inducing cascades of photons with GeV energies, $E_{\rm IC}$.

The mean-free path of the scattering process is

$$D_{\rm IC}=\frac{3m_e^2c^4}{4\sigma_Tu_{\rm CMB}E_b}\approx 0.73\left(\frac{E_\gamma}{\rm TeV}\right)^{-1}(1+z)^{-4}\;\;{\rm Mpc}, \tag{1.9}$$

where σ_T is the Thompson cross section and $u_{\rm CMB}$ is the CMB energy density. Therefore, the rate by which the pair-beams inverse Compton cool, $\Gamma_{\rm IC}$, is given by

$$\Gamma_{\rm IC}\approx\frac{c}{D_{\rm IC}}=\frac{4\sigma_Tu_{\rm CMB}}{3m_ec}\gamma_b\approx 2.13\times10^{-13}\;\left(\frac{1+z}{2}\right)^4\left(\frac{E_\gamma}{\rm TeV}\right){\rm s}^{-1}. \tag{1.10}$$

The up-scattered photons energy is given by (see, e.g., Tiede et al., 2017a)

$$E_{\rm IC} \approx 2\gamma_b^2 E_{\rm CMB} \approx 2\left(\frac{E_\gamma}{\rm TeV}\right)^2\left(\frac{E_{\rm CMB}}{\rm meV}\right)\,{\rm GeV}. \tag{1.11}$$

However, these ICC multi-GeV photons have not been observed by the *Fermi* Large Area Telescope (LAT). This was then explained by the hypothesized presence of intergalactic magnetic fields (IGMFs) that would deflect the pair-beams away from our line-of-sight (see, e.g., Neronov & Vovk, 2010; Tavecchio et al., 2010, 2011; Dermer et al., 2011; Taylor et al., 2011; Takahashi et al., 2012; Dolag et al., 2011; H. E. S. S. Collaboration et al., 2014; Prokhorov & Moraghan, 2016).

An IGMF, with magnetic strength B and correlation length λ_B, deflects the pair-beams with an angle (Neronov & Semikoz, 2009)

$$\theta_{\rm def} \approx \begin{cases} \dfrac{D_{\rm IC}}{r_L} = 3.37\times10^{-2}\left(\dfrac{B}{10^{-16}G}\right)\left(\dfrac{E_\gamma}{\rm TeV}\right)^{-2}(1+z)^{-4}\ \ {\rm rad}, & \lambda_B \gg D_{\rm IC} \\ \dfrac{\sqrt{\lambda_B D_{\rm IC}}}{r_L} = 1.25\times10^{-3}\left(\dfrac{B}{10^{-16}G}\right)\left(\dfrac{E_\gamma}{\rm TeV}\right)^{-\frac{3}{2}}\left(\dfrac{\lambda_B}{\rm kpc}\right)^{\frac{1}{2}}(1+z)^{-2}\ \ {\rm rad}, & \lambda_B \ll D_{\rm IC} \end{cases} \tag{1.12}$$

out of our line-of-sight, which, in turn, reduces the GeV flux expected around TeV bright objects (see Figure 1.1 for illustration). Where the first case, $\lambda_B \gg D_{IC}$, is the approximation assuming the motion in a homogeneous magnetic field, the second case, $\lambda_B \ll D_{IC}$, corresponds to the diffusion in angle for the pair-beams, and r_L is the Larmor radius given by

$$r_L = \frac{E_b}{ecB} \approx 21.6\left(\frac{E_\gamma}{\rm TeV}\right)\left(\frac{B}{10^{-16}G}\right)^{-1}\,{\rm Mpc}. \tag{1.13}$$

Therefore, the emission of GeV photons is expected to be extended over angular size $\Theta_{\rm ext}$ given by $\Theta_{\rm ext} \approx \dfrac{\theta_{\rm def}}{D/D_{\rm pp}}$, where $D = D(z)$ is the angular diameter distance, therefore, than angular size of the extended emission is given by

$$\Theta_{\rm ext} \approx \begin{cases} 3.37\times10^{-3}\left(\dfrac{B}{10^{-16}G}\right)\left(\dfrac{E_\gamma}{\rm TeV}\right)^{-2}\left(\dfrac{D/D_{\rm IC}}{10}\right)^{-1}(1+z)^{-4}\ \ {\rm rad}, & \lambda_B \gg D_{\rm IC} \\ 1.25\times10^{-4}\left(\dfrac{B}{10^{-16}G}\right)\left(\dfrac{E_\gamma}{\rm TeV}\right)^{-\frac{3}{2}}\left(\dfrac{D/D_{\rm IC}}{10}\right)^{-1}\left(\dfrac{\lambda_B}{\rm kpc}\right)^{\frac{1}{2}}(1+z)^{-2}\ \ {\rm rad}, & \lambda_B \ll D_{\rm IC} \end{cases} \tag{1.14}$$

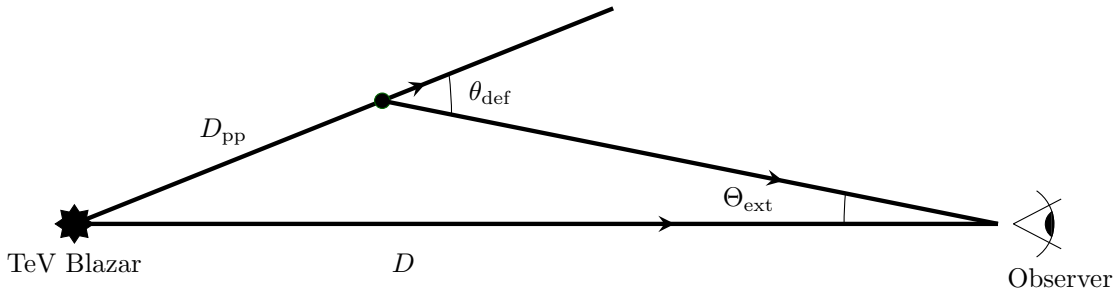

Figure 1.1 Geometry for the deflection of pair-beams by the IGMF (Neronov & Semikoz, 2009).

The absence of GeV flux can be explained if the deflection angle is bigger than the *Fermi* angular resolution (point spread function) $\theta_{\rm PSF} \sim 3.5 \times 10^{-3}$ rad, i.e., $\Theta_{\rm ext} > \theta_{\rm PSF}$. This places a lower limit on the IGMF strength, e.g., $B \gtrsim 10^{-16}$G, for $\lambda_B \gg D_{\rm IC}$, which have provided the strongest lower limits on the IGMF to date (see, e.g., for more details on this lower limit Neronov & Semikoz, 2009).

This lower limit, however, is valid only if the ICC is the dominant mechanism by which the pair-beams lose energy. If we assume the dominance of ICC, the deflection of pair-beams implies, typically, highly anisotropic halos of GeV photons around TeV bright objects which is accessible to *Fermi*-LAT. These halos extend over many degrees and, therefore, have a low surface brightness (see, e.g., Section 1.3.2).

1.2.3 Dominant mechanism for pair-beam energy loss

The ratio of the rate of energy loss due to plasma instabilities in the *linear* regime (oblique modes, $\Gamma_{\rm obl}$), to the energy loss due to inverse-Compton scattering, $\Gamma_{\rm IC}$, using Equations (1.8, 1.10), is given by

$$\frac{\Gamma_{\rm obl}}{\Gamma_{\rm IC}} \approx 233\,(1+\delta)^{-1/4}\left(\frac{1+z}{2}\right)^{(6\zeta-19)/4}\left(\frac{E_\gamma}{\rm TeV}\right)^{1/2}\left(\frac{E_\gamma L_{E_\gamma}}{10^{45}\ {\rm erg\ s^{-1}}}\right)^{1/2} \tag{1.15}$$

In Figure 1.2, the ratio $\Gamma_{\rm obl}/\Gamma_{\rm IC}$, at different red-shift is shown for a wide range of TeV energy emissions, $E_\gamma/{\rm TeV}$. The energy loss due the linear phase of the oblique modes growth is much faster than the rate due to IC scattering, for energies above TeV, this

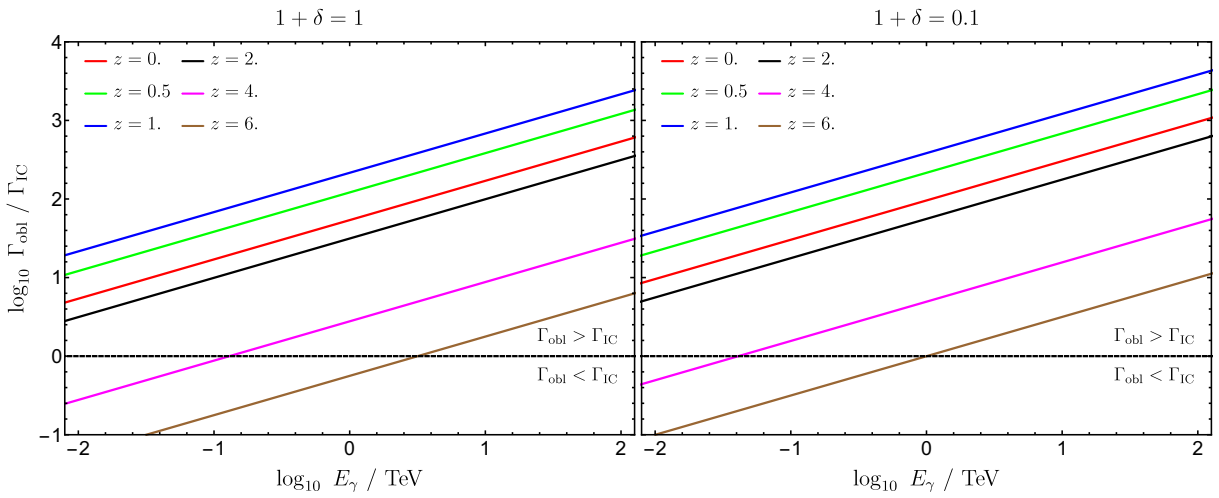

Figure 1.2 The ratio of the rate of energy loss due to plasma instability *linear* growth (oblique modes), $\Gamma_{\rm obl}$, to the energy loss due to inverse-Compton scattering, $\Gamma_{\rm IC}$, at different red-shifts. In all curves, we used $E_\gamma L_{E_\gamma} = 10^{45}$ erg s^{-1}. Left is the comparison at mean density of IGM, $1+\delta = 1$, and right is the ratio at voids, $1+\delta = 0.1$: the cooling via plasma instabilities is more effective at lower densities of IGM. At $E_\gamma =$ TeV and mean density of IGM, the energy loss via plasma instabilities (linear phase) is dominant up to $z = 4$, at lower red-shift, the energy loss via linear plasma instabilities is faster by orders of magnitude than the energy loss due to inverse-Compton scattering with CMB photons.

extends up to $z \approx 4$. At higher emission energies, this extends to even higher red-shift values ($z > 4$).

Assuming that the pair-beams loses the energy at the linear growth rates of these instabilities, this increases the temperature of the mean density IGM by nearly an order of magnitude and even more heating at lower density IGM regions. The inclusion of this heating qualitatively and quantitatively changes the structure and thermal history of the IGM. The heating deposit more energy per baryon in lower density voids, which reproduce the inverted density-temperature relation (Chang et al., 2012; Lamberts et al., 2015), inferred using high-redshift (z = 2-3) Lyα studies . In the standard reionization models, the inverted density-temperature relation has proven to be problematic (McQuinn et al., 2009; Bolton & Becker, 2009).

1.3 Probes for the beam-plasma instabilities in the non-linear regime

The dominance of the plasma instabilities energy loss rate, in the linear regime of the instabilities, guarantees the initial growth of these plasma waves, regardless of whether this dominance holds when non-linear effects on the instabilities are included. Eventually, nonlinear effects will cause these waves to saturate, limiting the ultimate energy loss rate.

It is currently unclear if this dominance continues to hold when these nonlinear effects are included. It has been argued by Broderick et al. (2012); Chang et al. (2014); Schlickeiser et al. (2013b) that the energy loss due to plasma instabilities still dominates when the non-linear effects are included, however, the opposite was also argued in (Miniati & Elyiv, 2012; Sironi & Giannios, 2014; Kempf et al., 2016).

Here we present evidences in support of the dominance of plasma instabilities in the pair-beams energy loss. We start by showing that when an important non-linear effect (Non-linear Landau damping) is included, the cooling rate of the pair-beams due to the plasma instabilities is still higher than the cooling rate due to ICC scenario for most typical cases. We then show that an important ICC implication (GeV halos around TeV bright objects) is absent in samples provided by the *Fermi* large area telescope, which provide an indirect evidence in support of the dominance of plasma instabilities scenario.

1.3.1 Higher order, perturbative calculations

Here we explore the effect of an important non-linear effect on the growth of the unstable modes: as the unstable wavemodes grow in amplitude, they become subject to nonlinear particle-wave and wave-wave interactions. The most important nonlinear interaction, here, is the induced scattering by thermal ions (Kaplan & Tsytovich, 1968; Smith & Fung, 1971; Breĭzman et al., 1972; Melrose, 1986).

Scattering of these unstable plasma wavemodes with thermal ions is called non-linear Landau damping (NLLD). This scattering leads to a change in oscillation frequencies and wave-numbers of the plasma wavemodes, i.e., changes $(\omega, \mathbf{k})$ to $(\omega^{'}, \mathbf{k}^{'})$. The kinetic equation that describe the evolution of the energy density of plasma wavemodes, when scattering off of thermal ions is included, is given by (Kaplan & Tsytovich, 1968; Breĭzman et al., 1972)

$$\frac{dW_{\mathbf{k}}}{dt} = 2\Gamma_{\mathbf{k}} W_{\mathbf{k}} - \frac{W_{\mathbf{k}}\omega_p}{8(2\pi)^{5/2} n_{\rm IGM} m_e v_{e,th}^2} \int \frac{(\mathbf{k}\cdot\mathbf{k}^{'})^2}{k^2 k^{'2}} \phi(\mathbf{k},\mathbf{k}^{'}) W_{\mathbf{k}^{'}} d\mathbf{k}^{'}, \tag{1.16}$$

$$\phi(\mathbf{k},\mathbf{k}^{'}) = \frac{3v_{e,th}^2(k^2 - k^{'2})}{4\omega_p |\mathbf{k}-\mathbf{k}^{'}| v_{i,th}} \times \exp\left[-2\left(\frac{3v_{e,th}^2(k^2-k^{'2})}{4\omega_p|\mathbf{k}-\mathbf{k}^{'}|v_{i,th}}\right)^2\right], \tag{1.17}$$

where $\Gamma_k = \Gamma_{\rm obl}(\mathbf{k}) + \Gamma_{LD}(\mathbf{k})$, where $\Gamma_{\rm LD}(\mathbf{k})$ is the linear landau damping rate for wavemode $\mathbf{k}$, $\omega_p = \sqrt{e^2 n_{\rm IGM}/m_e \epsilon_0}$ is the IGM plasma frequency, $v_{e,th}$ and $v_{i,th}$ are the thermal velocities of IGM electrons and ions, respectively and $W_{\mathbf{k}}$ is the spectral energy density of the wavemodes normalized such that the total energy density is given by

$$W = \frac{1}{(2\pi)^3} \int W_{\mathbf{k}} d\mathbf{k}. \tag{1.18}$$

This integro-differential equation (1.16) was solved numerically in Chang et al. (2014), for typical pair-beams produced by TeV-bright blazars with $E_\gamma L_{E_\gamma} = 10^{45}$ erg s^{-1} and $E_\gamma = 1$ and 10 TeV. It was found that while the instability grew slower than in the linear regime, it remained dominant. The maximum growth rate of the instability after including such scattering, $\Gamma_{\rm NL}$, was found to be

$$\Gamma_{\rm NL} \approx 8 \times 10^{-4} \Gamma_{\rm linear}, \tag{1.19}$$

where $\Gamma_{\rm linear}$ is the maximum growth rate of the oblique wavemodes in the linear regime. Using this growth rate to compute the number density of the beam (Equation 1.4), the

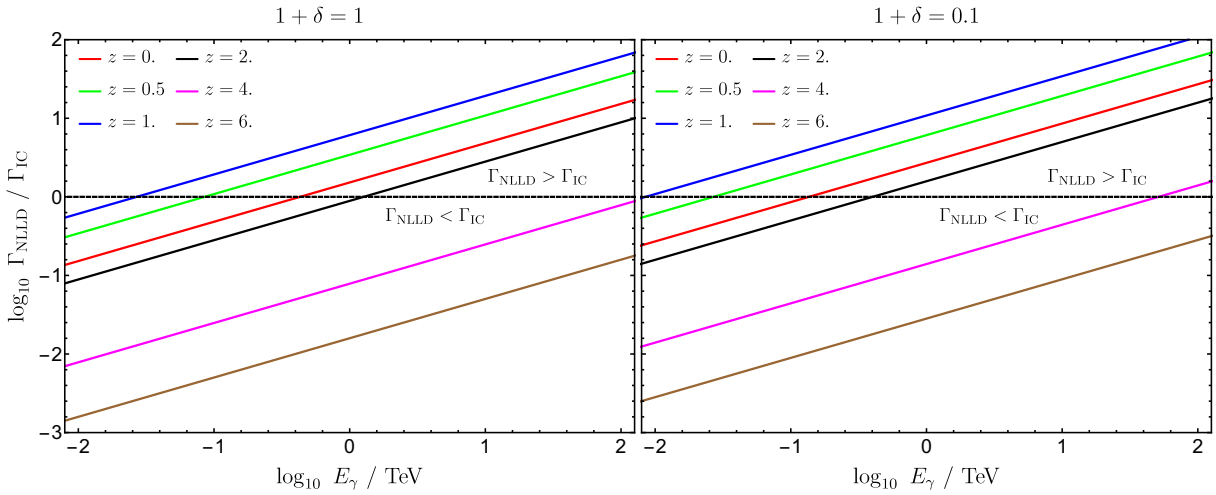

Figure 1.3 The ratio of the rate of energy loss due to plasma instability growth (oblique modes) after accounting for the non-linear landau damping effects, $\Gamma_{\rm NLLD}$ to the energy loss due to inverse-Compton scattering, $\Gamma_{\rm IC}$, at different red-shift values. In all curves, we used $E_\gamma L_{E_\gamma} = 10^{45}$ erg s^{-1}. Left is the comparison at mean density of IGM, $1+\delta = 1$, and right is the ratio at voids, $1+\delta = 0.1$: the cooling via plasma instabilities is more effective at lower densities of IGM.

rate of energy loss due to the plasma instabilities, after including NLLD effect, is given by

$$\Gamma_{\rm NLLD} \approx 1.335 \times 10^{-12} (1+\delta)^{-1/4} \left(\frac{1+z}{2}\right)^{(6\zeta-3)/4} \left(\frac{E_\gamma}{\rm TeV}\right)^{3/2} \left(\frac{E_\gamma L_{E_\gamma}}{10^{45}\ {\rm erg\ s^{-1}}}\right)^{1/2} {\rm s}^{-1}. \quad (1.20)$$

Which remains comfortably larger than the inverse Compoton cooling rate for typical TeV-bright blazars.

The ratio of energy loss rate due to plasma instabilities after including the effect of thermal ions scattering, $\Gamma_{\rm NLLD}$, to the energy loss rate due to inverse-Compton scattering, $\Gamma_{\rm IC}$ is given by (using Equations (1.10, 1.20))

$$\frac{\Gamma_{\rm NLLD}}{\Gamma_{\rm IC}} \approx 6.1\ (1+\delta)^{-1/4} \left(\frac{1+z}{2}\right)^{(6\zeta-19)/4} \left(\frac{E_\gamma}{\rm TeV}\right)^{1/2} \left(\frac{E_\gamma L_{E_\gamma}}{10^{45}\ {\rm erg\ s^{-1}}}\right)^{1/2}. \quad (1.21)$$

In Figure 1.3, the ratio $\Gamma_{\rm NLLD}/\Gamma_{\rm IC}$ is shown at different red-shift for a wide range to gamma-ray energies, E_γ/TeV. At $z = 0$ and mean density ($\delta = 0$), the energy loss

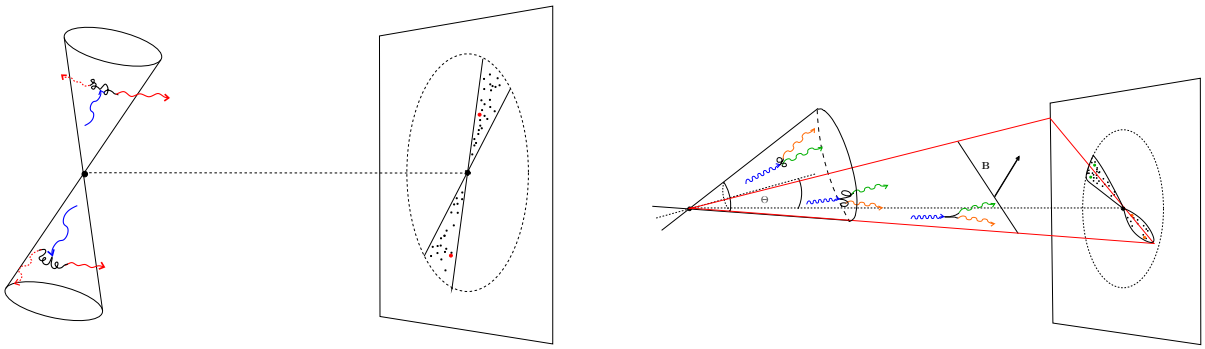

Figure 1.4 Cartoons of the mechanisms by which anisotropy in the ICC halos is generated, distinguished by the structure of the underlying IGMF. Left: For an IGMF tangled on small scales ($\lambda_B \ll 3$ Mpc) the anisotropy is due to the structure of the gamma-ray jet. Right: For an IGMF that is uniform across the gamma-ray jet (IGMF coherence length $\lambda_B \gg 100$ Mpc) the anisotropy is due to the geometry of the gyrating, relativistic pairs.

due to the ICCs are $\sim 38\%$ and 16% at 1 and 10 TeV, respectively. These values could significantly be reduced further if nonlinear wave-wave interactions reduce the effectiveness of the scattering process (Chang et al., 2014).

1.3.2 The search for inverse Compton cascade halos

The possibility of ICCs dominance in the energy loss of pair-beams can be assessed by searching for its implications. Chief among which is an extended halos of GeV photons surrounding TeV-bright blazars this occurs due to the deflection of the pair-beam. The *Fermi* large area telescope (LAT) provides data sets for bright gamma-ray bright AGNs in which these halos can be searched for. Here we elaborate on an attempt to search for such halos in a sample of objects provided by Fermi-LAT.

Generally, the halos are highly asymmetric, and in Figure 1.4, a cartoon for how such anisotropic signal is, typically, formed is shown. The asymmetric structure of the halos occurs either due to a uniform IGMF across the gamma-ray jet or, in case of small scale tangled IGMF, due to the structure of the gamma-ray jet. A quantitative description of the structure of the ICC halos in different cases was computed in (Broderick et al., 2016).

The anisotropy presents a signature that is distinct from most possible contaminants, and a statistical method based on stacking the power spectra of halos was devised in (Tiede

et al., 2017a). Sacking the power spectra of images was shown to be much more effective than simply stacking images to increase the significance of halos signal and avoid most of systematic uncertainties that comes from the *Fermi* point spread function and the spatially varying gamma-ray background (e.g., Neronov et al., 2011; Ackermann et al., 2013).

In (Tiede et al., 2017b), the method of stacking power spectra was used to look for these halos in a sample of Fermi objects: the sample was optimized to look for the anisotropic halo feature and can be found in Table 1 of (Tiede et al., 2017a). The signal for the halos is absent, and assuming a correlation length for IGMF $\lambda_B > 100$Mpc: IGMF with strengths $B = 10^{-15}$ to 10^{-16}G is shown to be excluded at greater than 3.9σ significance, and at 2σ significance, $B = 10^{-14}$ to 10^{-17}G is shown to be excluded.

The ICC mechanism also implies a redshift evolution for blazars that is very different from other AGNs. In (Broderick et al., 2014), it was shown that if the ICC mechanism do not occur, similar redshift evolution is consistent with observed *Fermi* objects, supporting the absence of ICC mechanism.

1.3.3 Numerical simulation

The particle-in-cell (PIC) method is a powerful numerical tool to study the evolution of plasmas. It is used to model plasmas ranging from laboratory experiments to astrophysical environments. First proposed in one spatial dimension (1D) by Buneman (1959) and Dawson (1962), the general idea of this algorithm is straightforward: it follows the trajectory of particles with N-body methods while solving Maxwell's equation on an Eulerian grid. The communication between grid points and particles is achieved through interpolation. The general loop (described in Figure 1.5) consists of first interpolating particle positions and velocities to a spatial grid to solve for the resulting charge and current density. Maxwell's equations are then solved on the grid with these source terms to find the self-consistent electromagnetic (electrostatic in 1D) fields. Fields are then interpolated back to the particle positions to calculate the Lorentz force, and hence, acceleration, to forward evolve the particles in time using a so-called pusher. This reduces the number of computational operations from $\sim O(N^2)$ (as the case for N-body methods) to $\sim O(N)$, where N is the number of particles in the simulation. This also results in eliminating all wavemodes in the electromagnetic fields on scales smaller than the cell-size on the grid upon which they are computed.

The limitation of such powerful numerical tool comes mainly from the lack of the conservation of phase-space distribution moments (energy, momentum and charge). This is a result of two common types of numerical instabilities present in these schemes: aliasing

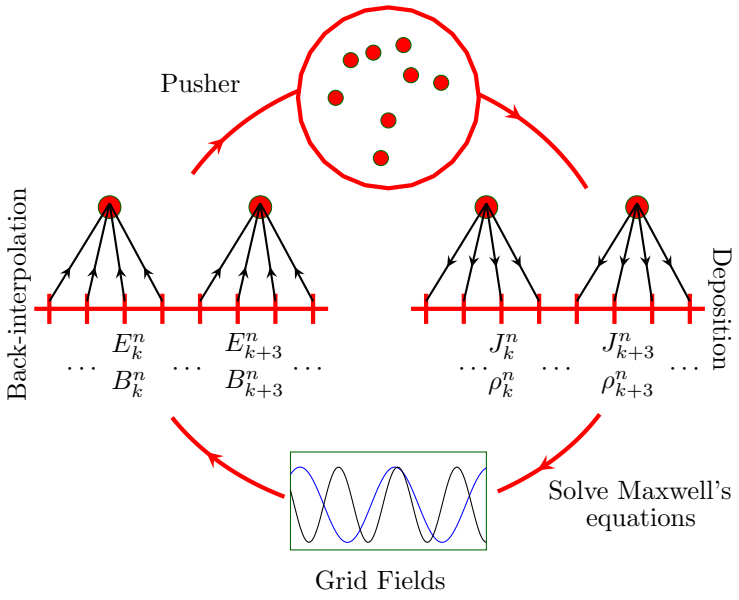

Figure 1.5 Schematic representation for the general loop in the PIC method: Starting from the three o'clock position and moving clockwise, the macro-particles' position and velocity data (x, v) are deposited onto a physical grid to construct charge and current densities (ρ_k and J_k) at control points (k) of the grid (e.g., Section 2.2.3). These are used to solve Maxwell's equations that yield the self-consistently computed (electric and magnetic) fields at these control points of the physical grid (e.g., Section 2.2.4). The updated fields are, then, back-interpolated on the macro-particles to construct the Lorentz force on macro-particles (e.g., Section 2.2.5), which is then used to evolve them via a particle pusher (e.g., Section 2.2.6).

and numerical Cerenkov instabilities. Both of these instabilities arise due to the difference in the treatments of particles (Lagrangian treatment) and fields (Eulerian treatment) in PIC schemes generally. All these issue are briefly discussed below, while discussions of how to overcome these limitations is deferred to later chapters.

Conservation of charge

Direct interpolation of particle data to construct charge and current densities on the grid, in general, leads to a violation of charge conservation, i.e., violation of the continuity equation on the grid. The reason for that is calculating the current density requires the knowledge of both particles positions and velocities at the half-time step and approximating the particles positions at half-time step leads to an error in the calculated current-density when particles cross cell-boundaries. Recently, several methods were proposed where the calculation of the current density on the grid from the particles is done such that the continuity equation is satisfied on the grid at all times (Eastwood, 1991; Villasenor & Buneman, 1992; Esirkepov, 2001; Umeda et al., 2003).

Conservation of energy and momentum

On the other had, for PIC schemes, energy and momentum conservation appear to be mutually exclusive in general (see, e.g., Brackbill, 2016).

Momentum non-conservation, typically, comes from non-vanishing self-forces and errors in the interaction forces – an example of such a case is shown in Appendix A.1.1. These non-physical forces can produce macroscopic non-physical instabilities (Langdon, 1973). Energy non-conservation can also produce dramatic changes in the evolution of the plasmas. Since such an error has a secular (unbounded) growth, energy non-conservation in PIC schemes imposes a serious limitation on the ability to study non-linear phenomena that occurs on long time scales (compared to ω_p^{-1}).

For instance, Lapenta & Markidis (2011) demonstrated that in the two-stream instability the errors in the energy are disproportionately distributed to the fast particles. That is, even though the per-particle violation in energy conservation is small, the energy error primarily affected the high energy end of the momentum distribution function. This is important for particle acceleration in relativistic situations (Lapenta & Markidis, 2011). Results that probe the long-term behavior of particle distribution functions starting from linearly unstable conditions such as tenuous beam instabilities or particle acceleration are

subject to these issues (e.g. Sironi & Giannios, 2014; Park et al., 2015; Ardaneh et al., 2015a).

A major test of the accuracy and fidelity of different PIC schemes is, thus, their ability to preserve conserved quantities such as energy, momentum and charge. Often, this is required to accurately study subdominant, relativistic populations that typically arise in astrophysical contexts. Examples include non-thermal particle populations accelerated at shocks and reconnection events (Spitkovsky, 2008; Lyutikov et al., 2016), propagation of cosmic rays (Riquelme & Spitkovsky, 2009), interaction of accretion disks and coronae (Miller & Stone, 1999), and TeV blazar driven beam instabilities (Broderick et al., 2012). In the latter, this problem is especially severe, with the beams being both numerically and energetically subdominant while being highly relativistic; even a small degree of heating in the background can impact or overwhelm the evolution of beam plasma instabilities.

Recently introduced implicit methods (Markidis & Lapenta, 2011; Chen et al., 2011; Lapenta & Markidis, 2011) can in theory preserve total energy exactly (though in practice may not), while violating momentum conservation. For computationally simpler explicit, momentum conserving, schemes, energy conservation is improved by filtering the deposited grid moments (charge and current densities) as is done in the TRISTAN-MP code (Buneman et al., 1993; Spitkovsky, 2005). However, filtering, when used with a momentum-conserving scheme, leads to a violation of momentum conservation and non-vanishing self-forces (see Appendix A.1.3). In lieu of filtering, energy conservation is also improved by using higher-order interpolation functions, which is the approach that we will use in Chapter 2 for both forward-interpolation (from particles to fields) and back-interpolation (from fields to particles) steps. This has the added advantage that momentum conservation is maintained.

Numerical instabilities

The non-conservation of energy and/or momentum conservation is related to common numerical instabilities that exit in general PIC algorithms. Typically, mitigating such instabilities improves the conservation properties of the PIC algorithms.

In 1D, the major source of that is the aliasing: the coupling between the wavemodes resolved by the grid and their aliases. Aliases of a wave mode, k, are all wavemodes that differ from k by integer number of $2\pi/\Delta x$, where Δx is the grid cell size. The reason for such coupling is that continuous particle-data (which support wavemodes that include aliases of wavemodes resolved by the grid) are used in the construction of phase-space moments at a discrete set control of points on the physical grid. This leads to virulent numerical

heating of the simulated plasmas, and the heating saturates only when the plasma Debye length becomes comparable to the grid cell size (see, e.g., Birdsall & Maron (1980)). In Chapter 2, we demonstrate that this numerical heating can almost be completely eliminated when higher order interpolation functions are used in both forward- and back-interpolation steps.

In multi-dimensional PIC algorithms, another strong numerical instability exists: the numerical Cerenkov instability (NCI), see e.g., Godfrey (1974). As we mentioned above, this arises due to the difference in the treatments of particles (Lagrangian treatment) and fields (Eulerian treatment) in PIC schemes. It occurs by the numerical (non-physical) coupling of the beam resonances and electromagnetic modes that are numerically traveling slower than the speed of light in a drifting plasma Godfrey (1975); Nuter & Tikhonchuk (2016). Techniques to mitigate and eliminate the dominant modes of NCI includes, digital filtering, using 'magical' time step and improving the numerical balancing of transverse electric and magnetic fields at smaller wave-numbers Godfrey & Vay (2014); Lehe et al. (2016); Nuter & Tikhonchuk (2016); Xu et al. (2013); Yu et al. (2015).

Chapter 2

Particle in cell algorithm in one dimension: SHARP-1D

Numerical heating in particle-in-cell (PIC) codes currently precludes the accurate simulation of cold, relativistic plasma over long periods, severely limiting their applications in astrophysical environments. We present a spatially higher order accurate relativistic PIC algorithm in one spatial dimension which conserves charge and momentum exactly. We utilize the smoothness implied by the usage of higher order interpolation functions to achieve a spatially higher order accurate algorithm (up to 5th order). We validate our algorithm against several test problems – thermal stability of stationary plasma, stability of linear plasma waves, and two-stream instability in the relativistic and non-relativistic regimes. Numerical heating in particle-in-cell (PIC) codes currently precludes the accurate simulation of cold, relativistic plasma over long periods, severely limiting their applications in astrophysical environments. We present a spatially higher order accurate relativistic PIC algorithm in one spatial dimension which conserves charge and momentum exactly. We utilize the smoothness implied by the usage of higher order interpolation functions to achieve a spatially higher order accurate algorithm (up to 5th order). We validate our algorithm against several test problems – thermal stability of stationary plasma, stability of linear plasma waves, and two-stream instability in the relativistic and non-relativistic regimes. Comparing our simulations to exact solutions of the dispersion relations, we demonstrate that SHARP can *quantitatively* reproduce important kinetic features of the linear regime. Our simulations have a superior ability to control energy non-conservation and avoid numerical heating in comparison to common second order schemes. We provide a natural definition for convergence of a general PIC algorithm: the complement of physical modes captured by the simulation, i.e., lie above the Poisson noise, must grow commensurately

with the resolution. This implies that it is necessary to simultaneously increase the number of particles per cell and decrease the cell size. We demonstrate that traditional ways for testing for convergence fail, leading to plateauing of the energy error. This new PIC code enables to faithfully study the long-term evolution of plasma problems that require absolute control of the energy and momentum conservation.

2.1 Introduction

In this chapter, we describe an implementation of the PIC algorithm in 1D that uses high-order spline functions (up to 5th order) for the forward- and back-interpolation steps of the algorithm. We couple this with an exact Poisson solver and a second order symplectic integrator, i.e., leap frog, to produce a second-order accurate code called SHARP-1D. SHARP-1D displays superior energy-conservation properties while conserving the momentum exactly. The smoothness coming from the usage of high order interpolation functions is utilized to construct up to 5th order spatially accurate algorithm.[1] Despite the high spatial order accuracy, our code remains second order accurate as it is limited by the accuracy of the particle pusher. This will be addressed in future work.

The chapter is organized as follows: in Section 2.2 we describe the basic equations of the PIC method, our choice of discretization of the equations, and discuss sources for the numerical error. After discussing the order of accuracy of the solution, we describe our choice of code units. In Section 2.3 we discuss the conservation properties of different PIC algorithms. In Section 2.4 we demonstrate the different capabilities of SHARP-1D by validating it against several test problems: thermal stability of plasma, plasma oscillation frequency and linear-Landau damping of standing plasma waves and two-stream instabilities in both relativistic and non-relativistic regimes. We compare several of the results of SHARP-1D to the results of TRISTAN-MP simulations in Section 2.5. Finally, we study the convergence properties for our algorithm in Section 2.6 and conclude in Section 3.4.

2.2 The PIC method

The evolution of the particles that comprise a plasma is described by the Boltzmann and Maxwell's equations. In the absence of collisions, the particles are described by the Vlasov

[1] Due to the usage of lower order interpolation functions, current algorithms perform the back-interpolation step with second order spatial accuracy (e.g., Haugbølle & Frederiksen, 2013; Lapenta & Markidis, 2011; Lapenta, 2016; Brackbill, 2016).

equation, which in one spatial dimension is

$$\partial_t f_s(x,u,t) + \frac{u}{\gamma}\partial_x f_s(x,u,t) + \frac{q_s E(x,t)}{m_s}\partial_u f_s(x,u,t) = 0, \tag{2.1}$$

where s denotes a particle species, characterized by its charge q_s and mass m_s, $u = \gamma v$ is the spatial component of the four-velocity, $\gamma = \sqrt{1+(u/c)^2}$ is the Lorentz factor, $E(x,t)$ is the electric field and $f_s(x,u,t)$ is the phase-space distribution functions of particles of species s.

In one dimension, Maxwell's equations imply that the magnetic field is constant and along the direction of the particle motion. Thus, it impacts the evolution of neither the particle nor the electric field, and we take it to be zero henceforth. Therefore, Maxwell's equations reduce to

$$\partial_x E(x,t) - \frac{\rho(x,t)}{\epsilon_0} = 0 \quad \text{and} \quad \partial_t E(x,t) + \frac{j(x,t)}{\epsilon_0} = 0\,, \tag{2.2}$$

where ρ and j are the charge and current densities, respectively. This set of equations is closed by the following equations for ρ and j:

$$\begin{aligned} \rho(x,t) &= \sum_s q_s \int f_s(x,u,t)du \\ j(x,t) &= \sum_s q_s \int \frac{u}{\gamma} f_s(x,u,t)du\,. \end{aligned} \tag{2.3}$$

2.2.1 Smoothing phase-space distribution functions

The distribution function for point-like particles is given by the Klimontovich distribution function:

$$f_s^K(x,u) = \sum_{i_s}^{N_s^p} \delta(x - x_{i_s})\delta(u - u_{i_s}), \tag{2.4}$$

where N_s^p is the number of physical (point-like) particles and $\delta(x)$ is the Dirac delta function.

Direct usage of this singular distribution function is impractical for two reasons: first, the number of particles to be simulated is too large to be tractable, and thus second, this distribution function would result in an overwhelming shot noise due to the finite number of particles used in practice (Lipatov, 2002). Both can be mitigated in simulations by

using a smoothed approximation for the distribution function. Thus, we approximate the distribution function by

$$f_s(x,u) \;=\; w\sum_{i_s}^{N_s} S(x-x_{i_s})\delta(u-u_{i_s}) \approx \int dx' f_s^K(x',u)S(x',x), \tag{2.5}$$

where N_s is the number of macro-particles (defined below), and $w = N_s^p/N_s$ is the number of physical particles that a macro-particle represents.

The macro-particles (also called computational particles[2]) have a "shape" $S(x, x_{i_s})$, i.e., a smoothed localized charge distribution that has w physical particles centered at x_{i_s}, with

$$\int S(x, x_{i_s})dx = 1. \tag{2.6}$$

The charge and the mass for these computational particles are $Q_s = wq_s$ and $M_s = wm_s$, respectively.

The macro-particles have the same plasma frequency ω_P as physical particle they represent in simulations: they have same charge-to-mass ratio and hence $\omega_p^2 = q_s^2 N_s^p/(Vm_s\epsilon_0) = Q_s^2 N_s/(VM_s\epsilon_0)$, where V is the volume. Both macro-particles and physical particles have, also, the same normalized temperature $\theta_s = k_B T_s/M_s c^2 = k_B T_s^p/m_s c^2$, where T_s and T_s^p are the effective temperatures of the macro-particles and physical particles, respectively. This arises from the assumption that the macro-particles are monolithic, and thus have the same *velocity* distribution as the underlying physical particles, and thus

$$\frac{k_B T_s}{M_s c^2} = \frac{\int du(\gamma-1)f_s}{\int du f_s} = \frac{\int du(\gamma-1)f_s^K}{\int du f_s^K} = \frac{k_B T_s^p}{m_s c^2}. \tag{2.7}$$

Inserting the phase-space distribution function in Equation (2.5) into the Vlasov-Maxwell system (Equations (2.1) and (2.2)), we obtain from the first two moments the following equations of motion for the macro-particle of species s:

$$\frac{dx_{i_s}}{dt} \;=\; \frac{u_{i_s}}{\gamma_{i_s}}, \quad \frac{du_{i_s}}{dt} = \frac{Q_s}{M_s}E_{i_s}, \tag{2.8}$$

$$E_{i_s} \;\equiv\; \int E(x)S(x, x_{i_s})dx, \tag{2.9}$$

[2]Both macro-particles and particles will be interchangeably used to mean the same thing: particles used in simulations. When we refer to physical particles, it will be explicitly specified.

where $E(x)$ is the solution of Maxwell's equations (2.2) with moments given by

$$\rho(x,t) = \sum_s Q_s \sum_{i_s}^{N_s} S(x, x_{i_s}), \tag{2.10}$$

$$j(x,t) = \sum_s Q_s \sum_{i_s}^{N_s} v_{i_s} S(x, x_{i_s}), \tag{2.11}$$

where $v_{i_s} = u_{i_s}/\gamma_{i_s}$. Below we explain how implicit discretization of such system of equations is achieved in our code.

2.2.2 Spatial grid

For a system of macro-particles in a periodic box (line) of length L, we divide our domain into N_c cells each of size $\Delta x = L/N_c$. Assuming $k \in \{0, 1, ..., N_c - 1\}$, we define the kth cell (c_k) centered at $x_{k+1/2} \equiv x_k + \Delta x/2$ as $x \in [x_k, x_{k+1})$, where $x_k \equiv \Delta x\, k$.

We adopt spline functions extending over a number of grid cells as the shape function of the macro-particles. Therefore, the distribution of physical particles inside these macro-particles is symmetric around their center and extends over a number of computational cells depending on the order m of the spline functions used. For instance $m = 1$ is a top-hat distribution (shape) given by

$$S(x, x_i) \to S^1\left(\frac{|x - x_i|}{\Delta x}\right) = \frac{1}{\Delta x} \begin{cases} 1, & \text{If } |x - x_i| < \Delta x/2, \\ \\ 0, & \text{otherwise.} \end{cases} \tag{2.12}$$

We also define, $t^n = n \times \Delta t$, $E^n \equiv E(t^n)$, i.e., superscript n denotes the nth time step for the particular quantity. We choose the time step Δt such that $c\Delta t \leq \Delta x$, to obey the Courant-Friedrichs-Lewy (CFL) stability condition in 1D (Courant et al., 1967).

2.2.3 Charge and current deposition

To obtain a discrete set of equations that governs the evolution of such macro-particles, we begin by integrating the first equation in (2.2) over the kth cell c_k:

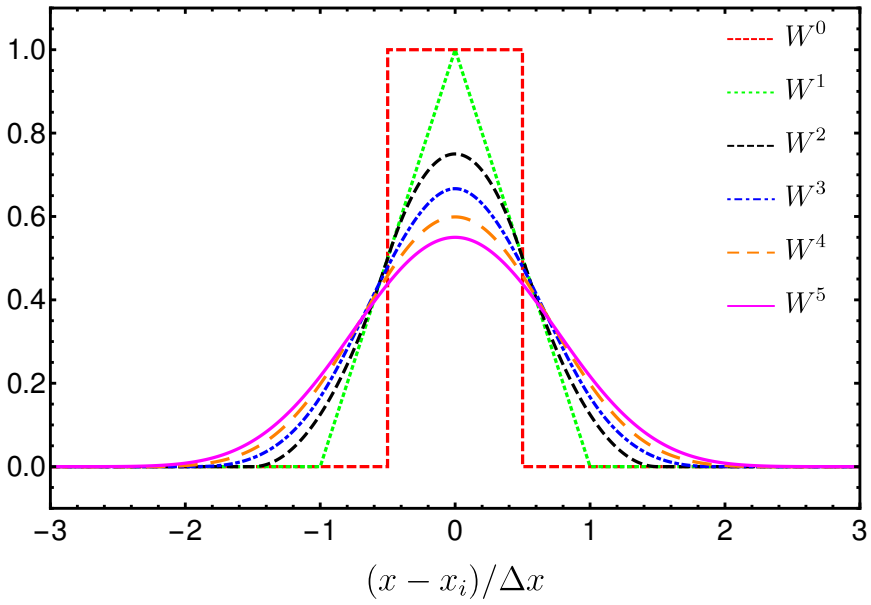

Figure 2.1 Different weight functions implemented in SHARP-1D. The relation between shape and weight functions is defined in Equation (2.15). Explicit forms for both, shape and weight functions are given in Appendix A.2.

$$E^n_{k+1} - E^n_k \;=\; \int_{c_k} \frac{\rho^n}{\epsilon_0} dx = \frac{\Delta x}{\epsilon_0} \rho^n_{k+1/2}. \tag{2.13}$$

Here, $\rho^n_{k+1/2}$ is the average charge density inside c_k at $t = t^n$:

$$\begin{aligned} \rho^n_{k+1/2} &= \int_{c_k} \rho^n \frac{dx}{\Delta x} = \sum_s Q_s \sum_{i_s} \int_{x_k}^{x_{k+1}} S^m \left(\frac{x - x^n_{i_s}}{\Delta x} \right) \frac{dx}{\Delta x} \\ &= \sum_s \frac{Q_s}{\Delta x} \sum_{i_s} W^m \left(\frac{x_{k+1/2} - x^n_{i_s}}{\Delta x} \right), \end{aligned} \tag{2.14}$$

where

$$W^m \left(\frac{x_k - x^n_{i_s}}{\Delta x} \right) \;=\; \int_{x_k - \Delta x/2}^{x_k + \Delta x/2} S^m \left(\frac{x - x^n_{i_s}}{\Delta x} \right) dx \tag{2.15}$$

defines the weighed contribution of a macro-particle at x_{i_s} to the average charge density of the kth cell.

The explicit forms for both shape S^m and weight W^m functions that we use in our code are given in Appendix A.2. In Figure 2.1 we plot different weight functions.

2.2.4 Solving Maxwell's equations

Equation (2.13) gives the change in the electric field at cell edges exactly. However, a complete solution also requires the boundary condition, $E_{k=0}$. Therefore, we rewrite Equation (2.13) as

$$E^n_k = E^n_0 + \frac{\Delta x}{\epsilon_0} \sum_{j=0}^{k-1} \rho^n_{j+1/2}. \tag{2.16}$$

We see that E^n_k inherits the error of E^n_0. To find E^n_0, we first find the sum of cell-edges field $E^n_{\rm tot} \equiv \sum_k E^n_k$. The second equation in (2.2) can be re-written (for $m > 0$) as

$$\begin{aligned} \partial_t E_{\rm tot} &= -\sum_k \frac{j_k}{\epsilon_0} = -\frac{1}{\epsilon_0} \sum_s Q_s \sum_{i_s} v_{i_s} \sum_k S^m(x_k, x_{i_s}) \\ &= -\sum_s \frac{Q_s}{\Delta x \epsilon_0} \sum_{i_s} v_{i_s} = \frac{-j_{\rm tot}}{\epsilon_0}. \end{aligned} \tag{2.17}$$

The first equality uses $\sum_k \Delta x S^m(x_k, x_i) = \sum_k W^{m-1}(x_k, x_i) = 1$, which is a property of spline functions implemented in our code (see Table A.1). Note that j_{tot} can be calculated exactly at each time-step using the macro-particles' velocities. If the plasma macro-particles have a total current, then $\partial_t E \neq 0$, i.e., setting $\partial_t E$ to zero will artificially add a constant electric field on the grid or equivalently a counter current.

Equation (2.17) is approximated to second, third, and fourth orders of accuracy, respectively, as:

$$E^n_{\text{tot}} = E^{n-1}_{\text{tot}} - \frac{\Delta t}{\epsilon_0} j^{n-\frac{1}{2}}_{\text{tot}} + O(\Delta t^3) \tag{2.18}$$

$$E^n_{\text{tot}} = \frac{21}{23}E^{n-1}_{\text{tot}} + \frac{3}{23}E^{n-2}_{\text{tot}} - \frac{1}{23}E^{n-3}_{\text{tot}} - \frac{24}{23}\frac{\Delta t}{\epsilon_0} j^{n-\frac{1}{2}}_{\text{tot}} + O(\Delta t^4) \tag{2.19}$$

$$E^n_{\text{tot}} = \frac{17}{22}E^{n-1}_{\text{tot}} + \frac{9}{22}E^{n-2}_{\text{tot}} - \frac{5}{22}E^{n-3}_{\text{tot}} + \frac{1}{22}E^{n-4}_{\text{tot}} - \frac{12}{11}\frac{\Delta t}{\epsilon_0} j^{n-\frac{1}{2}}_{\text{tot}} + O(\Delta t^5). \tag{2.20}$$

Proceeding in a similar way to generate higher-order accurate, asymmetric estimates for E^n_{tot} results in numerically unstable approximations. Thus, we stop at 4th order accurate method given in Equation (2.20).

To find E_0 from E_{tot}, we multiply Equation (2.13) by the index k, and then sum over all cells. The left hand side is given by

$$\sum_{k=0}^{N_c-1} k\left(E^n_{k+1} - E^n_k\right) = \sum_{k=1}^{N_c}(k-1)E^n_k - \sum_{k=1}^{N_c-1} kE^n_k = N_c E^n_{N_c} - E^n_{\text{tot}}. \tag{2.21}$$

Then, using the periodicity of E_k, i.e., $E_{N_c} = E_0$, we can write

$$E^n_0 = \frac{E^n_{\text{tot}}}{N_c} + \frac{\Delta x}{\epsilon_0 N_c}\sum_{k=0}^{N_c-1} k\,\rho^n_{k+1/2}. \tag{2.22}$$

Thus, for a given set of particle data $\{x^n_{i_s}, v^{n-1/2}_{i_s}\}$, we are able to find the electric field at the edges of the cells, E^n_k. Importantly, the only source of error is the error introduced in finding E^n_{tot}.

The error, for fixed $\Delta t/\Delta x$ (motivated by the CFL condition), is of order $O(\Delta x^4)$ if we use Equation (2.18) to update E^n_{tot}. The error drops to $O(\Delta x^5)$ or $O(\Delta x^6)$ with

Equations (2.19) or (2.20), respectively. It is also important here to note that an $O(\Delta x^k)$ error in the force would introduce an $O(\Delta x^{k+1})$ error in the updated data of the macro-particles.

2.2.5 Back-interpolation: force on macro-particles

Having determined the electric field using Equations (2.13), (2.14), and (2.18) or (2.19) or (2.20) to different orders of accuracy from the macro-particle positions and velocities, we now calculate the force on the individual macro-particles. The effective electric field that acts on the macro-particle (Equation (2.9)) can be determined from the electric field at each cell face, E_k^n as follows

$$\begin{aligned} E_{i_s}^n &= \sum_k \int_{c_k} E^n(x) S^m(x, x_{i_s}^n) dx \\ &= \sum_k \frac{E_{k+1}^n + E_k^n}{2} \int_{x_k}^{x_{k+1}} S^m(x, x_{i_s}^n) dx + O(\Delta x^2) \\ &= \sum_k \frac{E_{k+1}^n + E_k^n}{2} W^m \left[(x_{k+1/2} - x_{i_s}^n)/\Delta x \right] + O(\Delta x^2). \end{aligned} \tag{2.23}$$

In Appendix A.1.2, we show that the approximation in Equation (2.23) leads to exact momentum conservation and vanishing self-forces. Another possible approximation of $E_{i_s}^n$, that has the same order of accuracy is given by

$$\begin{aligned} E_{i_s}^n &= \sum_k E_k^n \int_{x_{k-1/2}}^{x_{k+1/2}} S^m(x, x_{i_s}^n) dx + O(\Delta x^2) \\ &= \sum_k E_k^n W^m \left[(x_k - x_{i_s}^n)/\Delta x \right] + O(\Delta x^2). \end{aligned} \tag{2.24}$$

The approximation in Equation (2.24) is used, for instance, in Haugbølle & Frederiksen (2013). It generally leads to violation of momentum conservation and unphysical self-forces as shown in Appendix A.1.1. The order of accuracy for the back-interpolation step is typically second order (e.g., Haugbølle & Frederiksen, 2013; Lapenta & Markidis, 2011; Lapenta, 2016; Brackbill, 2016) because of the use of lower order interpolation functions.

Using higher order interpolation functions implies a smoother representation of the phase-space distribution function. As a consequence, we can assume a smoother represen-

tation of the electric fields[3]. Therefore, since we implemented up to 5th order spline interpolation function, this allows constructing up to *5th order* accurate back-interpolation. To derive a higher order accurate method, we approximate the integration $I_k = \int_{c_k} E^n(x) S(x, x^n_{i_s}) dx$ using Simpson's rule:

$$\begin{aligned} I_k &= \int_{x_k}^{x_{k+1}} E^n(x) S^m(x, x^n_{i_s}) dx \\ &= \frac{\Delta x}{6} \left[E^n_k S^m_{k,i_s} + 4E^n_{k+\frac{1}{2}} S^m_{k+\frac{1}{2},i_s} + E^n_{k+1} S^m_{k+1,i_s} \right] + O(\Delta x^5), \end{aligned} \tag{2.25}$$

where we define $S^m_{k,i_s} \equiv S^m(x_k, x^n_{i_s})$.

To utilize Equation (2.25) we need to approximate $E^n_{k+\frac{1}{2}}$ in terms of cell-edges fields E^n_k as follows

$$E_{k+\frac{1}{2}} = \frac{-E_{k+2} + 9(E_k + E_{k+1}) - E_{k-1}}{16} + O(\Delta x^4) \tag{2.26}$$

$$= \frac{3(E_{k+3} + E_{k-2}) + 150(E_{k+1} + E_k) - 25(E_{k+2} + E_{k-1})}{256} + O(\Delta x^6). \tag{2.27}$$

Using Equation (2.25) and since $\Delta x S^m \in [0, 1]$ (see Table A.1), $O(\Delta x^4)$ error in $E_{k+\frac{1}{2}}$ implies $O(\Delta x^4)$ error order in E_{i_s} and $O(\Delta x^6)$ error in $E_{k+\frac{1}{2}}$ implies $O(\Delta x^5)$ error order in E_{i_s} (because of the error order in Equation (2.25)). Therefore, the approximate electric field $E^n_{i_s} = \sum_k I_k$ on a macro-particle at x_{i_s}, using the periodicity of E_k, can be expressed as

$$\begin{aligned} E^n_{i_s} &= \sum_k \Delta x S^m_{k+\frac{1}{2},i_s} \left[\frac{9(E^n_k + E^n_{k+1}) - (E^n_{k+2} + E^n_{k-1})}{24} \right] \\ &\quad + \sum_k \frac{E^n_k}{3} \left[\Delta x S^m_{k,i_s} \right] + O(\Delta x^4) \end{aligned} \tag{2.28}$$

$$\begin{aligned} &= \sum_k \frac{E^n_k}{3} \left[\Delta x S^m_{k+\frac{1}{2},i_s} \right] + \sum_k \Delta x S^m_{k+\frac{1}{2},i_s} \\ &\quad \times \left[\frac{3(E^n_{k+3} + E^n_{k-2}) + 150(E^n_{k+1} + E^n_k) - 25(E^n_{k+2} + E^n_{k-1})}{384} \right] \\ &\quad + O(\Delta x^5). \end{aligned} \tag{2.29}$$

[3] An order m interpolation function means that f is $m+1$ times spatially differentiable.

To summarize, here we showed how we can find the forces on the individual macro-particles for a given discretized field on a grid. The force error can be of order $O(\Delta x^2)$, $O(\Delta x^4)$, or $O(\Delta x^5)$ if we use Equation (2.23), (2.28), or (2.29), respectively. Given the numerical error in finding E_k^n, so far we have shown how, for a given set of particle data $\{x_{i_s}^n, v_{i_s}^{n-1/2}\}$, we can find the forces on such particles $F_{i_s}^n$. The error can be of order $O(\Delta x^2)$, $O(\Delta x^4)$, or $O(\Delta x^5)$, by employing consecutively higher order equations in finding E_0^n.

2.2.6 Pusher: particle update

To push the individual particles we use a leapfrog scheme to discretize the equations of motions for the particles,

$$u_{i_s}^{n+1/2} = u_{i_s}^{n-1/2} + \Delta t \frac{Q_s}{M_s} E_{i_s}^n + O(\Delta t^3), \tag{2.30}$$

$$x_{i_s}^{n+1} = x_{i_s}^n + \Delta t v_{i_s}^{n+1/2} + O(\Delta t^3). \tag{2.31}$$

The code assumes that the initial positions of the particles are provided at $t = 0$, but the initial momenta are given at $t = -\Delta t/2$. It also assumes that at $t = -\Delta t$ the sum of electric field at cell-edges was zero, i.e., $E_{\text{tot}}^{n=-1} = 0$.

2.2.7 Error sources in our algorithm

Here, we summarize the different sources of error in the algorithm presented above.

1. The use of discretized equations to compute E_{tot}, yielding up to $O(\Delta t^5)$ accurate schemes (Equations (2.18)-(2.20)).

2. The interpolation of the field from the grid to the macro-particle to calculate the force F_{i_s}. This can be done at $O(\Delta x)$ in such a fashion that total momentum is conserved exactly, or at higher accuracy, $O(\Delta x^3)$ and $O(\Delta x^4)$ at the cost of (slightly) violating momentum conservation.

3. The updating of the particle positions, which is currently performed at $O(\Delta t^3)$.

For fixed $\Delta t/\Delta x$, as implied by the CFL condition, the above imply that our code is fundamentally 2nd order accurate, limited by the particle pusher. That is, despite improving energy and momentum conservation, the order of the interpolation function

does not set the order of accuracy of the overall scheme. Implementing a higher order symplectic integrator within our scheme would improve the convergence order; we leave this point for future work. Nevertheless, as we will show in Sections 2.4-2.6, the improved spatial order produces substantial practical enhancements in the code performance.

2.2.8 Normalized equations

Using the fiducial units (c, n_0, q_0, m_0) we define the following scales

$$\begin{aligned} t_0 &= \sqrt{m_0\epsilon_0/(q_0^2 n_0)}, \\ \mathbb{E}_0 &= \sqrt{n_0 m_0 c^2/\epsilon_0}, \\ \rho_0 &= q_0 n_0, \\ j_0 &= \rho_0 c, \\ x_0 &= c t_0. \end{aligned} \tag{2.32}$$

We then define our dimensionless variables as: $\bar{t} = t/t_0$, $dt = \Delta t/t_0$, $\bar{x} = x/x_0$, $h = \Delta x/x_0$, $\bar{u} = u/c$, $\bar{Q}_s = Q_s/q_0$, $\bar{M}_s = M_s/m_0$, $\bar{\rho} = \rho/\rho_0$, $\bar{j} = j/j_0$, $\bar{E} = E/\mathbb{E}_0$. We also identify t_0 as the time scale of the plasma frequency of the entire plasma that includes contributions from all species. This defines n_0 as follows

$$\omega_0^2 \equiv t_0^{-2} = \frac{q_0^2 n_0}{m_0\epsilon_0} = \omega_p^2 = \sum_s \frac{Q_s^2 n_s}{M_s \epsilon_0} \quad \rightarrow \quad n_0 = \sum_s \frac{\bar{Q}_s^2 n_s}{\bar{M}_s}, \tag{2.33}$$

where n_s is the number density of the macro-particles of species s and

$$n_0 \Delta x = \sum_s \frac{\bar{Q}_s^2 n_s \Delta x}{\bar{M}_s} = \frac{1}{N_c} \sum_s \frac{\bar{Q}_s^2 N_s}{\bar{M}_s}. \tag{2.34}$$

In the case where all species have the same mass and charge, $n_0\Delta x = (\sum_s N_s)/N_c = N_t/N_c$. In such case, we chose our fiducial units so that $\bar{Q}_s^2 = 1$, $\bar{M}_s = 1$, therefore, $n_0 = \sum_s n_s$.

In terms of the dimensionless variables defined above, the equations that are solved by

the code can be written as follows

$$\bar{\rho}^n_{k+1/2} = \frac{N_c}{\sum_s (\bar{Q}_s^2 N_s)/\bar{M}_s} \sum_s \bar{Q}_s \sum_{i_s} W^m \left[(\bar{x}_{k+1/2} - \bar{x}^n_{i_s})/h \right], \tag{2.35}$$

$$\bar{E}^n_{k+1} = \bar{E}^n_k + h\bar{\rho}^n_{k+1/2}, \tag{2.36}$$

$$\bar{E}^n_{i_s} = \sum_k \frac{\bar{E}^n_{k+1} + \bar{E}^n_k}{2} W^m \left[(\bar{x}_{k+1/2} - \bar{x}^n_{i_s})/h \right], \tag{2.37}$$

$$\bar{u}^{n+1/2}_{i_s} = \bar{u}^{n-1/2}_{i_s} + dt \frac{\bar{Q}_s}{\bar{M}_s} \bar{E}^n_{i_s}, \tag{2.38}$$

$$\bar{x}^{n+1}_{i_s} = \bar{x}^n_{i_s} + dt \bar{v}^{n+1/2}_{i_s}. \tag{2.39}$$

The general loop in the code is then

$$\left\{ \begin{array}{l} \bar{x}^n_{i_s} \\ \bar{v}^{n-1/2}_{i_s} \end{array} \right\} \xrightarrow{(2.35)} \bar{\rho}^n_{k+1/2} \xrightarrow{(2.36)\ \&\ \bar{E}^{n-1}_{\rm tot}} \bar{E}^n_k \xrightarrow{(2.37)} \bar{E}^n_{i_s} \xrightarrow{(2.38)\ \&\ (2.39)} \left\{ \begin{array}{l} \bar{x}^{n+1}_{i_s} \\ \bar{v}^{n+1/2}_{i_s} \end{array} \right\}.$$

A schematic representation of this loop is shown in Figure 1.5.

2.2.9 Implementation

SHARP-1D is implemented in C++, and is massively parallelized using MPI. The parallelization is done by distributing macro-particles on different processors, while reserving the first processor (rank = 0) to compute the electric field on the grid and to manage outputs.

2.3 Conserved quantities in PIC

As we mentioned in the introduction, a major test of the accuracy and fidelity of PIC schemes is their ability to preserve conserved quantities such as energy, momentum and charge. Below we discuss such conservation laws in PIC schemes and how well they are respected when different methodologies are used. We begin by showing that our algorithm is charge conserving. Then, we compare the energy and momentum conservation properties

when implicit and explicit techniques are employed[4]. We also show that the usage of higher order interpolation leads to a decrease in the aliasing which improves energy conservation while maintaining exact momentum conservation.

2.3.1 Charge conservation

In the presented algorithm, we locally obey the discretized continuity equation at all times (i.e., we use a charge conserving scheme). The discretized current density[5] coincides with the current density proposed in Esirkepov (2001). To see this, we integrate the continuity equation $\partial_t \rho(x,t) + \partial_x J_x(x,t) = 0$ over a cell of size Δx,

$$\partial_t \rho_{k+1/2}(t) + \frac{J_{k+1} - J_{k+1}}{\Delta x} = 0. \tag{2.40}$$

Therefore, we can write

$$\frac{\rho^{n+1}_{k+1/2} - \rho^{n}_{k+1/2}}{\Delta t} + \frac{J^{n+1/2}_{k+1} - J^{n+1/2}_{k}}{\Delta x} + O(\Delta t^3) = 0. \tag{2.41}$$

Using the second equation in (2.2), the current density at cell edges can be expressed as follows

$$J^{n+1/2}_k \equiv \sum_s Q_s \sum_{i_s}^{N_s} v^{n+1/2}_{i_s} S\left(x_k, x^{n+1/2}_{i_s}\right) \tag{2.42}$$

$$= -\frac{\epsilon_0}{\Delta t}\left[E^{n+1}_k - E^n_k\right] + O(\Delta t^3). \tag{2.43}$$

Then using Equations (2.43) and (2.13), we can write

$$\begin{aligned} J^{n+1/2}_{k+1} - J^{n+1/2}_k &= -\frac{\epsilon_0}{\Delta t}\left[(E^{n+1}_{k+1} - E^{n+1}_k) - (E^n_{k+1} - E^n_k)\right] + O(\Delta t^3). \\ &= -\frac{\Delta x}{\Delta t}\left[\rho^{n+1}_{k+1/2} - \rho^n_{k+1/2}\right] + O(\Delta t^3). \end{aligned} \tag{2.44}$$

Therefore, our scheme obeys exactly the second-order accurate continuity equation.

[4]Typically discretization in PIC is done using either explicit or implicit schemes. In explicit schemes (such as the algorithm presented here) particle-data are used first to calculate the fields on the grid and then particles advancement in time is carried out using these fields. On the other hand when implicit discretization is employed the equations for fields on the grid and evolution equations of particles have to be solved simultaneously in order to evolve forward in time.

[5]In fact, our presented algorithm does not require to calculate the current density for solving Poisson's equation.

2.3.2 Energy and momentum conservation

Traditional explicit algorithms lead to numerical increase in the total energy (numerical heating) while conserving the total momentum exactly (Birdsall & Langdon, 1991; Hockney & Eastwood, 1988). For explicit schemes, an energy conserving algorithm was developed in Lewis (1970). However, the total energy is conserved only in the limit of $\Delta t \to 0$. In practice, there will be numerical heating of the plasma because of the finite timestep.

On the other hand, traditional implicit algorithms tend to decrease the total energy numerically (numerical cooling) while violating the total momentum conservation (Brackbill & J. Forslund, 1985). Recently, implicit algorithms that, in principle, conserve the total energy exactly, while still *violating* momentum conservation, were introduced: for non-relativistic/classical plasmas by Markidis & Lapenta (2011); Chen et al. (2011) and relativistic plasmas by Lapenta & Markidis (2011). However, in practice, these algorithms use the Jacobian-Free Newton Krylov (JFNK) method to solve the full implicit system, introducing an error that depends on the accuracy of the Newton or Picard iteration. This leads to violation in energy conservation that can be controlled by increasing the accuracy of such methods.

One major source of energy non-conservation is the coupling between the wave modes resolved by the grid and their aliases. Aliases of a wave mode, k, are all wave modes that differ from k by integer numberof $2\pi/\Delta x$, where, Δx is the grid cell size. The reason for such coupling is that continuous particle-data (which support wave modes that include aliases of wave modes resolved by the grid) are used in the construction of phase-space moments at a discrete set control of points on the physical grid. Therefore, it appears that a promising compromise is to improve the energy conservation for momentum conserving schemes by decreasing the coupling of the wave modes resolved by the grid with their aliases.

One way to decrease the effect of aliasing is done by filtering the deposited grid moments (charge and current densities), this is used, for instance, in TRISTAN (Buneman et al., 1993) and its parallel version TRISTAN-MP (Spitkovsky, 2005). Filtering, however, when used with a momentum conserving scheme results in violating the momentum conservation and non-vanishing self-forces (an example for such case is presented in Appendix A.1.3).

Alternatively, energy conservation is naturally improved when using higher-order interpolation functions, as employed here. In Fourier space, using higher order interpolation function is qualitatively equivalent to low-pass filtering.However, for instance, filtering when used with W^0 produces larger energy errors in comparison to the errors produced when first-order interpolation, W^1, is used (cf. Section 8.7 of Birdsall & Langdon 1991).

That is, higher-order shape functions considerably decrease the impact of aliasing, resulting in an improved energy conservation for the same reasons as filtering, while simultaneously maintaining higher accuracy evolution of the underlying system. This includes, potentially, exact momentum conservation. As shown explicitly in Appendix A.3, the discretization of the plasma into macro-particles with shape functions of order m produces a spectral smearing with a width that scales as $(k\Delta x)^{-m}$, producing a corresponding an exponential decrease in aliasing for the resolved modes with shape-function order.

2.4 Validation

We begin the assessment of the numerical algorithm presented in Section 2.2 with the physical validation of simulation results against known results. This represents the first in two critical numerical tests, the second being convergence and treated in Section 2.6.

Specifically, we present comparisons with the analytical or semi-analytical results on the following test problems:

- thermal stability of a uniform plasma (Section 2.4.1),
- standing plasma waves – Plasma oscillations and linear Landau damping (Section 2.4.2), and
- two-stream instabilities – non-relativistic and relativistic (Section 2.4.3)

Because validation essentially consists of quantitative comparisons with known results, we are currently limited to phenomena in the linear regime. This appears to be a wide-spread difficulty within plasma simulations. Nevertheless, weak validation in the nonlinear regime can be found when we discuss code comparisons in Section 2.5. Here, we assume that all plasma species have the same mass, and, up to a sign, the same charge. Thus, we take as our fiducial units, $q_0^2 = Q_s^2$ and $m_0 = M_s$, which implies that $n_0 = \sum_s n_s$.

2.4.1 Thermal stability of plasma

In the absence of microscopic radiative processes (e.g., Compton scattering, bremsstrahlung), a uniform, thermal plasma should not evolve. In practice, even a uniform thermal plasma will numerically heat. This arises mainly as a consequence of aliasing as explained in Section 2.3.2.

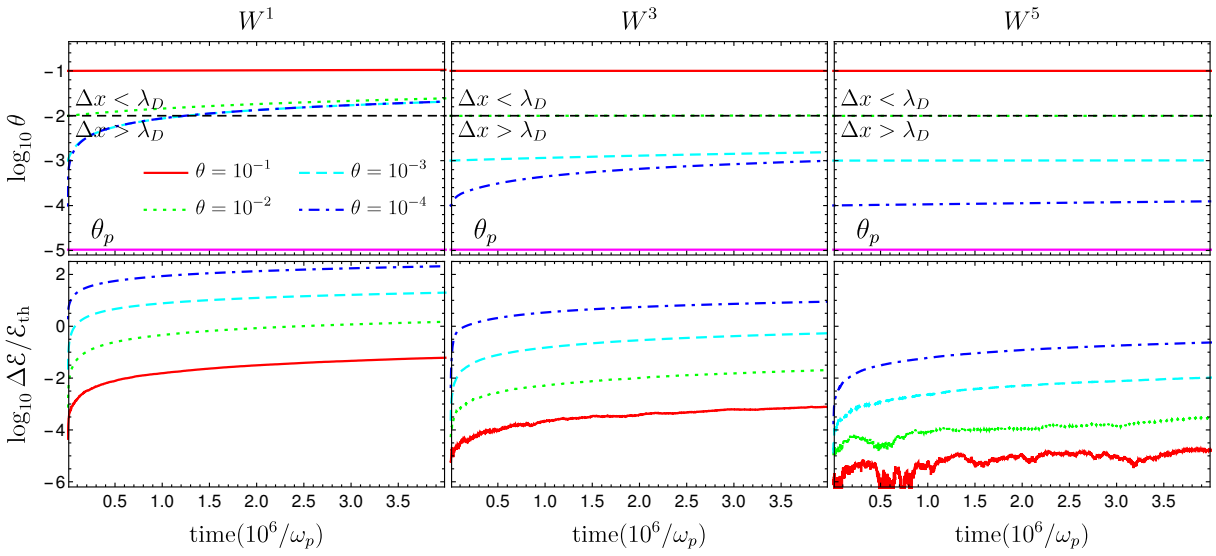

Figure 2.2 Impact of numerical heating on the temperature (top) and energy error (bottom) evolution in simulations of a stationary thermal plasma for different interpolation functions: first-order interpolation W^1 (left), third-order W^3 (middle) and fifth-order W^5 (right). Here, $\theta = k_B T/m_0c^2$ is the normalized temperature, $\Delta\mathcal{E}$ is the energy change (error) in the total energy and $\mathcal{E}_{\rm th}$ is the initial thermal energy, i.e., excluding rest mass energy of macro-particles. Therefore, $\Delta\mathcal{E}/\mathcal{E}_{\rm th}$ measures the fractional energy error with respect to the initial thermal energy of plasma. For each interpolation order we perform simulations, at *fixed* cell-size $h = 0.1$, with initial temperatures of $\theta = 10^{-1}$ (solid-red curves), $\theta = 10^{-2}$ (dotted-green curves), $\theta = 10^{-3}$ (dashed-cyan curves) and $\theta = 10^{-4}$ (dotted-dashed-blue curves). The top panels show the long term (up to $4 \times 10^6\omega_p^{-1}$) evolution of different temperatures for different interpolation orders, while the bottom panels show the evolution of the fractional energy error of the plasma. The dashed-black line in the top panel shows the Debye temperature θ_D. The purple-lines in the top panels indicate θ_p that is given by Equation (2.46): temperatures below θ_P are not well defined numerically.

There are two temperature scales that are often relevant for the numerical heating of plasma simulated with variants of the PIC algorithm. The first is the numerical Debye temperature,

$$\theta_D \equiv h^2, \tag{2.45}$$

which is the temperature at which the Debye length is equal to square of the cell size in code units. Note that this is a purely numerical quantity that defines those temperatures below which the discretization of Maxwell's equations no longer resolves the Debye length. Typically, for $\theta < \theta_D$ second order accurate codes will exhibit virulent numerical heating until $\theta \approx \theta_D$ (see, e.g., Birdsall & Maron (1980)). Thus, θ_D presents a key numerical limitation on the classes of plasmas that have been simulated to date. However, as shown in Section 2.3.2, implementing higher order spatial interpolation decreases the effect of aliasing and hence considerably decrease such heating as shown in Figure 2.2.

The second is the Poisson temperature, set by the Poisson fluctuations in the reconstruction of the particle distribution. This is set by equating the average potential and kinetic energies of randomly distributed particles (Appendix A.4.3), though in the cold and hot limits (i.e., non-relativistic and relativistic velocity dispersion limits, respectively) this reduces to

$$\theta_P = \theta_D \frac{N_c^2}{12N}\left[1 - \frac{6f_m}{N_c}\right] \times \begin{cases} 2, & \theta_p \ll 1, \\ 1, & \theta_p \gg 1. \end{cases} \tag{2.46}$$

Temperatures below θ_P are not well defined numerically. Note that the ordering of θ_P and θ_D is not fixed, though we will consider cases when $\theta_P < \theta_D$ exclusively.

Here, we study the heating due to different approximations in PIC algorithms. To this end, we start all of our simulations with temperatures higher than θ_P and study the evolution of the plasma temperatures. We perform a series of simulations for two populations of negatively and positively charged macro-particles in a periodic box of length $\bar{L} = 5$ and cell size of $h = 0.1$. The total number of macro-particles is $N_\mathrm{t} = 2 \times 10^5$. Therefore, $\theta_P \approx 1.04 \times 10^{-5}$ and $\theta_D = 10^{-2}$.

Each simulation is started at a different initial temperature: $\theta = 10^{-1}, 10^{-2}, 10^{-3}, 10^{-4}$. In all simulations presented here, we use second-order accurate back-interpolation i.e. Equation (2.23).

Since for all simulations here, $\theta \ll 1$, we start with an initial distribution function that is given by

$$f(x, v, t = 0) = \frac{N_\mathrm{t}}{L}\sqrt{\frac{\theta}{2\pi c^2}} e^{-(v/c)^2/2\theta}. \tag{2.47}$$

For the various initial temperatures, we show in Figure 2.2 the evolution of the plasma temperatures (top panel) and that of the fractional energy error of the plasma (bottom panel). We show results when first-order interpolation W^1 (left), third-order W^3 (middle), and fifth-order W^5 (right) is used in deposition and back-interpolation steps.

As expected, for the first-order interpolation (the scheme that is most commonly employed in existing PIC codes), uncontrolled heating is observed for all $\theta \leq \theta_D$. This heating subsides when $\theta \approx 3\theta_D$, requiring between one and two cells per Debye length. Hence, first order PIC algorithms face severe computational requirements to resolve cold plasmas.

However, using higher-order spatial interpolation significantly reduces the temperature at which uncontrolled numerical heating occurs. By fifth order, temperatures four orders of magnitude smaller than θ_D, and only an order of magnitude larger than θ_P, can be resolved for millions of plasma timescales. That is, high-order spatial interpolation extends the range of temperatures and timescales that can be simulated.

The marked improvement of SHARP-1D is a direct result of the corresponding improvement in energy conservation. The bottom panels of Figure 2.2 show the evolution of the growth in the energy of each simulation; in all cases the unphysical heating can be fully attributed to the failure to conserve energy. However, the *fractional* energy non-conservation is improved by nearly three orders of magnitude for each simulated temperature as the spatial interpolation order is increased from W^1 to W^5. The net result of higher spatial order is, therefore, the ability to run simulations orders of magnitude longer with orders of magnitude lower resolutions.

2.4.2 Stability of standing linear plasma waves

We now turn to the stability and evolution of plasmas with linear perturbations, specifically, standing waves. Key validation tests are the reproduction of oscillation frequencies, dispersion relations, and linear Landau damping rates. We begin with a discussion of the anticipated values followed by quantitative comparisons of standing wave evolution.

Linear Dispersion Relations and Growth Rates

As shown in Appendix A.5, the linear dispersion relation for thermal plasmas are conveniently expressed in terms of a handful of dimensionless quantities:

Table 2.1. Standing plasma waves simulation parameters and results.

$\hat{k}$	N	$\bar{\lambda}$ [a]	$\bar{\lambda}/h$ [b]	$\bar{L}/\bar{\lambda}$	ω_r/ω_p [c]	ω_r^{sim}/ω_p [d]	R_r [e]	ω_i/ω_p [c]	ω_i^{sim}/ω_p [d]	R_i [e]	$[t_{\min}, t_{\max}]\omega_p$ [f]
0.01	10^9	19.869	1761	2	1.00015	$0.99925 \pm 3 \times 10^{-7}$	0.9991	–	–	–	$[0, 10^3]$
0.35	5×10^8	0.568	67	12	1.22095	$1.21989 \pm 2 \times 10^{-5}$	0.9991	-0.03432	$-0.0344 \pm 4 \times 10^{-5}$	1.0036	$[1.7, 30.84]$
0.40	5×10^8	0.497	62	15	1.28506	$1.28145 \pm 4 \times 10^{-5}$	0.9972	-0.06613	$-0.0687 \pm 8 \times 10^{-5}$	1.0389	$[1.7, 16.80]$
0.45	5×10^8	0.442	68	19	1.35025	$1.34617 \pm 1 \times 10^{-5}$	0.9969	-0.10629	$-0.1066 \pm 2 \times 10^{-5}$	1.00326	$[1.6, 16.65]$
0.50	5×10^8	0.397	68	19	1.41566	$1.40786 \pm 2 \times 10^{-5}$	0.9945	-0.15336	$-0.1546 \pm 6 \times 10^{-5}$	1.0081	$[1.6, 8.77]$

[a] Wavelength of the initially excited mode in code units.

[b] Number of cells used to resolve the initially excited wavelength.

[c] Numerical solution of Equation (2.49).

[d] Oscillation frequencies and damping rates found by fitting the changes in simulations. The error in the fitting parameters corresponds to 99% confidence level.

[e] $R_r = \omega_r^{\rm sim}/\omega_r$ and $R_i = \omega_i^{\rm sim}/\omega_i$, where $\omega_r^{\rm sim}$ and $\omega_i^{\rm sim}$ are the oscillation frequency and damping rate obtained from fitting simulation results, respectively. An example for such a fit is shown in Figure 2.4 for the case of $\hat{k} = 0.01$ and in Figure 2.6 for the case of $\hat{k} = 0.45$.

[f] To fit our simulation results we specify a time range $[t_{\min}, t_{\max}]$ in the simulation over which we carry out the fitting.

$$\begin{aligned}\hat{\omega} &= \frac{\omega}{\omega_p}, \\ \hat{k} &= \frac{k v_{\rm th}}{\omega_p} = \frac{k}{k_D}, \\ v_p &= \frac{\hat{\omega}}{\hat{k}} = \frac{\omega}{k v_{\rm th}},\end{aligned} \tag{2.48}$$

where $v_{\rm th} = \theta^{1/2} c$ is the thermal velocity dispersion and k_D is the wavenumber associated with the Debye length. The linear dispersion relation for a non-relativistic thermal population of uniformly distributed electrons with a fixed positively charged background, i.e. infinitely massive ions, is given by (see Appendix A.5 for more details)

$$\hat{k}^2 + 1 \;=\; \sqrt{\frac{\pi}{2}} \left[\mathrm{Erfi}\left(v_p / \sqrt{2} \right) - i \right] v_p e^{-\frac{v_p^2}{2}}, \tag{2.49}$$

where Erfi is the complex error function defined as $\mathrm{Erfi}(v_p) = -i\,\mathrm{Erf}(i v_p)$. For a given $\hat{k}$, the roots $\hat{\omega}_j = \omega_j / \omega_p$ can be found by solving Equation (2.49) numerically; the real and imaginary values for ω_j yield the oscillating frequency and the growing/damping rate of the mode with wavenumber k, respectively, at a given thermal velocity $v_{\rm th}$.

Approximate expressions for the roots of Equation (2.49) are often obtained for the limit $\hat{k} \ll 1$. The most common of these, and the standard expression found in most textbooks (e.g., Boyd & Sanderson, 2003, and referred to here as "Standard") is

$$\hat{\omega}_i = -\frac{1}{2}\sqrt{\frac{\pi}{2}} \frac{1}{\hat{k}^3} e^{-\frac{1}{2\hat{k}^2} - \frac{3}{2}} \quad \text{and} \quad \hat{\omega}_r = 1 + \frac{3}{2}\hat{k}^2, \tag{2.50}$$

where ω_r and ω_i are the real and imaginary components of ω, respectively. A more accurate expression, derived by a higher-order approximation to Equation (2.49) is given by McKinstrie et al. (1999) (referred to as "Extended").

$$\begin{aligned}\hat{\omega}_i &= -\frac{1}{2}\sqrt{\frac{\pi}{2}} \left(\frac{1}{\hat{k}^3} - 6\hat{k} \right) e^{-\frac{1}{2\hat{k}^2} - \frac{3}{2} - 3\hat{k}^2 - 12\hat{k}^4} \\ \hat{\omega}_r &= 1 + \frac{3}{2}\hat{k}^2 + \frac{15}{8}\hat{k}^4 + \frac{147}{16}\hat{k}^6.\end{aligned} \tag{2.51}$$

Both of these approximates are shown in comparison to the full numerical solution ("Numerical") in Figure 2.3. It is immediately evident that the regime of applicability of both

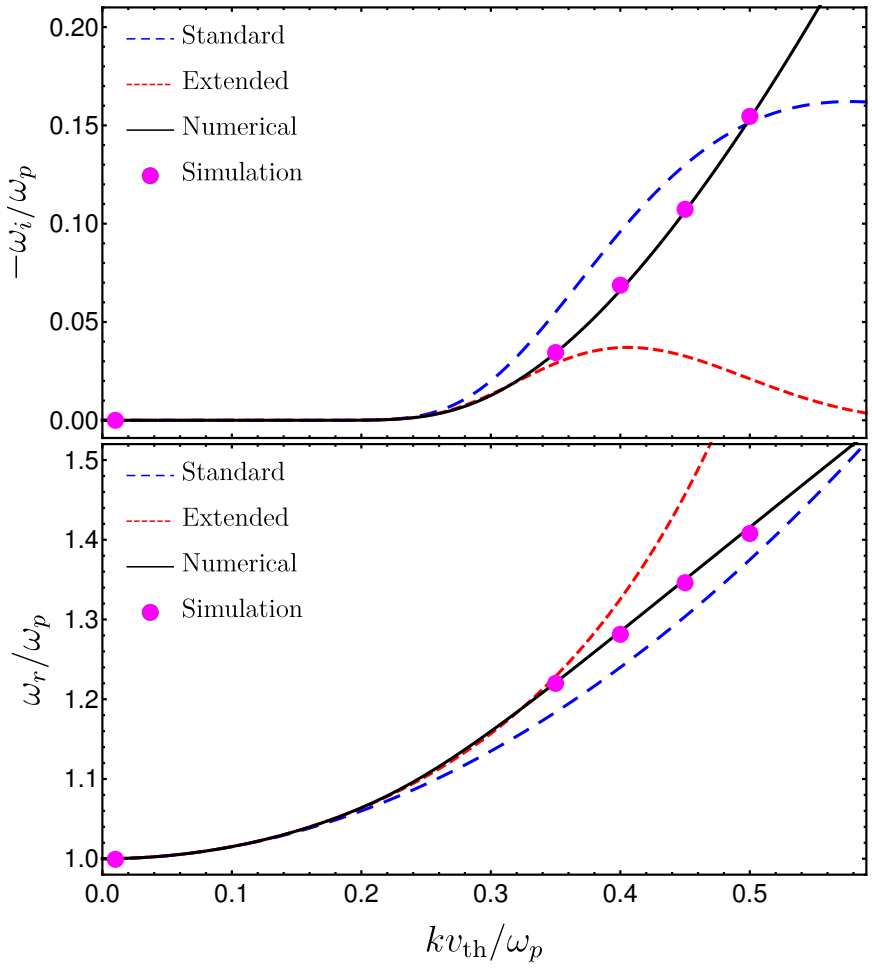

Figure 2.3 The stability of standing plasma waves in the linear regime. The black curves show the numerical solution to the linear dispersion relation, Equation (2.49). Red and blue curves are different analytical approximate solutions for the linear dispersion relation (2.49). Purple data points show results from different simulations in Section 2.4.2.

the Standard and Extended approximations is limited to $\hat{k} < 0.25$, with the numerical consequence that neither are quantitatively accurate in the rapid damping regime, where numerical validation experiments can most easily be performed.

For convenience we provide, below, a numerical fitting formula based on the formulation of McKinstrie et al. (1999) to the full numerical solution for $\hat{k} \in [0, 0.6]$ that is good to 4% throughout and better than 0.5% above $\hat{k} = 0.3$

$$\begin{aligned}
\hat{\omega}_i = &-\frac{1}{2}\sqrt{\frac{\pi}{2}}\left(\frac{1}{\hat{k}^3} - 6\hat{k} - 40.7173\hat{k}^3\right. \\
&\left. - 3900.23\hat{k}^5 - 2462.25\hat{k}^7 - 274.99\hat{k}^9\right) \\
&\times \exp\left(-\frac{1}{2\hat{k}^2} - \frac{3}{2} - 3\hat{k}^2 - 12\hat{k}^4 - 575.516\hat{k}^6\right. \\
&\left. + 3790.16\hat{k}^8 - 8827.54\hat{k}^{10} + 7266.87\hat{k}^{12}\right), \\
\hat{\omega}_r = &\ 1 + \frac{3}{2}\hat{k}^2 + \frac{15}{8}\hat{k}^4 + \frac{147}{16}\hat{k}^6 \\
&+ 736.437\hat{k}^8 - 14729.3\hat{k}^{10} + 105429\hat{k}^{12} \\
&- 370151\hat{k}^{14} + 645538\hat{k}^{16} - 448190\hat{k}^{18}.
\end{aligned} \tag{2.52}$$

In the following subsections, we report a series of simulations to test the code in the regimes $\omega_i \sim 0$ (undamped modes) and $\omega_i \neq 0$ (damped modes). We use a fixed-neutralizing background and negatively charged plasma macro-particles whose initial distribution function is given by

$$f(x, v, t = 0) = \frac{e^{-\bar{v}^2/2\theta}}{\sqrt{2\pi\theta}} \left[1 + \alpha \cos(kx)\right]. \tag{2.53}$$

In all simulations, we use $\theta = 10^{-3}$, $\alpha = 10^{-2}$, and fifth-order spatial interpolation, i.e., W^5. The damping rates and oscillation frequencies in different simulations of this section are also shown in Figure 2.3.

Plasma oscillations

At small $\hat{k}$ the linear Landau damping rate is vanishingly small, i.e., $\omega_i \approx 0$. As a result, a linear perturbation should oscillate providing quantitative tests in the form of the oscillation frequency and evolution of the mode amplitude. We initialize the simulation with

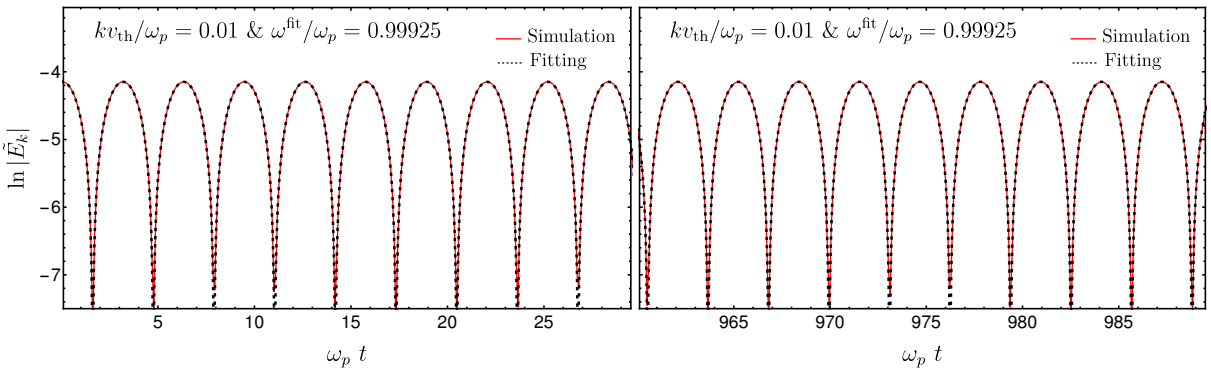

Figure 2.4 Fitting the oscillation frequency for plasma oscillation simulations. The left panel shows that the simulation data (red-curve) is in excellent agreement with the fit. It continues to excellently fit the simulation until its end at $10^3\omega_p^{-1}$ (right).

an excited mode such that $\hat{k} = 0.01$. The theoretical predictions (numerical solution of Equation (2.49)) are $\omega_r/\omega_p = 1.00015$ and $\omega_i = -4.7 \times 10^{-2167}$. The rest of our simulation parameters are given in Table 2.1.

Figure 2.4 shows the fitted values for the electric field of the initially excited oscillation modes. The oscillation frequency of the initially excited mode is found to be within 0.09% of the theoretically predicted oscillation frequency (this is measured by fitting the oscillation of such mode in the simulation over about 159 oscillation periods). The oscillation frequency and amplitude are still in excellent agreement with the theoretical prediction until the end of the simulation time $t = 10^3\omega_p^{-1}$.

In Figure 2.5 we show the evolution of the averaged energy in the excited modes (over 5 plasma periods). We find that most of the power stays in the excited mode for the whole simulation period. Coupled with the degree of energy conservation during the simulation, this implies that no more that 0.1% of the initial energy in the mode leaks into other degrees of freedom of the plasma (e.g., other modes or heating of the plasma).

Linear Landau damping rates

For larger $\hat{k}$, corresponding to comparatively larger wavenumbers, the damping rates become large. By $\hat{k} = 0.35$ the wave should damp by one e-fold in about 6 wave oscillation periods. Again, this provides a number of quantitative tests of SHARP-1D: oscillation frequencies and damping rates. Thus, here we report on simulations at large $\hat{k}$; the values of

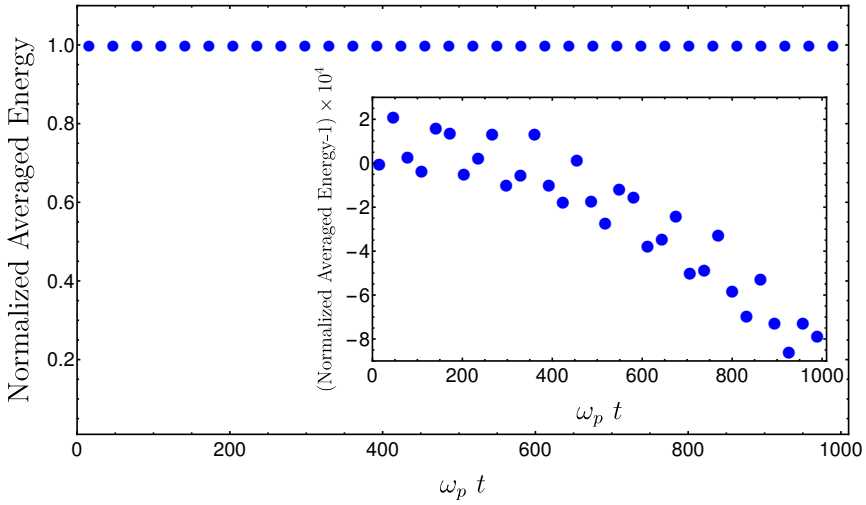

Figure 2.5 The evolution of the averaged (over 5 plasma periods) energy in the initially excited mode normalized to averaged energy in the first 5 plasma periods of such mode. The inset shows that, after evolving the simulation to $10^3\omega_p^{-1}$, the level of variation on energy carried by the mode is about 0.1% of the initial energy in that mode.

parameters in these simulation and their results are summarized in Table 2.1. The damping rates and oscillation frequencies in different simulations are also shown in Figure 2.3.

In all simulations, the oscillation frequencies and damping rates are found to be within 0.5% and 0.8% of the theoretical predictions of linear theory, respectively. The 2-columns R_r and R_i of Table 2.1 report the ratio between the oscillation frequency and damping rate in simulations to their theoretically predicted values, obtained by numerically solving Equation (2.49). The damping rate and the oscillation frequency of the simulation are obtained by fitting the evolution of the Fourier component of the electric field that corresponds to the initially excited wave mode. In Figure 2.6, we show an example (for $\hat{k} = 0.45$ simulation) of the fitting carried out to find oscillation frequencies and damping rates of different simulations.

A sudden drop in the mode energy at the first period can be observed in Figure 2.6. This is a characteristic feature of linear Landau simulations, i.e., when damping rate is comparable to the plasma frequency. Such a feature is also present when other simulation methods are used to simulate the evolution of such modes in a thermal plasma (e.g., Rossmanith & Seal, 2011; Besse & Sonnendrücker, 2003).

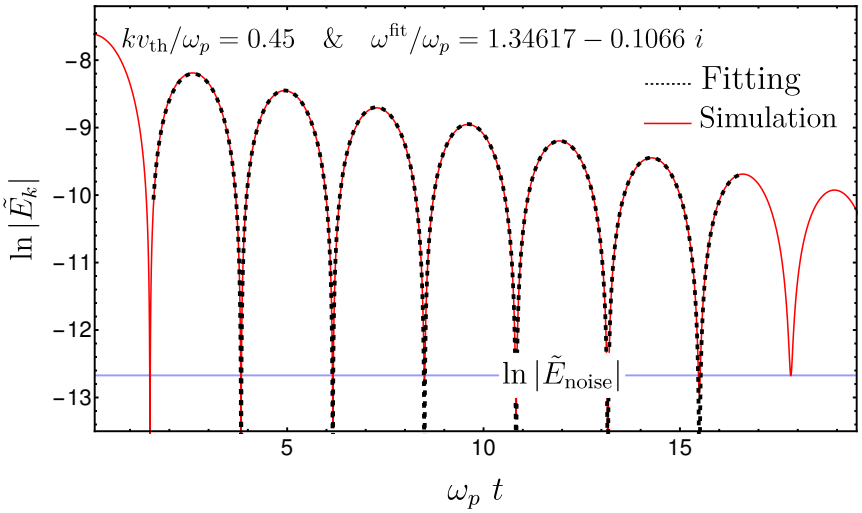

Figure 2.6 The evolution of standing linear plasma mode in the regime of high linear landau damping rate ($\hat{k} = 0.45$). The figure shows the fitting of the Fourier component of the grid electric field that corresponds to the initially excited mode. The noise level (blue line) corresponds to the estimated Fourier component of the electric field in Equation (A.41), i.e., the noise due to the finite number of macro-particles distributed uniformly on a periodic grid.

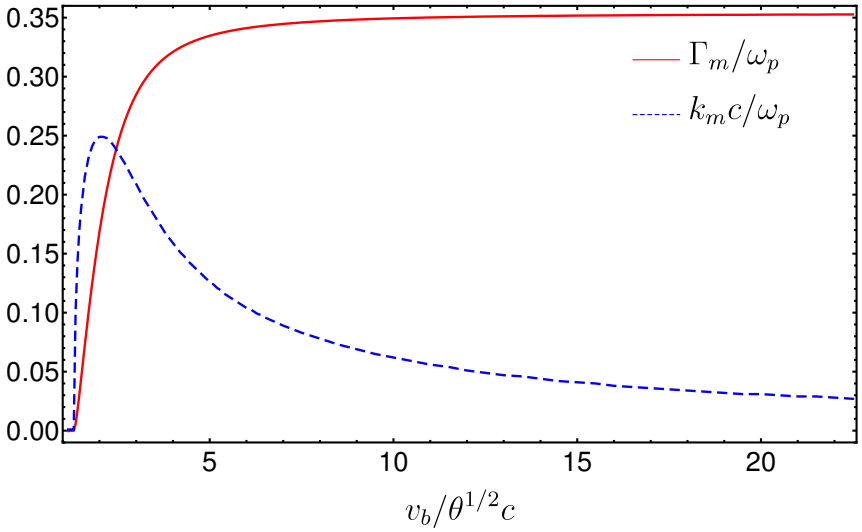

Figure 2.7 Numerical solutions to the non-relativistic two-stream instability dispersion relation (Equation (2.54)). The blue curve shows the dependence of maximum growth rate on the stream speed (and temperature). The red curve shows the dependence of maximally growing wave mode on the stream speed (and temperature).

2.4.3 Two-stream instability

We now consider the quantitative accuracy with which SHARP-1D can reproduce a dynamical instability – in 1D the primary example is the two-stream instability. This provides an opportunity to also assess the relativistic performance of the code, through the simulation of relativistic beams. Thus, we will consider two limiting regimes: non-relativistic ($v_b \ll c$) and relativistic ($u_b \gg c$). As with linear Landau damping, we will begin with a general discussion of the anticipated instability properties and then move onto quantitative comparisons.

Instability Growth Rates

In the non-relativistic regime, i.e. the streams are moving with non-relativistic speeds and have non-relativistic temperatures, the linear dispersion relation for two counter streams

in such limit is given by (see Appendix A.5 for more details)

$$\hat{k}^2+1 = \sqrt{\frac{\pi}{8}}\left[(v_p+z_b)\left(\mathrm{Erfi}\left[\frac{v_p+z_b}{\sqrt{2}}\right]-i\right)e^{-v_p z_b} + (v_p-z_b)\left(\mathrm{Erfi}\left[\frac{v_p-z_b}{\sqrt{2}}\right]-i\right)e^{v_p z_b}\right]e^{-(v_p^2+z_b^2)/2}, \quad (2.54)$$

where $z_b = \bar{v}_b/\sqrt{\theta}$, $\bar{v}_b = v_b/c$, $\hat{k} = kc\sqrt{\theta}/\omega_p$ and $v_p = \omega/kc\sqrt{\theta}$. In general this must be numerically solved to obtain the mode frequencies. The solution generally consist of two oscillatory modes, a growing mode and several damping modes. We present some of these solutions in Table 2.2. In Figure 2.7, we show the numerical solutions for the maximum growth rates (and the mode growing with such a rate) as a function of the stream speed and its temperature.

In the relativistic limit, the beam velocity distribution exhibits a narrow peak very close to the speed of light c, and is thus well described by the cold-plasma limit, i.e., $\theta = 0$. Within this limit, the linear dispersion relation for two relativistic counter streaming e^+-e^- populations (with speed v_b) is given by

$$1 = \frac{\omega_p^2/2}{\gamma_b^3(kv_b-\omega)^2} + \frac{\omega_p^2/2}{\gamma_b^3(kv_b+\omega)^2}. \quad (2.55)$$

In this case it is possible to obtain analytic solutions:

$$\frac{\omega}{\omega_p} = \pm\sqrt{\frac{1+2\hat{k}_b^2\gamma_b^3 \pm \sqrt{8\hat{k}_b^2\gamma_b^3+1}}{2\gamma_b^3}}, \quad (2.56)$$

where $\hat{k}_b = kv_b/\omega_p$. When $\gamma_b^3\hat{k}_b^2 < 1$, these again correspond to two oscillating modes, a growing mode and a damping mode. The positive imaginary root is maximized at the wavenumber

$$\frac{k_m c}{\omega_p} = \sqrt{\frac{3/8}{\bar{v}_b^2\gamma_b^3}} \quad (2.57)$$

at which the growth rate is

$$\frac{\Gamma_\mathrm{m}}{\omega_p} = \frac{1}{2\sqrt{2\gamma_b^3}}, \quad (2.58)$$

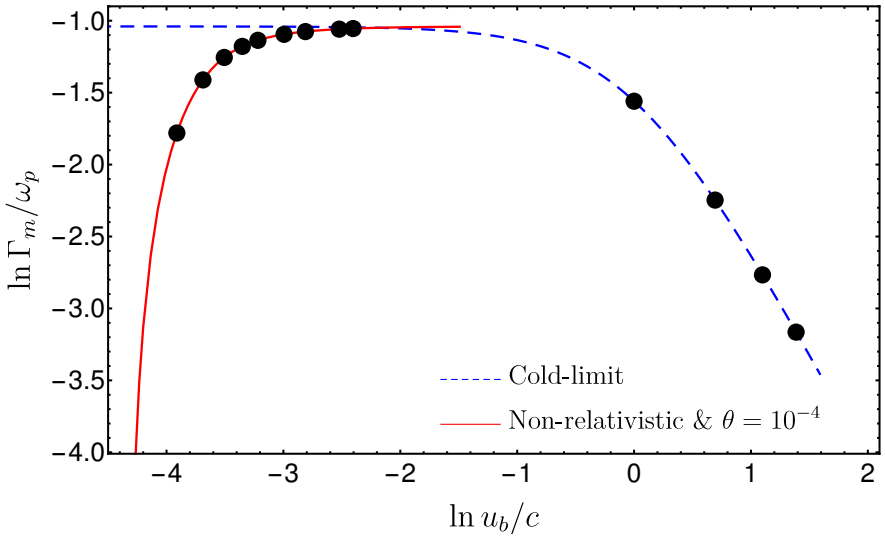

Figure 2.8 Theoretical predictions for the two-stream instability growth rates in both, relativistic and non-relativistic regimes. The black data points correspond to our simulated growth rates. Here $u_b = \gamma_b v_b$.

where $\Gamma_m = \Im(\omega_m)$ is the growth rate of that wavenumber.

The anticipated growth rates for both the relativistic and non-relativistic regimes are shown in Figure 2.8. At low beam velocities the finite temperatures of the beams suppress the growth rates appreciably relative to the cold-plasma limit, highlighting the importance of numerically solving the dispersion relation in the non-relativistic regime. In both cases (non-relativistic and relativistic streams) investigated below we use a fifth order interpolation function W^5.

Non-relativistic two-stream simulations

The non-relativistic two-stream simulations are initialized with an initial co-moving temperature of the streams at $\theta = 10^{-4}$. We use $\Delta x \sim 0.001 c/\omega_p$ and $L/\lambda_m = 20$, where $\lambda_m = 2\pi/k_m$ is the fastest growing wavelength. We start with a uniform distribution of macro-particles. Therefore, the initial distribution function is given by

$$f(x, v, t = 0) = \frac{1}{\sqrt{2\pi\theta}} \left[\frac{e^{-(\bar{v}-\bar{v}_b)^2/2\theta} + e^{-(\bar{v}+\bar{v}_b)^2/2\theta}}{2} \right]. \tag{2.59}$$

Other simulations parameters and the theoretical prediction are given in Table 2.2.

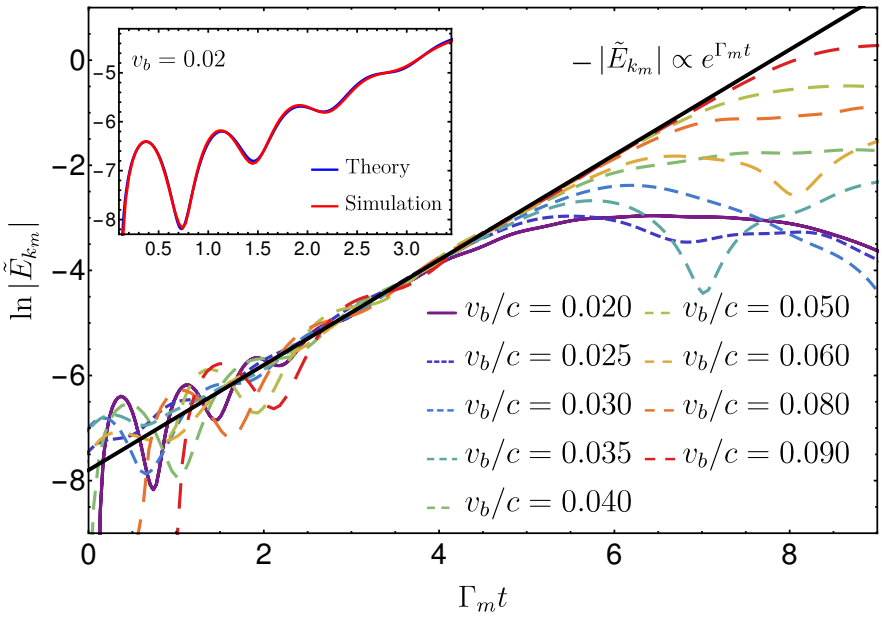

Figure 2.9 Two-stream instability simulation results in the non-relativistic regime. Different curves show the growth of the maximally growing mode (predicted by the theory) with time in units of the growth rate of this mode (predicted also theoretically) for streams with different speeds. The solid-black line is a line with slope= 1. An excellent agreement between simulation results and theoretical predictions is therefore evident: the growth rate found in the simulation and the rates calculated by solving the linear dispersion relation for such plasma i.e. Equation (2.54), numerically are quantitatively similar. The inset shows a reconstruction of the $v_b/c = 0.020$ simulation in terms of the full complement of plasma modes shown in Table 2.2. Note that, Γ_m is different for different beam velocities v_b (see Table 2.2 and Figure 2.8. Since the instability grows from the noise in all simulations, we shifted the time so that linear-phase instability growth starts at the same time for all simulations.

Table 2.2. Non-relativistic two-stream simulation parameters.

v_b/c	N_c [a]	Npc [b]	Γ_m/ω_p [c]	$k_m c/\omega_p$ [d]	$\hat{\omega}_m^1$ & $\hat{\omega}_m^2$ [e]	$\hat{\omega}_m^3$ [e]	$\hat{\omega}_m^4$ [e]	$\hat{\omega}_m^5$ [e]
0.02	5046	900.	0.168555	24.9	$\pm 1.40842 - 0.0161625i$	$-0.485447i$	$-0.915823i$	$-1.32416i$
0.025	5324	900.	0.243771	23.6	$\pm 1.47658 - 0.0123756i$	$-0.342545i$	$-0.673817i$	$-0.987125i$
0.03	6013	899.85	0.284945	20.9	$\pm 1.48041 - 0.00479742i$	$-0.249662i$	$-0.48542i$	$-0.715823i$
0.035	6904	900.	0.307734	18.2	$\pm 1.46288 - 0.00103408i$	$-0.213058i$	$-0.356584i$	$-0.524922i$
0.04	7903	900.	0.321003	15.9	$\pm 1.44312 - 0.00011898i$	$-0.247524i$	$-0.391793i$	$-0.527878i$
0.05	9974	899.91	0.334645	12.6	$\pm 1.41697 - 3.246 \times 10^{-7}i$	$-0.340762i$	$-0.388706i$	$-0.494053i$
0.06	12083	900.	0.34111	10.4	$\pm 1.40108 - 1.294 \times 10^{-10}i$	$-0.341415i$	$-0.467936i$	$-0.496439i$
0.08	16110	900.	0.346906	7.8	$\pm 1.39159 - 3.816 \times 10^{-19}i$	$-0.346906i$	$-0.396172i$	$-0.524619i$
0.09	18212	900.	0.348379	6.9	$\pm 1.38628 - 1.148 \times 10^{-24}i$	$-0.348379i$	$-0.548489i$	$-0.556374i$

[a] Number of cells.

[b] Number of computation particles per cell.

[c] Theoretical predictions for the maximum growth rate.

[d] Fastest growing wave mode predicted theoretically.

[e] $\hat{\omega} = \omega/\omega_p$: other solutions of Equation (2.54) at the fastest growing wave mode k_m.

Generally, these simulations exhibit excellent quantitative agreement with the results of the linear theory. This is clearly evident in Figure 2.9 which shows the evolution of the amplitude of the most rapidly growing mode (based on linear theory) in the non-relativistic simulations as a function of linear growth times. These should be compared to the solid black line, which shows the expected exponential growth, i.e., $e^{\Gamma_m t}$; the correspondence lasts over 4-8 e-folding times, i.e., 2-3.5 orders of magnitude, ending when the instability saturates non-linearly.

The initial oscillations correspond to other solutions of the dispersion relation, i.e., they are fully described by the linear analysis of the two-stream instability: in addition to the ultimately dominant exponentially growing mode, the linear dispersion relation admits other damping and oscillatory modes.

The inset in Figure 2.9 shows a reconstruction of the $v_b/c = 0.02$ simulation, which shows prominent oscillations at the beginning, in terms of the full complement of plasma modes shown in Table 2.2. Thus, the simulation quantitatively reproduces all of the anticipated linear features. A similar exercise is possible with the remaining non-relativistic simulations as well.

Relativistic two-stream simulations

We also performed a series of simulations for streams moving with relativistic speeds $u_b = \gamma_b v_b$. In all simulations, the initial co-moving temperature of streams is $\theta = 3 \times 10^{-3}$, $\Delta x \sim 0.05 c/\omega_p$ and $L/\lambda_m = 10$, where $\lambda_m = 2\pi/k_m$ is the fastest growing wavelength. We start with uniformly distributed macro-particles, i.e., the instability here also grows from numerical noise. The initial distribution function is given by a combination of Maxwell-Jüttner distributions:

$$f(x, v, t = 0) = \frac{\left[e^{\bar{u}\bar{u}_b/\theta} + e^{-\bar{u}\bar{u}_b/\theta}\right] e^{-\gamma_b \gamma/\theta}}{4K_1\left(1/\theta\right)}, \tag{2.60}$$

where K_1 is the Bessel function of the first kind, and θ is the temperature in the co-moving frame of each beam. All other simulations parameters, along with theoretical predictions, are shown in Table 2.3.

Figure 2.10 shows again an excellent quantitative agreement between the growth rates of the fastest growing Fourier component of the electric field in different simulations and the theoretical predictions (solid-black curve). As in the non-relativistic case, the simulation exhibits exponential growth with the anticipated growth rate over 3-4 e-folding timescales. As for the non-relativistic case, the initial oscillations can be identified with the oscillatory,

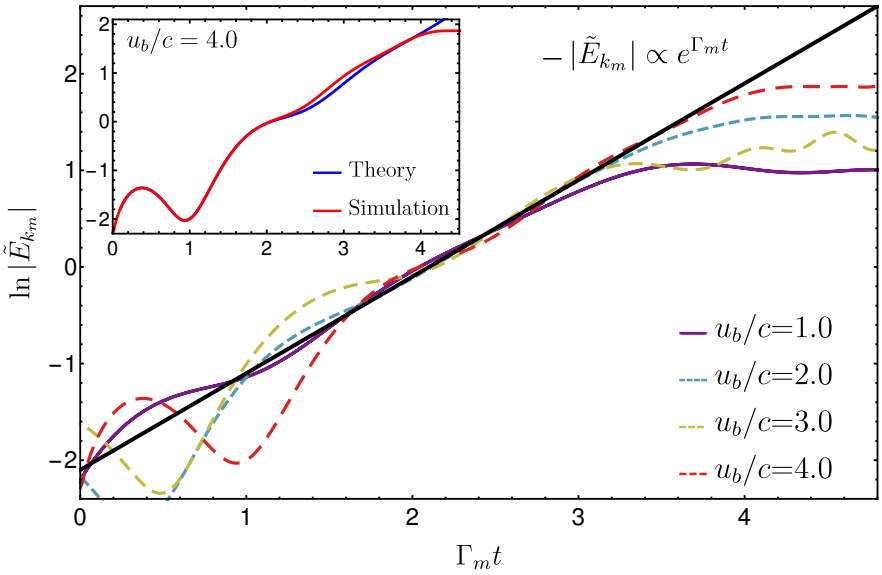

Figure 2.10 Two-stream instability simulation results the relativistic regime. Different curves show the growth of the maximally growing mode (predicted by the theory) with time in units of the growth rate of this mode (predicted also theoretically) for streams with different speeds. The solid-black line is a line with slope= 1. An excellent agreement between simulation results and theoretical predictions is therefore evident: the growth rates found in the simulations and the rates calculated by solving the linear dispersion relation in the cold-limit Equation (2.58) are quantitatively similar. The inset here shows a fit for $u_b/c = 4.0$ that includes the oscillatory components given in Table 2.3. Note that for different stream velocities, Γ_m is different (see Table 2.3 and Figure 2.8). Since the instability here grows from the noise in all simulations, we shifted the time so that linear instability growth starts at the same time for all simulations.

Table 2.3. Relativistic two-stream simulation parameters.

u_b/c	v_b/c	N_c [a]	$N_{\rm pc}$ [b]	Γ_m/ω_p [c]	$k_m c/\omega_p$ [d]	$\hat{\omega}_m^1$ & $\hat{\omega}_m^2$ [e]	$\hat{\omega}_m^3$ [e]
1	0.707	2441	491.6	0.2102	0.5147	± 0.8142	$-0.2102i$
2	0.894	6138	488.76	0.1057	0.2047	± 0.4095	$-0.1057i$
3	0.948	10948	493.24	0.0629	0.1148	± 0.2435	$-0.0629i$
4	0.970	16668	497.96	0.0422	0.0754	± 0.1636	$-0.0422i$

[a]Number of cells.

[b]Number of computation particles per cell.

[c]Theoretical predictions for the maximum growth rate.

[d]Fastest growing wave mode predicted theoretically.

[e]$\hat{\omega} = \omega/\omega_p$: other solutions given by Equation (2.56) at the fastest growing wave mode k_m.

non-growing modes (described by and below Equation (2.56)). A fit for $u_b/c = 4.0$ that includes the oscillatory components is shown as inset inside Figure 2.10.

2.5 Comparison with TRISTAN-MP

TRISTAN-MP is a publicly available PIC code to study plasma physics relevant for astrophysical problems (e.g., Spitkovsky, 2008; Riquelme & Spitkovsky, 2009; Philippov et al., 2015). Here, we compare some of the results we obtain from SHARP-1D with those obtained using TRISTAN-MP. In all cases the same initial data are used. Generally, we find a substantial improvement in the ability to conserve energy and avoid numerical heating in SHARP simulations, and a good agreement in short timescale phenomena for which energy non-conservation is not substantial.

In our test problems, the performance of SHARP compares very favorably to TRISTAN-MP, typically running roughly an order of magnitude faster. We caution, however, that this may not be an entirely fair comparison since TRISTAN-MP, as a 3D code, may not be optimized for 1D problems.

2.5.1 Numerical particulars of TRISTAN-MP

In addition to the initial conditions, TRISTAN-MP has a number of specific numerical parameters that impact its performance. While we are unable to perform an exhaustive analysis of each, we did explore the result of varying a handful of these. TRISTAN-MP is a 3D and 2D PIC code. Here, we use the 2D version with 1 or 2 cells in one of the spatial dimensions to run it in an effective 1D set-up, which enables a fair comparison to SHARP-1D.

Filtering

TRISTAN-MP provides the ability to low-pass filter the deposited grid moments, e.g., current densities on the grid, damping high-frequency noise prior to using them to solve Maxwell's equations. This reduces the coupling between the wave modes resolved on the grid with their aliases leading to improvements in the momentum and energy conservation of the algorithm. In TRISTAN-MP filtering is accomplished with a three-cell stencil that generates a weighted average between the charge current density in a given cell with its neighbors. This operation may be repeated as many times as desired, smoothing the moments on progressively larger scales.

It is not a priori clear how many passes of the three-cell filtering operation are optimal in a given problem and we experimented with a number of different choices for the comparison problems presented here. We find that after a small number of filtering passes, typically 3-5, the qualitative improvement is only moderate for $\theta \lesssim \theta_D$ and negligible for $\theta > \theta_D$.

This modest improvement comes with the additional computational cost, set by the addition of a substantial number of transverse grid cells required by many filtering passes. Thus, when comparing the numerical heating in SHARP-1D (when W^5 is used), we use four filtering passes with a 2D simulation box for TRISTAN-MP that is only 2 cells wide in the x-direction. All other comparisons employ only three filtering passes or less with a 2D simulation box for TRISTAN-MP that is only 1 cell wide in the x-direction.

Electromagnetic Mode Speeds

To suppress the numerical Cerenkov instability in TRISTAN-MP it is possible to independently set the ratio of the propagation speed of transverse electromagnetic modes to the speed of light. This is implemented explicitly via an additional numerical coefficient in Maxwell's equations. Typically, this is set near to unity, e.g., 1.025. However, in 1D

electrostatic case, the numerical Cerenkov instability does not exist, and we have verified that this factor does not qualitatively change any of the results from the TRISTAN-MP simulations.

2.5.2 Thermal stability and energy conservation

In Figure 2.11 we compare the evolution of the temperature and energy error in a pair of simulations described in Section 2.4.1. These are chosen such that in one case the Debye length is resolved by the grid cell (red curves) and when it is not resolved (blue curves). In both cases TRISTAN-MP (dashed lines) exhibits a significantly larger violation of energy conservation, differing only in the timescale over which this occurs. When the Debye length is resolved the numerical heating occurs more slowly, becoming untenable only after 3.5×10^6 plasma timescales. On the other hand, when the Debye length is not resolved, the numerical heating dominates the initial thermal energy almost instantly. In both cases by $4 \times 10^6 \omega_p^{-1}$ both simulations have generated similar *relative* degrees of numerical heating, i.e., the ratio of the energy errors to the original thermal energy of the plasma.

In comparison, SHARP-1D (solid lines) reduces the numerical heating rate drastically. When the Debye length is resolved (high temperature) the factional errors are fixed near 10^{-5} throughout the simulation. Lower temperature plasmas exhibit similar *absolute* heating rates, and therefore the relative heating for cold plasmas appears larger. However, even when the Debye length is unresolved by an order of magnitude the plasma continues to be well modeled. The origin of the improvement in the numerical heating is the improvement in the order of interpolation.

2.5.3 Stability of standing linear plasma waves

Here, we compare the evolution of a standing plasma wave, where the linear Landau damping can be ignored, i.e., the ability of both TRISTAN-MP and SHARP-1D to maintain a small amplitude oscillating wave mode.

The simulation setup is similar to that in Section 2.4.2: a fixed uniform background of ions with thermal electrons in a box with size $L = 40\, c/\omega_p$. The electrons are initially uniformally distributed. The initially excited mode is added through a velocity perturbation: we first initialize electron velocities using Equation (2.47) with $\theta = 10^{-3}$, then add a position dependent velocity perturbation to indivitual particles' velocity by adding $\beta \cos(2\pi x/\lambda)$ to their velocities, where the initially excited wavelength $\lambda = 20\, c/\omega_p$, with $\beta = 0.01\lambda/2\pi$, i.e., after about 0.25 of a plasma period this will introduce a density perturbation with an

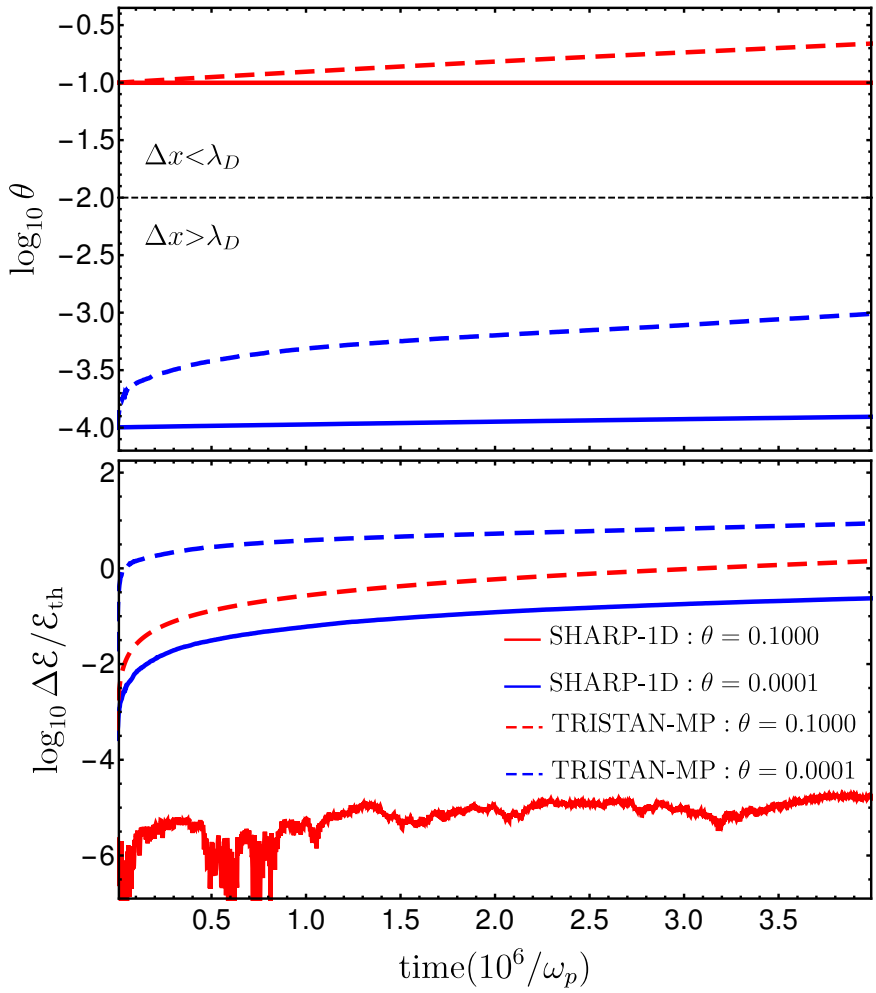

Figure 2.11 Comparison of the numerical heating (top) and energy non-conservation (bottom) when TRISTAN-MP is used (four filters, dashed curves) and when SHARP-1D (5th order, solid curves) is used. Here, $\theta = k_B T/m_0 c^2$ is the normalized temperature, $\Delta\mathcal{E}$ is the energy change/error in the total energy and $\mathcal{E}_{\rm th}$ is the initial thermal energy i.e. excluding rest mass energy of macro-particles, therefore $\Delta\mathcal{E}/\mathcal{E}_{\rm th}$ measures the fractional error with respect to the initial thermal energy of plasma. We compare the evolution of the plasmas with initial normalized temperatures of $\theta_i = 10^{-1}$ (red curves) and $\theta_i = 10^{-4}$ (blue curves) for the two codes. The dashed-black line in the top panel shows the Debye temperature θ_D.

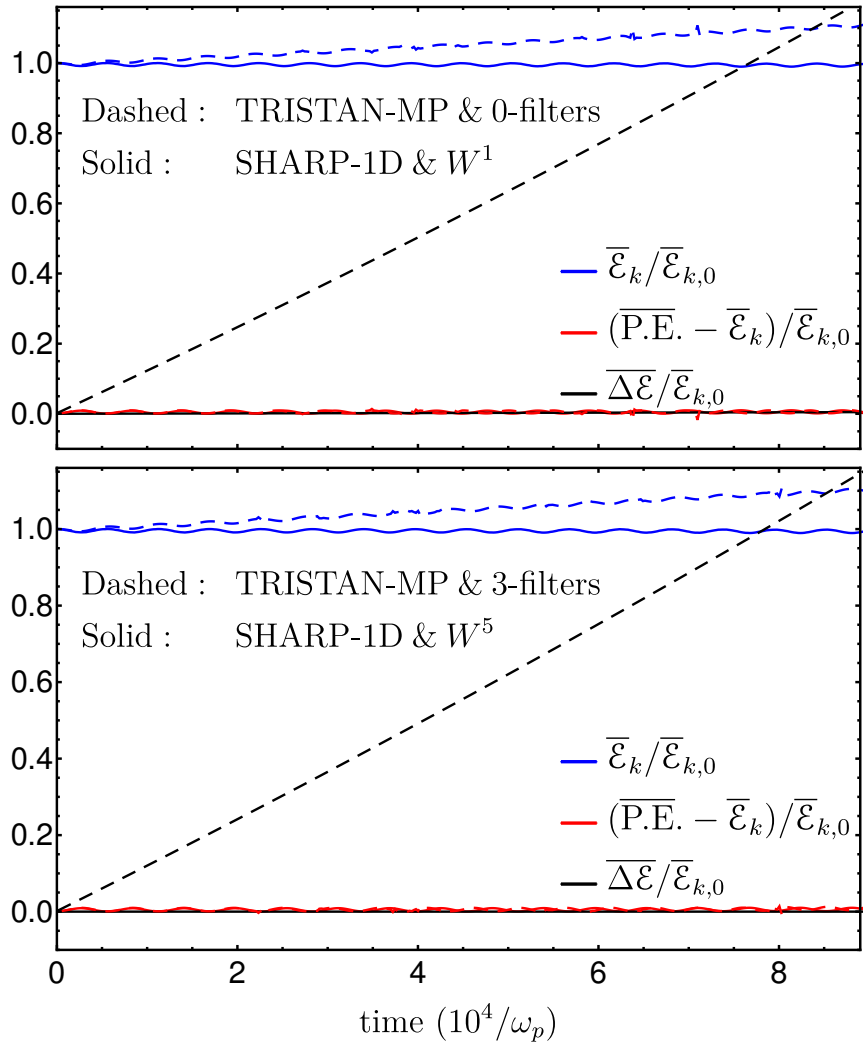

Figure 2.12 The evolution of the averaged energy in the initially excited mode (blue), the energy in all other modes resolved by the grid (red), and averaged energy error (black). Note that all energies, including the energy error, are normalized by the initial average energy in the excited mode, which is 16.87% of the initial thermal energy in the plasma, i.e., excluding the rest mass energy. Results from SHARP-1D are shown as solid lines, while results from TRISTAN-MP are shown as dashed lines. The averaging is done over 37 plasma periods, while the normalization is done with respect to the initial average energy in the excited mode, i.e., in the first 37 plasma periods. Top (bottom) panel shows a comparison of the SHARP simulations employing W^1 (W^5) to the TRISTAN-MP simulations with no (three) filtering passes.

amplitude of 0.01.[6] The cell size is $\Delta x = 0.01\, c/\omega_p$ and since $kv_{\rm th}/\omega_p = 0.009934$, linear Landau damping can be ignored. In all simulations described here, we fix the number of electrons per cell to $N_{pc} = 1250$. We also note that in all simulations the Debye length is well resolved, i.e., $\lambda_D = 3.162\,\Delta x$.

In Figure 2.12 we show the long term evolution of the energy in this isolated wave mode. In both the SHARP-1D (solid curves) and TRISTAN-MP (dashed curves) simulations, the square of the amplitude ($|\tilde{E}_k|^2$) exhibits very small, long-timescale oscillations. In the SHARP-1D simulations, these are confined to within 0.8% of the initial value over the entire simulation. In contrast, the TRISTAN-MP simulations also exhibit a secular growth in the mode amplitude, leading to approximate energy increase of 10% by $8 \times 10^4 \omega_p^{-1}$.

This behavior is independent of the interpolation order of SHARP-1D or number of smoothing filters employed in TRISTAN-MP. Even when employing W^1 with SHARP-1D, the mode amplitude continues to execute only small oscillations about the fixed value, accurately reproducing the expectation for the linear evolution of the mode. Because the Debye length is well resolved in this case, filtering improves the energy conservation only slightly in TRISTAN-MP, again, making little difference to the mode evolution.

The origin of the unphysical growth in the mode in the TRISTAN-MP simulations is unclear. The heating of the background is insufficient to appreciably Landau damp or excite the mode. We have run additional simulations with SHARP-1D employing a momentum non-conserving scheme in SHARP-1D with W^1, i.e., using Equation (2.24) (which is the back-interpolation scheme used in TRISTAN-MP), finding similar results. That is, excluding both the differences in order and the back-interpolation of the fields as the source of the secular growth in the mode energy. The only untested distinction remaining between SHARP-1D and TRISTAN-MP is the way in which the electric fields are updated.

Next, we compare the evolution of a shorter wavelength mode ($kv_{\rm th}/\omega_p = 0.45$) that has a high linear Landau damping rate. The simulations setup is exactly the same as in Section 2.4.2. The time scale for damping is much smaller than the time needed for the energy non-conservation to affect the evolution of such modes. The result from both TRISTAN-MP (dashed blue curve) and SHARP-1D (solid red line) match exactly as shown in Figure 2.13. As noted before, the initial drop in the wave amplitude is also present when other simulation methods are used (e.g., Rossmanith & Seal, 2011; Besse & Sonnendrücker,

[6] Unlike the simulations in Section 2.4.2, here we initialize a perturbation in the velocity, which is more easily done with the native initialization routines of TRISTAN-MP. We have verified that there are no significant differences when the mode is initialized as a density perturbation, and hence do so when we later compare a Landau damped wave.

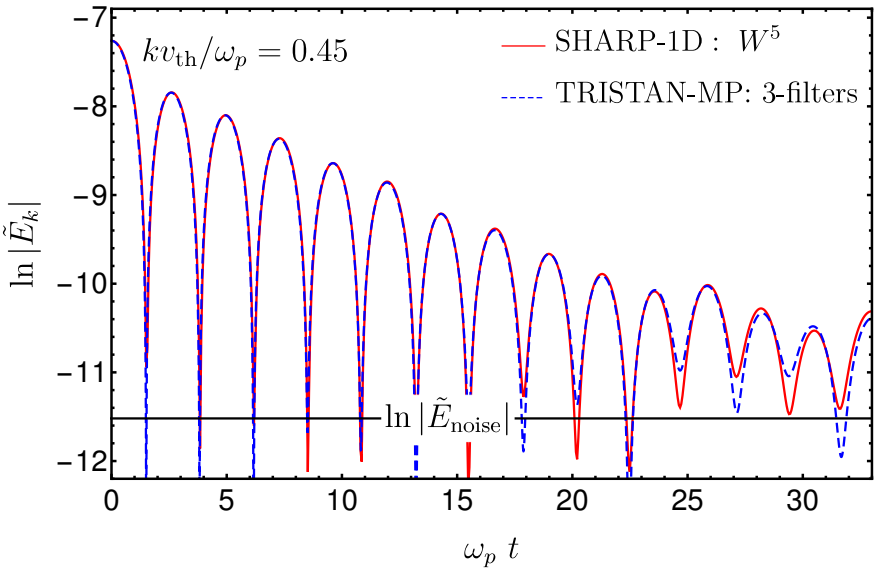

Figure 2.13 Comparison of the evolution of a linear plasma wave in the regime where the linear Landau damping rate is high ($\hat{k} = 0.45$). Here, we compare the results of SHARP-1D with W^5 (solid curves) to TRISTAN-MP with three filtering passes (dashed curves). Note that the substantially increased energy non-conservation of TRISTAN-MP causes the wave phases to decohere and to erroneously couple the energy to a longer wave mode. Since, the number of particles here is lower than it is used in Section 2.4.2, there are higher level of noise leading to a slightly faster damping rate than seen in Figure 2.6.

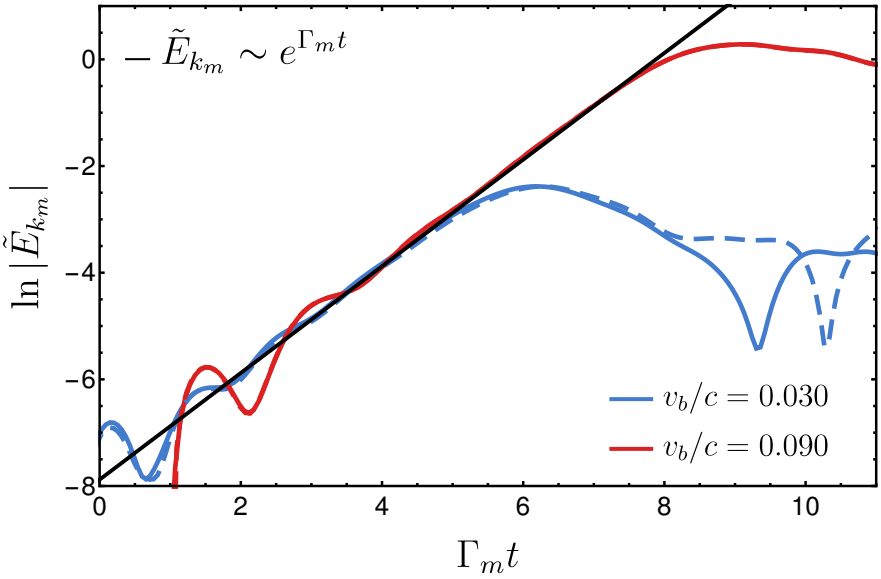

Figure 2.14 Comparison of the non-relativistic two-stream instability. Here, we compare the results of SHARP-1D with W^5 (solid curves) to TRISTAN-MP with three filtering passes (dashed curves).

2003).

2.5.4 Two-stream instability

We now compare the performance on dynamical instabilities, i.e., the two-stream instability as described in Section 2.4.3, for non-relativistic and relativistic streams. Here, again the time scale on which such instability grow is much shorter than the time scale needed for non-energy conservation to affect the evolution. Therefore, we find the same same linear evolution in both codes.

Figure 2.14 shows a comparison for two of the non-relativistic stream velocities reported in Section 2.4.3. As before, time is measured in e-foldings of the most unstable mode. In Figure 2.15 comparisons for two relativistic stream simulations reported in Section 2.4.3 are shown. Again the same linear evolution of the instability is found in both codes.

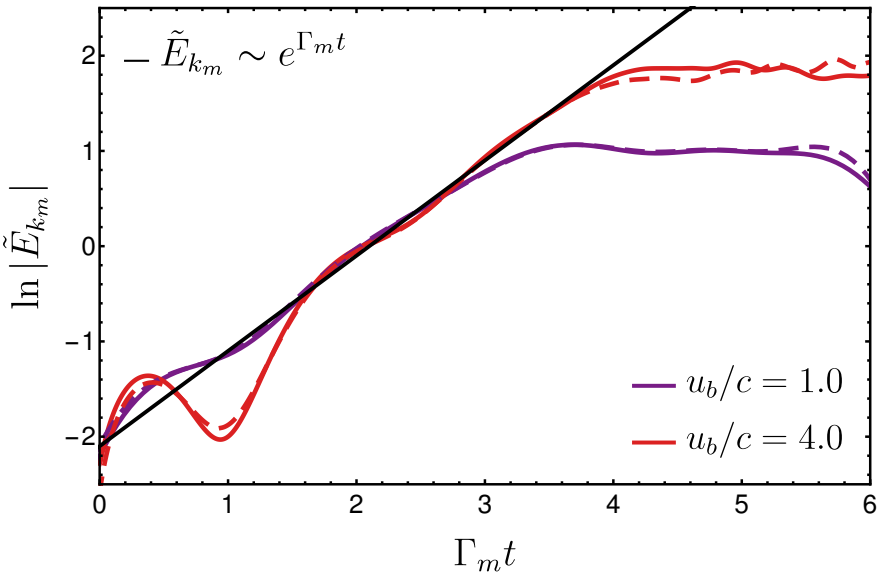

Figure 2.15 Comparison of the relativistic two-stream instability. Here, we compare the results of SHARP-1D with W^5 (solid curves) to TRISTAN-MP with three filtering passes (dashed curves).

2.6 Convergence

At the end of Section 2.2.2, we discussed the accuracy and different errors introduced in our numerical scheme. We saw that the dominant error is of order $O(h^3)$, arising from the order of particle pusher. Here, we assess the convergence of SHARP-1D and demonstrate that the numerical error decreases as expected. In particular, we develop a general criterion for convergence studies of PIC simulations by require that the ratio of the energy in the shortest wave mode to the energy in the Poisson noise of simulation to be at lease fixed. We then present a test case where the error in the total energy of plasmas is used as the measure of error: such test shows that the definition for convergence motivated above lead to a decrease in the error at the expected rate and typical methods to test for convergence fail: slower decrease in the error is observed as resolutions increase leading to a plateau in the error, where increasing the resolutions no longer lead to a decrease in the error.

2.6.1 "Resolution" in PIC algorithms

In general, for a PIC type algorithm, three notions of resolution are relevant for simulations:

1. Spatial resolution of the grid, i.e., h. This also determines the temporal resolution.

2. Momentum resolution, set by the number of particles used to construct the charge and current density at each cell, i.e., the number of particles per cell, N_{pc}.

3. Spectral resolution, set by the size of the "spectral-cell" which, for each spatial-dimension, is given by of $2\pi/L$, where L is the box-size.

The third is rarely discussed in PIC simulations and arises when a physical phenomena (in linear or non-linear regimes) has a narrow spectral support. In such cases, higher resolution simulations will require increasing the three types of resolutions simultaneously. Here we will focus on the first two, leaving a complete discussion of the third for future work.

Generally, it is necessary to increase all relevant resolutions simultaneously to study algorithmic convergence. As we will see below, this requires increasing the number of particles per cell, rather than fixing it as it is typically done. A similar requirement was found for smooth-particle hydrodynamics (SPH) simulations, where the convergence also requires increasing the number of fluid-particles within the smoothing volume of each particle to study convergence (Zhu et al., 2015).

2.6.2 Definition of convergence – equivalent simulation

The notions of both spatial resolution (i.e., h) and momentum resolution (i.e., $N_{\rm pc}$) place different constraints on the range of underlying wave modes that can effectively be simulated. Thus, some care must be taken to ensure that as these resolutions are increased simultaneously, the underlying wave complement of the physical system resolves ever smaller scales.

The discrete nature of the macro-particles places a floor on the amplitude of a mode that can be effectively resolved.[7] The average potential energy of the particle distribution, or Poisson noise, is

$$\mathcal{E}^m_{\rm noise} = \frac{L}{12\epsilon_0}\left[1 - \frac{6f_m}{N_c}\right] q_0^2 N_p, \tag{2.61}$$

where recall that f_m is a coefficient that depends on the spatial order of the algorithm. Any mode with an energy less than $\mathcal{E}^m_{\rm noise}$ is effectively unresolvable.

[7] This is what sets the thermal floor delineated by θ_P in Equation (2.46).

For comparison, we compute the energy in a single plasma mode that can be revolved on the grid[8]. For a single mode in plasma with charge density given by

$$\rho(x,t) \;=\; -A\left(\frac{q_0 N_p}{L}\right)\cos(\omega t)\,\cos(2\pi x/\lambda), \tag{2.62}$$

the electric field is given by

$$\begin{aligned} E(x,t) &= E_0(t) + \int_0^x dx^{'}\frac{\rho(x^{'},t)}{\epsilon_0} \\ &= E_0(t) - \left(\frac{q_0 N_p}{L}\frac{\lambda}{2\pi}\right)\frac{A}{\epsilon_0}\cos(\omega t)\sin(2\pi x/\lambda), \end{aligned} \tag{2.63}$$

where A is the amplitude of the initial perturbation for a mode with wavelength λ. Hence, The total electric field energy is given by

$$\begin{aligned} \mathcal{E}(t) &= \frac{\epsilon_0}{2}\int_0^L E(x,t)^2 dx \\ &= \frac{\epsilon_0 L}{2}E_0^2(t) + \frac{1}{2\epsilon_0}\left(\frac{q_0 N_p}{L}\frac{\lambda}{2\pi}\right)^2 A^2\cos^2(\omega t)\frac{L}{2}. \end{aligned} \tag{2.64}$$

Averaging over a full-period and assuming that $\langle E_0^2\rangle = 0$, the averaged potential energy in the wave mode is then

$$\langle\mathcal{E}\rangle = \frac{1}{2\epsilon_0}\left(\frac{q_0 N_p}{L}\frac{\lambda}{2\pi}\right)^2 A^2\frac{L}{4}. \tag{2.65}$$

Whether or not a mode can be resolved is then determined by the ratio of $\langle\mathcal{E}\rangle$ to $\mathcal{E}^m_{\rm noise}$,

$$r = \frac{\langle\mathcal{E}\rangle}{\mathcal{E}^m_{\rm noise}} = \frac{3}{2}\frac{A^2 N_p}{(2\pi L/\lambda)^2}\left[1 - \frac{6 f_m}{N_c}\right]^{-1} \approx \frac{3A^2}{8\pi^2}\frac{\lambda^2 N_p}{L^2}. \tag{2.66}$$

When $r > 1$ the mode is resolved on the grid, while when $r < 1$ it is dominated by the Poisson noise in the simulation and rapidly randomized. Because $r \propto \lambda^2$ this statement is also a function of wavelength, with the smallest wavelength modes being the most marginal. That is, the Poisson noise limit, $\mathcal{E}^m_{\rm noise}$, sets a minimum mode wavelength, $\lambda_{\rm min}$ the simulation can resolve, independent of the spatial resolution of the grid. Improving the fidelity of the simulation requires, therefore, concurrent increases in spatial resolution (e.g., h), momentum resolution (e.g., $N_{\rm pc}$), and spectral resolution (e.g., L).

[8]The wavelength λ is resolved by the grid, if λ/L is an integer.

Explicitly, requiring that modes on the smallest spatial scales are resolved, i.e., $\lambda_{\rm min} \propto h$, then translates into the requirement that $hN_{\rm pc}/L$ is, at least, fixed.[9] When spectral resolution is not important, this requires that if the spatial resolution increases by a factor η then $N_{\rm pc}$ must grow by a similar factor, i.e.,

$$h \to h/\eta \quad \text{and} \quad N_{\rm pc} \to \eta N_{\rm pc}\,. \tag{2.67}$$

This is unsurprising – convergence requires simultaneous and equal increases in the spatial and momentum resolutions. It does mean, however, that convergence studies are numerically demanding, as they scale as η^3, even in 1D. This is, of course, exactly the factor one would find in a purely Eulerian scheme for solving the 1D Boltzmann equation, which is similar to 2D hydrodynamics. It does make clear, however, that the inherent randomness of the particle description does nothing to improve the convergence characteristics.

2.6.3 SHARP-1D convergence – an explicit example

We now provide an explicit example of convergence testing, as described in the previous section, using SHARP-1D. To illustrate both the convergence of SHARP-1D under this definition, and equally importantly, the lack of convergence under separate definitions often employed, we do this for an extreme range of η, extending over two orders of magnitude.

We begin with a fiducial simulation, which defines $\eta = 1$. This is comprised of a population of electrons, with total number of macro-particles of $N_p = 8950$, and a fixed neutralizing background. We use a box with normalized length $\bar{L} = 39.96175$ and the initial normalized temperature for electrons $\theta_{ini} = 10^{-3}$. We start with a single excited mode with amplitude $A = 10^{-2}$ and wavelength of $\bar{\lambda} = \bar{L}/2$. Therefore, $\hat{k} = 2\pi\sqrt{\theta}/\bar{\lambda} = 0.0099441$, i.e., the linear perturbation should oscillate without damping during the entire simulation time, $T = 100\omega_p^{-1}$.

For our fiducial simulation we set the cell-size, Δx, such that $1/h = c/(\Delta x \omega_p) = 8.958$, i.e., $N_c = 358$ and $N_{pc} = N_p/N_c = 25$. For all simulations in this section we use fifth-order interpolation (W^5). Note that in this simulation the box is sufficiently large to spectrally resolve all relevant features of the dispersion relation, and thus we do not consider it further here.

[9] Such requirement (a fixed ratio of the energy in the shortest wavelength mode to the Poisson energy) implies that the ratio of the energy in a specific mode to the energy in the Poisson noise of simulation increases as η^2 with improving resolution.

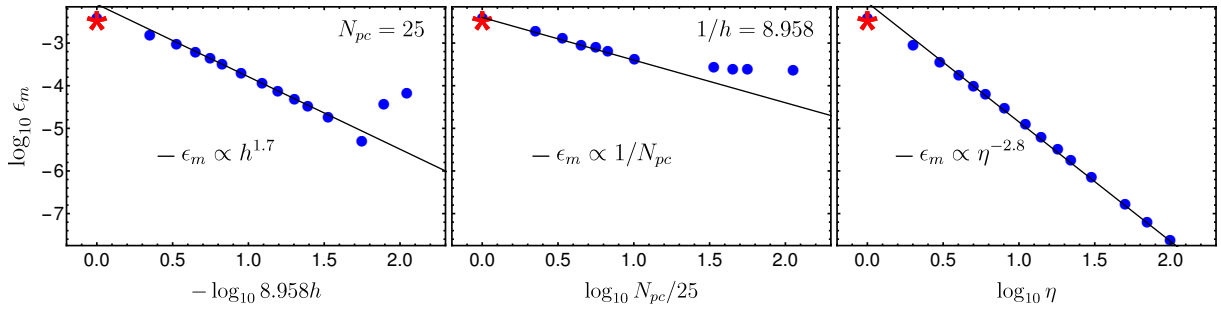

Figure 2.16 The effect of increasing different resolutions, starting with our fiducial simulation, on the maximum of the normalized energy error $\epsilon_{\rm m} \equiv \max(\Delta\mathcal{E})/\mathcal{E}_{\rm th}$, where $\Delta\mathcal{E}$ is the energy change in the total energy, $\mathcal{E}_{\rm th}$ is the initial thermal energy i.e. excluding rest mass energy. The figures show the effect of increasing the spatial resolution, h, while fixing the momentum resolution, N_{pc}, (right), the effect of increasing the momentum resolution while fixing the spatial resolution (middle) and the effect of simultaneously increasing both momentum and spatial resolution (left). The red-star result, which is the same simulation for all plots here, corresponds to our fiducial simulation ($N_{pc} = 25$ & $1/h = 8.958$). We define $\eta \equiv N_{pc}/25 = 1/(8.958 * h)$.

The accuracy measure we employ is the normalized maximum error over the duration of the simulation:

$$\epsilon_m \equiv \frac{\max(\Delta\mathcal{E})}{\mathcal{E}_{\rm th}}, \tag{2.68}$$

where $\Delta\mathcal{E}$ is the energy change in the total energy, $\mathcal{E}_{\rm th}$ is the initial thermal energy, i.e., excluding rest mass energy. Using various definitions of the energy error, i.e., average error, result in qualitatively identical results. Note that this is not the only accuracy measure we might use; others include the amplitude or phase of the wave, or the ability to reproduce other known solutions. It does have the property that it is fundamentally well understood (energy is conserved), not explicitly conserved by the code (like momentum), and universally defined.

Figure 2.16 shows the impact of increasing the various relevant notions of resolution independently and together. Increasing either the spatial or momentum resolution independently leads to a plateau in ϵ_m. The location and magnitude of this plateau depends upon the value of the non-converging resolution, i.e., when converging in spatial resolution, $N_{\rm pc}$, or when converging in momentum resolution, h. This is qualitative distinct from the case when both resolutions are increased simultaneously, for which no plateau is evident over two orders of magnitude.

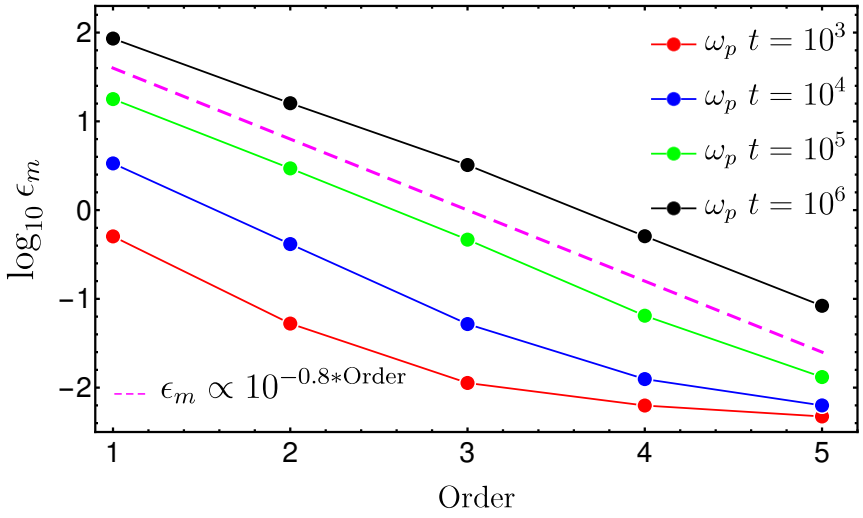

Figure 2.17 The effect of using higher order interpolation functions on the normalized maximum energy error ϵ_m. Red, blue, green and black lines are, respectively, the results after running the simulation up to 10^3, 10^4, 10^5, and 10^6 ω_p^{-1}. This shows the importance of using higher order interpolation functions in controlling the energy non-conservation, the effect is specially important for long time simulations. Here, the maximum of the normalized energy error $\epsilon_{\rm m} \equiv max\left(\Delta\mathcal{E}\right)/\mathcal{E}_{\rm th}$, where $\Delta\mathcal{E}$ is the energy change in the total energy, $\mathcal{E}_{\rm th}$ is the initial thermal energy i.e. excluding rest mass energy.

Quantitatively, using our definition of convergence, SHARP-1D converges as $\eta^{-2.8} \propto h^{2.8}$. This is very similar to the anticipated h^3, with the implication that the algorithm performance is well understood. Because this is ultimately set by the currently second-order symplectic integration employed in the particle pusher, implementing higher-order spatial interpolation will not improve this convergence rate. However, the value of the higher-order spatial interpolation appears in the magnitude of the energy error (i.e., its coefficient). This is clearly evident in Figure 2.17, which shows the error in the $\eta = 1$ simulation for different interpolation orders. Nevertheless, achieving the full benefits of the higher-order spatial implementations will require implementing an appropriate particle pusher.

2.7 Performance of SHARP-1D

To quantify the increase in the computational cost of using higher order interpolation functions, we ran a simulation using 8950 macro-particles on 5 processors for all implemented orders. In Figure 2.18, we show the relative increase in computational time for both, deposition and back-interpolation steps after running each simulation up to $t\ \omega_p = 10^3$ (red), 10^5 (green) and 10^6 (black). The computational costper update of using W^5 is 2.28 times larger than W^1. We have verified that this is independent of the number of macro-particles and the number of processors.

The advantages of using higher order interpolation are problem dependent. However, if we use the error in the total energy as a measure of accuracy, we can attempt to quantify the difference by computing the relative computational cost of simulations with different interpolation orders holding the level of accuracy fixed. Figure 2.17 shows that for a simulation that runs until time $t = 10^6\ \omega_p^{-1}$, the energy error, ϵ_m, is smaller by a factor of 10^3 when W^5 is used instead of W^1.

To achieve a similar accuracy using W^1, i.e., decreasing ϵ_m by a factor of 10^3, η needs to be increased by $10^{3/2.8} \sim 11.8$ (where we employed the scaling in the right-hand panel of Figure 2.16). Consequently, both N_{pc} and $N_{\rm c}$ each have to increase by 11.8, increasing the number of steps by the same factor. Therefore, using W^1 the computational cost increases by a factor of $11.8^3 \sim 1640$, ~ 730 times that required by W^5. That is, to achieve the same level of accuracy, a simulation that uses W^5 is about 730 faster than a simulation that uses W^1 with improved resolutions.[10]

SHARP-1D exhibits a near linear strong scaling, i.e., for fixed problem size, with the number of processors employed, $N_{\rm pr}$. By varying $N_{\rm pr}$ between 20 and 300 we find

$$t \sim N_{\rm pr}^{-0.96}. \tag{2.69}$$

2.8 Conclusions

In this chapter, we present a self-consistent discretization for the governing equations of plasma made of macro-particles in 1D (i.e., the Vlasov-Poisson equations) implemented in the SHARP-1D code. It employs a self-consistent force on such macro-particles that is

[10] For reference, on Intel Xeon 3.47 GHZ CPUs, the computational time to evolve 8950 macro-particles on five processors for 22396417 steps is 1732 seconds per processor when using W^1.

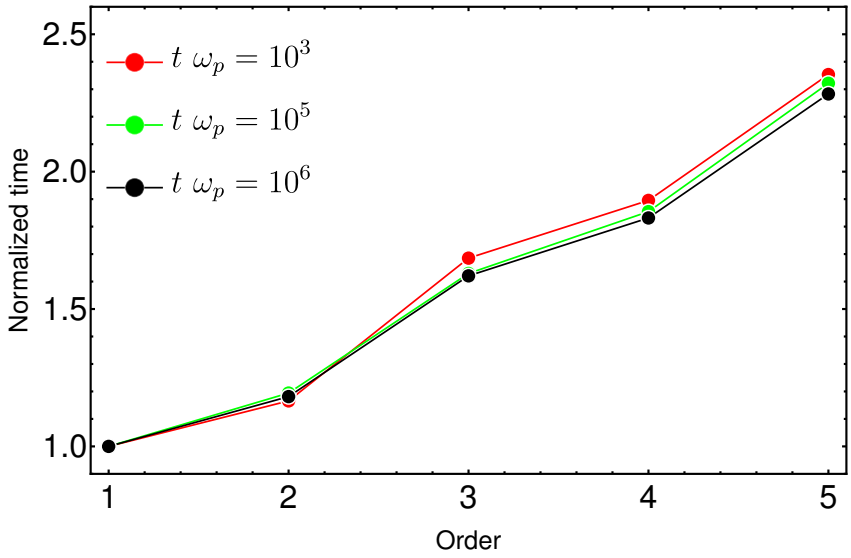

Figure 2.18 The increase in computational cost when higher order interpolation functions are used in SHARP-1D, at a fixed number of macro-particles ($N_{\rm p} = 8950$) and number of cells. The normalized time is the computation time used in both deposition and back-interpolation steps when simulation are run up to $t\ \omega_p = 10^3$ (red), 10^5 (green) and 10^6 (black), normalized to the corresponding time when W^1 is used. Here, we used 5 processor in all simulations. We have verified that the relative increase in the computational cost, we found here, is independent of the number of macro-particles and the number of processors.

accurate up to 5th order and provides; an essential step toward higher-order accurate PIC schemes. The over all accuracy of the algorithm is, however, limited by the accuracy of the particle pusher which is still second order accurate symplectic method (leap-frog).

SHARP-1D conserves momentum exactly, and despite its second order accuracy, when higher order interpolation functions are used, better energy conservation and lower numerical heating is evident. SHARP-1D simulations of a thermal plasma, whose Debye length is 10 times smaller than the cell size and which employ spatial interpolation accurate to fifth order only have an energy error, which is better than 1% of the initial thermal energy. Moreover, it shows a negligible numerical heating over a very long time (up to millions of inverse plasma frequencies, see Figure 2.2).

We present a validation of SHARP-1D against some test problems: the thermal stability of plasmas, the stability of linear plasma modes, and the two-stream instability in the relativistic and non-relativistic regimes.

To perform such validation tests, we determine the correct modes of thermal plasmas (oscillation frequencies and damping and growing rates) by solving the corresponding linear dispersion relations numerically. This is done for thermal plasmas that are both stationary and counter streaming. For convenience, we provide a fit to the oscillation frequencies and the damping rates in the linear regime of thermal plasmas up to $\hat{k} = kv_{\rm th}/\omega_p = 0.6$.

In all test problems, SHARP-1D demonstrates the ability to reproduce kinetic effects of the linear regime both qualitatively and quantitatively. This includes reproducing the correct oscillation frequencies and damping rates for different modes of the thermal plasma, and also reproducing all oscillating, growing and damping modes in counter streaming plasmas in the relativistic and non-relativistic regimes.

Results from SHARP-1D in both relativistic and non-relativistic regimes are contrasted with results from TRISTAN-MP. A substantial improvement in the ability to conserve energy and control numerical heating is shown when SHARP-1D is used.

Importantly, the improved performance due to higher spatial order does not come at the cost of increased execution time; to achieve the same level of accuracy, we have shown that, for SHARP-1D, a simulation with W^5 is almost three orders of magnitude faster than a simulation with W^1 and improved resolutions.

Finally, we develop a general criterion for convergence studies of PIC simulations by require that the ratio of the energy in the shortest wave mode to the energy in the Poisson noise of simulation to be at lease fixed.

An example study for such convergence test is presented, where the decrease in the energy error for plasma, as different relevant resolutions are increased is used as a measure

for convergence. Both the number of particles per cell and the spatial resolution of the grid are crucial resolution elements: increasing only one relevant resolution results not only in slower decrease of the error, but also in a plateau where the error does not decrease any longer as such resolution increases. Faster decrease of the error without any plateau is achieved when all relevant resolutions are increased simultaneously for such plasma.

This new PIC code provides a new avenue that enables the faithful study of the long-term evolution of plasma problems (in one dimension) that require absolute control of the energy and momentum conservation. Those include, e.g., the oblique instability driven by the highly anisotropic TeV pair beams that emerge from TeV gamma-rays that propagate from blazars to us or interactions of relativistic plasma components with a non-relativistic background plasma over long time scales (Broderick et al., 2012).

Chapter 3

Spectrally resolving beam-plasma instabilities

Many astrophysical plasmas are prone to beam-plasma instabilities. For relativistic and dilute beams, the *spectral* support of the beam-plasma instabilities is narrow, i.e., the linearly unstable modes that grow with rates comparable to the maximum growth rate occupy a narrow range of wave numbers. This places stringent requirements on the box-sizes when simulating the evolution of the instabilities. We identify the implied lower limits on the box size imposed by the longitudinal beam plasma instability, finding typically that sizes many orders of magnitude larger than the resonant wavelength are required. Using particle-in-cell simulations, we show that the failure to sufficiently resolve the spectral support of the instability yields slower growth and lower levels of saturation, potentially leading to erroneous physical conclusion.

3.1 Introduction

Plasmas are ubiquitous in astronomical environments, from the intergalactic medium to gamma-ray bursts. Often, these are subject to virulent plasma instabilities, which couple the microscopic motions of the constituent particles and the macroscopic, collective motions of the fluid. These are believed to be critical to mediating collisionless shocks, growing magnetic fields, coupling different particle species, and accelerating a fraction of these particles to high energies.

Beam-plasma instabilities, in particular, are a common feature in astrophysical contexts. They typically occur when relativistic, dilute beams propagate through background

plasmas. Examples include relativistic jet propagation (Nishikawa et al., 2016; Ardaneh et al., 2016), gamma-ray bursts (Ramirez-Ruiz et al., 2007; Ardaneh et al., 2015b), collisionless Shocks (Caprioli & Spitkovsky, 2013; Stockem Novo et al., 2016; Sironi et al., 2013), black hole accretion flows (Riquelme et al., 2016), and pair beams, induced by TeV blazars (Broderick et al., 2012; Schlickeiser et al., 2012, 2013a; Chang et al., 2014, 2016), propagating through the intergalactic medium.

Linear perturbative analyses for typical astrophysical plasmas show that a subset of linear plasma wave modes are unstable, leading to the exponential growth of their amplitudes. However, analytical solutions for linear dispersion relations can be found only in very simple cases and depend on the particulars of the equilibrium momentum distribution of plasmas (Bret et al., 2010b).

These instabilities back-react on the particle distribution that originally drove them in the linear regime and nonlinearly saturate. Analytical analysis of this nonlinear saturation rely on making appropriate choices of the physics to include and making certain approximations and simplifications on that physics. As a result these analyses can sometimes give contradictory conclusions, (e.g. Chang et al., 2014; Miniati & Elyiv, 2013). Numerical simulations offers a path to clarify the physics of nonlinear saturation, but present their own caveats and subtleties.

The particle-in-cell (PIC) method (Hockney & Eastwood, 1988; Birdsall & Langdon, 1991) is a powerful and commonly used numerical tool to study the kinetic evolution of plasmas. The general idea of this algorithm is straightforward: it follows the trajectory of particles with N-body methods while solving Maxwell's equation on an Eulerian grid. Thus, the method simultaneously takes advantage of the nearly uniform spatial extent of most plasmas (i.e., the large separation in scales between the plasma skin depth and the typical length scales of astrophysical systems) and addresses the sparse local momentum distributions that are usually relevant. The two partial descriptions of the system are coupled via interpolation, both to deposit charges and currents and to obtain the forces on the particles. While most of our remarks are true for simulation methods generally, we will explicitly demonstrate them for PIC simulations in one dimension.

The nature of PIC algorithm, which combines a discretization of momentum and physical space, evokes three notions of "resolution" that are important to accurately model the evolution. First is spatial resolution, e.g., the cell size on the Eulerian grid, Δx. Insufficient spatial resolution necessarily leads to artificial numerical damping as the various plasma waves can no longer be resolved. Second is momentum-space resolution, e.g., the number of particles per cell, $N_{\rm pc}$, in PIC algorithms. This is conceptually similar to spatial resolution, being essentially part of the generalization of the same notion to the phase space.

Insufficient momentum space resolution leads to the inability to resolve current fluctuations, again leading to unphysical plasma evolutions. Typically, simulations are tested for convergence by decreasing Δx and increasing $N_{\rm pc}$; in Shalaby et al. (2017) it was shown that simulations only converge when these are changed concurrently.

A third, often ignored, notion is *spectral* resolution, which is necessary in resolving all the relevant modes in the system. Here we show that within the context of simulating beam-plasma instabilities, this is equally important as the preceding two. Typically, simulations of the instabilities saturation employ periodic boundary conditions, for which only wave modes that fit fully within the simulation box are modeled. That is, a box with length L supports only modes with wave numbers

$$k_j = j\Delta k_{\rm sim} \quad \text{where} \quad \Delta k_{\rm sim} \equiv \frac{2\pi}{L}, \tag{3.1}$$

where j is an integer ranging from zero to $N_{\rm c}$. Thus, the spectral resolution, $\Delta k_{\rm sim}$, is a measure of the finest structures in k-space that can be probed by the simulation. Anywhere that instabilities have compact support in k, e.g., resonant instabilities in cold plasmas, generally, insufficient spectral resolution can lead to their unphysical quenching and sub-optimal growth.

Beam-plasma systems often fall into this pathological category. That is, only modes with wave numbers within $\Delta k_{\rm f}$ about the fastest growing mode, located at $k_{\rm f}$, grow at rates comparable to the maximum growth rate, $\Gamma_{\rm f}$. Therefore, a necessary condition for resolving the instability is

$$\Delta k_{\rm sim} \ll \Delta k_{\rm f} \quad \Rightarrow \quad L \gg \frac{2\pi}{\Delta k_{\rm f}}. \tag{3.2}$$

The severity of this condition depends on the width $\Delta k_{\rm f}$. For relativistic and dilute beam-plasma systems, the most relevant for many astrophysical plasmas, only a very narrow spectral subset of the unstable linear wave modes grow with rates comparable to the maximum growth rate (Bret et al., 2010b). Hence, this case is a prime example in which the spectral resolution is very important, and a special care must be taken to resolve the narrow spectral support of the important unstable wave modes.

Typically, simulations of beam-plasma instabilities done in literature require that the box size to be larger than the most unstable wavelength, i.e.,

$$\Delta k_{\rm sim} < k_{\rm f}. \tag{3.3}$$

However, this necessary condition does not guarantee that the simulation can resolve any wave modes within $\Delta k_{\rm f}$, the most important wave modes during the linear evolution.

For relativistic, dilute beam-plasma system, the width of the oblique instability in the cold limit, associated with modes that propagate at an angle to the beam direction, is typically considerably larger than that for the longitudinal modes[1]. However, when considering these multidimensional instabilities, resolving only the oblique modes is know to be insufficient. In practice, all unstable modes grow simultaneously and impact the subsequent nonlinear evolution. It was shown by Bret et al. (2010b, see especially the discussion in Section V.D) that while the oblique modes dominate initially, upon exiting the linear regime, subdominant modes continue to grow and prove essential to correctly capturing the transition to the fully nonlinear regime.

We show below that the requirement in Equation (3.2) for longitudinal modes can be very stringent and imposes a strong restriction on the simulation setup. This stringent requirement must continue to be respected in higher dimensional simulations as well.

This chapter is organized as follows: In Section 3.2, we distinguish between different plasma instabilities according to the spectral support of their growth rates, $\Delta k_{\rm f}$, as broad and narrow supported instabilities. In Section 3.3, we show the implications of the narrow spectral support on the growth rates in simulations and quantify the spectral width of unstable modes. We, then, present a number of simulations that shows a quantitative agreement between simulation results and such anticipated implications. Concluding remarks are given in Section 3.4.

3.2 Spectral support for plasma instabilities

Here, we distinguish between two different types of instabilities that can occur in astrophysical plasmas: those with broad spectral support and those with narrow spectral support. In wave number space, the distinction is based on spectral width of modes that grow with rates near the maximum growth rate. Many different (especially non-relativistic) plasma instabilities exhibit a broad spectral support, but a subclass of important problems are plagued by the instabilities with narrow spectral support. Assessing when this is likely to be the case is critical to designing appropriate simulations. Here we focus on relativistic plasma instabilities: the two-stream instability, which has broad support, and the beam-plasma instability, which has narrow support.

[1] In the warm beam limit, it is no longer clearly true that the width of the oblique instability is larger than that of the longitudinal instability. When finite temperature effects are included, the growth maps of the instabilities become much narrower (see, e.g., the various panels in Figure 17 of Bret et al., 2010b). Therefore, in warm cases the spectral resolution requirements are likely to impose even a stronger requirement on the box sizes.

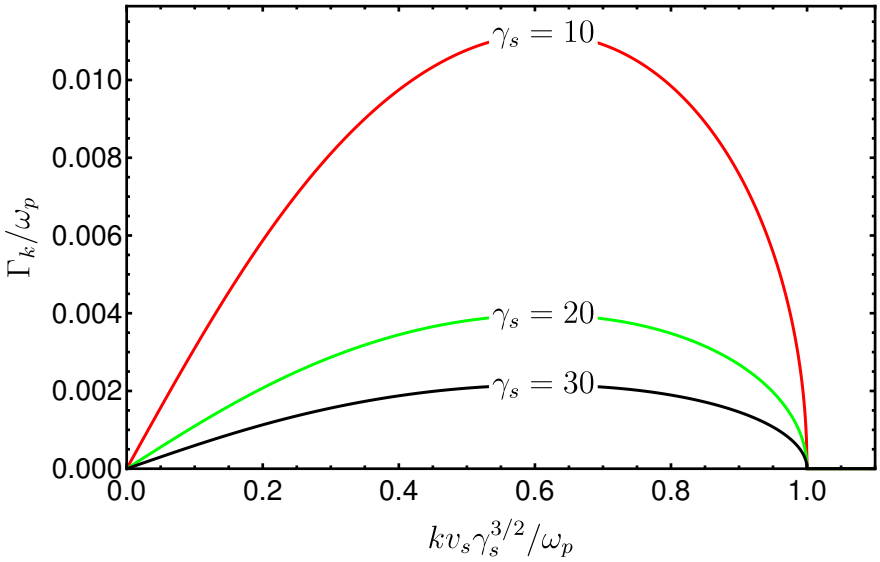

Figure 3.1 Growth rates Γ_k of the unstable wave modes in two-stream system with different center of mass Lorentz factor γ_s. Here, $kv_s\gamma_s^{3/2}/\omega_p = \lambda_{\rm min}/\lambda$, where, λ is the wavelength corresponding to the wave mode k, and $\lambda_{\rm min}$ is the shortest unstable wavelength.

3.2.1 Broad spectral support: two-stream instability

A common example of instabilities with broad spectral support is the two-stream instability, which occurs when two populations of collisionless plasmas of equal density counter-stream through each other with the same speed v_s. A subset of longitudinal plasma waves become unstable and grow exponentially with time. This leads to the heating of both streams and the acceleration of a subset of particles.

In the cold limit, the linear dispersion relation of the two-stream system is (e.g., Dieckmann et al., 2006)

$$2\gamma_s^3 = \frac{\omega_p^2}{(\omega + kv_s)^2} + \frac{\omega_p^2}{(\omega - kv_s)^2}, \tag{3.4}$$

where, $\omega_p = \sqrt{q^2 n/m\epsilon_0}$ is the plasma frequency, n is the total number density of both streams, q and m are the elementary charge and mass of streaming plasma particles, respectively, and the Lorentz factor of the streams is $\gamma_s = (1 - (v_s/c)^2)^{-1/2}$.

All modes with wave numbers such that $kv_s/\omega_p < \gamma_s^{-3/2}$ are unstable, and the most

unstable mode, i.e., that grows with the maximum growth rate, is

$$\frac{k_{\rm f}\, c}{\omega_p} = \sqrt{\frac{3/8}{(v_s/c)^2\gamma_s^3}} \quad \Rightarrow \quad \lambda_{\rm f} = 1.6329\lambda_{\rm min}, \tag{3.5}$$

where $\lambda_{\rm min} = 2\pi v_s\gamma_s^{3/2}/\omega_p$ is the minimum unstable wavelength. In Figure 3.1, we use the cold-plasma dispersion relation of the two-stream instability to plot the growth rate as a function of k for the two-stream instability: red, green and black curves are the solutions when $\gamma_s = 10$, 20 and 30, respectively. As this plot shows, neighboring modes grow at similar rates, and thus the instability has broad spectral support (we quantify the instability width below). Even if a simulation does not exactly resolve the fastest growing mode, it will nevertheless resolve a nearby mode that grows almost as fast.

To quantify this consideration, let us define a full-width, half-max of this instability in wave number space, $\Delta k_{1/2}$ as the width in k-space such that all modes grow within a factor of 0.5 of the maximum growth rate. For the two-stream instability this is given by:

$$\Delta k_{1/2} = \frac{1.07561}{\gamma_s^{3/2}}\frac{\omega_p}{v_s}. \tag{3.6}$$

Therefore, any periodic box with longitudinal size, $L_\parallel$, such that

$$L_\parallel > \frac{2\pi}{\Delta k_{1/2}} = 1.07561\lambda_{\rm min}, \tag{3.7}$$

will necessarily resolve a mode growing with a rate within a factor of 1/2 of the maximum growth rate. Therefore, the necessary condition that the box size is larger than the fastest growing wavelength, i.e., $L_\parallel > \lambda_{\rm f}$, is enough to capture the correct linear evolution of such instability in this case.

3.2.2 Narrow spectral support: beam-plasma instabilities

A more common type of instabilities for astrophysical plasmas are beam-plasma instabilities. They occur when relativistic plasma beams propagate through denser plasmas, which often define the background frame. The two-stream and beam-plasma systems differ in key aspects. The two-stream systems are typically studied in the center of mass frame, where both streams have the same number density and counter stream with the same speed. Therefore, the growth rates are characterized only by γ_s.

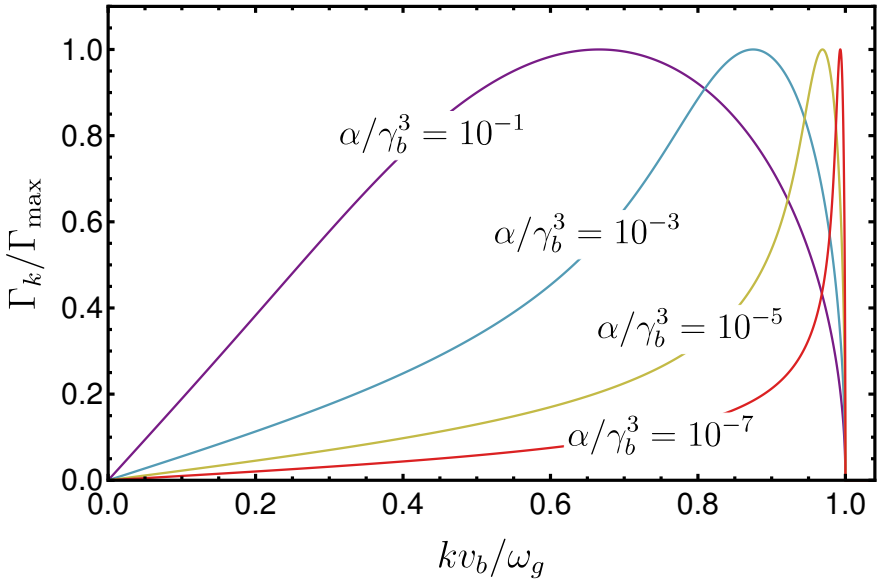

Figure 3.2 Unstable longitudinal wave modes in beam-plasma systems with different α/γ_b^3. We show the solutions for the cold limit dispersion relation – Equation (3.9).

On the other hand, beam-plasma systems are typically studied in the frame of the background plasmas and growth rates are characterized by α, the beam-to-background number density ratio and γ_b, the Lorentz factor of the beam in the frame of the background plasma. Since $\alpha < 1$ in the background frame, there is no other frame of reference where both beam and background have the same number density.

For an ultra-relativistic, very dilute beam streaming through a plasma, it was shown in Bret (2006) that the unstable wave modes lie in a very narrow wave-band within a small angle from the beam direction. The full range of unstable modes was studied in detail in Bret et al. (2010b). We focus on the longitudinal modes to show how narrow spectral support naturally emerges in beam-plasma systems.

The dispersion relation for longitudinal modes of the beam-plasma system, in the cold limit, is (Faĭnberg et al., 1969)

$$\left[\hat{k}^2 + \beta_b^2 \alpha/\gamma_b + \beta_b^2\left(1-\hat{\omega}^2\right)\right]^2 \left[1 - \frac{1}{\hat{\omega}^2} - \frac{\alpha/\gamma_b^3}{(\hat{\omega}-\hat{k})^2}\right] = 0 \tag{3.8}$$

where, $\beta_b = v_b/c$, v_b is the beam velocity, $\gamma_b = (1-\beta_b)^{-1/2}$, $\hat{\omega} = \omega/\omega_g$, $\hat{k} = k_\parallel v_b/\omega_g$, ω_g is the background plasma frequency, i.e., $\omega_g = \sqrt{e^2 n_g/\epsilon_0 m_e}$ and $\alpha = n_b/n_g$, where

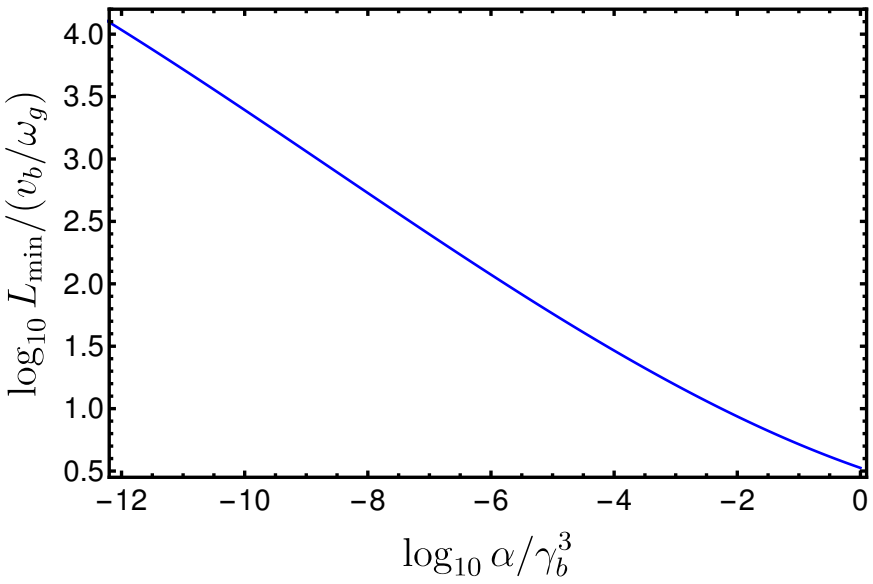

Figure 3.3 The dependence of the minimum box size, normalized to v_b/ω_g on α/γ_b^3. The minimum box size ensures that at least one growing mode with $\Gamma_{\rm max}^{\rm sim}/\Gamma_{\rm m}^{\rm th} \geq 0.5$ is resolved.

n_b is the number density of both electrons and positrons beam, and n_g is the number density of background electrons. Background ions are assumed to be immobile and have a uniform density. The roots of the first part gives only real solutions for $\hat{\omega}$, the stable electromagnetic modes, while the roots for the second part admit imaginary solutions for $\hat{\omega}$. Thus, the relevant dispersion relation can be written as

$$1 = \frac{1}{\hat{\omega}^2} + \frac{\alpha/\gamma_b^3}{(\hat{\omega} - \hat{k})^2}. \tag{3.9}$$

Equation (3.9) is a quartic polynomial whose discriminant is negative when $\hat{k}^2 < (1 + \alpha^{1/3}/\gamma_b)^3$. For $\hat{k}^2 > (1 + \alpha^{1/3}/\gamma_b)^3$, the discriminant is positive and all roots are real. Therefore, the shortest unstable wavelength is $\lambda_{\rm min} = 2\pi v_b(1 + \alpha^{1/3}/\gamma_b)^{-3/2}/\omega_g$.

The growth rates, i.e., solutions using Equation (3.9), are shown in Figure 3.2 for various value of α/γ_b^3. For values of α/γ_b^3 close to unity, the spectral support of unstable wave modes is broad, similar the two-stream system. For smaller values of α/γ_b^3, i.e., a more relativistic and dilute beam, the spectral support of the high growth rates narrows considerably. The spiky nature of the growth rate around the maximally growing mode shown is generic for dilute and relativistic beams.

The need to resolve such a narrow spectral feature translates into a stringent requirement on the length of the simulation box size. To derive the requirement on the box size, we again find the full-width half-max, $\Delta k_{1/2}$, of the growth rates, as a function of α/γ_b^3. Then we define the minimum longitudinal box-size, $L_{\rm min} = 2\pi/\Delta k_{1/2}$, needed to ensure that at least one wave mode within $\Delta k_{1/2}$ can be resolved. In Figure 3.3, we show the dependence of the minimum longitudinal box size on beam parameters (α/γ_b^3). Approximately, we find [2]

$$L_{\rm min} \approx \frac{1.15008 v_b}{\omega_g} \left(\frac{\alpha}{\gamma_b^3}\right)^{-1/3}. \tag{3.10}$$

The quantitative result of Equation 3.10 is consistent with the scaling for Δk found by Faĭnberg et al. (1969) for the case of $\alpha \ll 1$. For a simulation with a box size L such that $\lambda_{\rm min} < L < L_{\rm min}$, it is possible to *tune* the box-size so that a wave mode within $\Delta k_{1/2}$ is resolved[3]. We explore such possibility below.

[2] The quantitative result of Equation (3.10) is consistent with the scaling for Δk stated in (Faĭnberg et al., 1969) for the case of $\alpha \ll 1$.

[3] When $\lambda_{\rm min} < L < L_{\rm min}$, tuning can allow only one wave mode to grow within $\Delta k_{1/2}$.

3.3 Resolving linear beam-plasma instabilities

Here, we explicitly demonstrate the implications of the narrow spectral support on the growth rates found in PIC simulations. We find quantitative agreement between the prediction of the maximum growth in simulations and the results from the simulations.

3.3.1 Importance of spectral resolution

The growth rate, $\Gamma_k = \Im(\hat{\omega}_k)$, of the unstable modes when $\alpha/\gamma_b^3 = 10^{-7}$ are shown by the red curves in Figure 3.4. Superimposed are the growth rates of the unstable modes resolved by a simulation box (shown by the points) of lengths $L = 52c/\omega_g$ (top) and $L = 520c/\omega_g$ (bottom). The maximum growth rate accessible to the simulation, $\Gamma_{\rm max}^{\rm sim}$, is indicated by the green point. For the smaller box, which spectrally under-resolves the instability, $\Gamma_{\rm max}^{\rm sim}$ is much smaller than that implied by the linear analysis. In contrast, for the larger box, which contains many modes within the peak of the instability, the two growth rates are similar.

The ratio of the maximum growth rate accessible in a simulation, $\Gamma_{\rm max}^{\rm sim}$, to the theoretical maximum growth rate, $\Gamma_{\rm max}^{\rm th}$, is shown as a function of box size for $\alpha/\gamma_b^3 = 10^{-7}$ in Figure 3.5. At small box sizes the range of $\Gamma_{\rm max}^{\rm sim}/\Gamma_{\rm max}^{\rm th}$ is large, indicating that the maximum growth rate is frequently missed. At large box sizes, the range becomes small as a result of the increased spectral resolution, i.e., the instability is resolved. Note that even at low resolution, it is possible for the fastest growing mode to land at maximum theoretical growth rate, e.g., as shown in Figure 3.6. As mentioned above, this shows how we might attempt to *tune* simulations to resolve the fastest growing modes by design; we explore this in the following section.

3.3.2 Numerical verification

Here, we use ab initio simulations to demonstrated the importance of the spectral resolution. We run a series of simulations where we progressively increase spectral resolution, which we list in Table 3.1, and a simulation with a small, but tuned, box size (final row of Table 3.1) such that a mode growing at a rate very close to the maximum growth rate is resolved in our periodic box as shown in Figure 3.6.

For all simulations here, we use SHARP-1D (Shalaby et al., 2017) with 5th order interpolation, W^5, to improve the conservation of energy in simulations while conserving

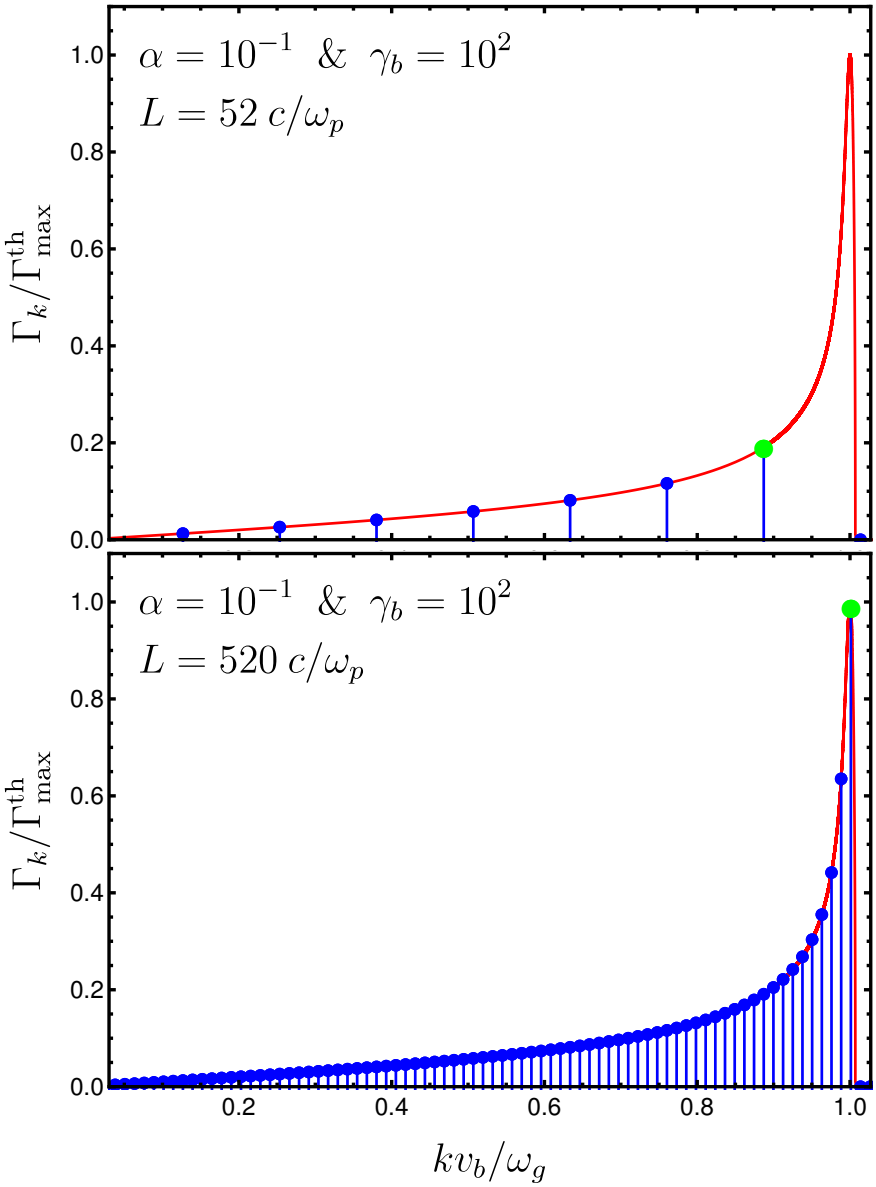

Figure 3.4 Importance of spectral resolution when simulating the linear phase of cold beam-plasma longitudinal instabilities. The red curves show the normalized growth rate, $\Gamma_k/\Gamma^{\rm th}_{\rm max}$, of the unstable wave modes when $\alpha/\gamma_b^3 = 10^{-7}$. The blue dots represent the growth rates of the wave modes resolved in simulations with box sizes 52 c/ω_p (top), and 520 c/ω_p (bottom). The green points indicate the maximum normalized growth rate in simulations with such box sizes, $\Gamma^{\rm sim}_{\rm max}/\Gamma^{\rm th}_{\rm max}$.

Table 3.1. Electrostatic beam-plasma instability simulations for $\alpha = 0.1$ and $\gamma_b = 100$.

L_c [a]	L/L_0 [b]	$\Gamma^{\rm sim}_{\rm max}/\Gamma^{\rm th}_{\rm max}$ [c]	$k^{\rm sim}_{\rm max}c/\omega_p$ [d]
026	0.1	0.1162	0.724983
052	0.2	0.1908	0.845813
130	0.5	0.3550	0.918312
260	1.0	0.6351	0.942478
520	2.0	0.9897	0.954561
1040	4.0	0.9897	0.954561
39.5	0.152	0.9926	0.954408

[a]The box size, L, in units of skin depth, i.e., $L_c = L\ \omega_p/c$, where, ω_p is the plasma frequency associated with all plasma particles: beam and background particles.

[b]$L_0 = 260\ c/\omega_p \sim L_{\rm min}(\alpha/\gamma_b^3 = 10^{-7})$.

[c]The maximum growth rate predicted of simulations due to different spectral resolutions $\Gamma^{\rm sim}_{\rm max}$ normalized to the maximum growth rate, $\Gamma^{\rm th}_{\rm max} = 3.036 \times 10^{-3}\ \omega_p$, found by solving the dispersion relation in Equation (3.9).

[d]The normalized fastest growing wave mode in simulations.

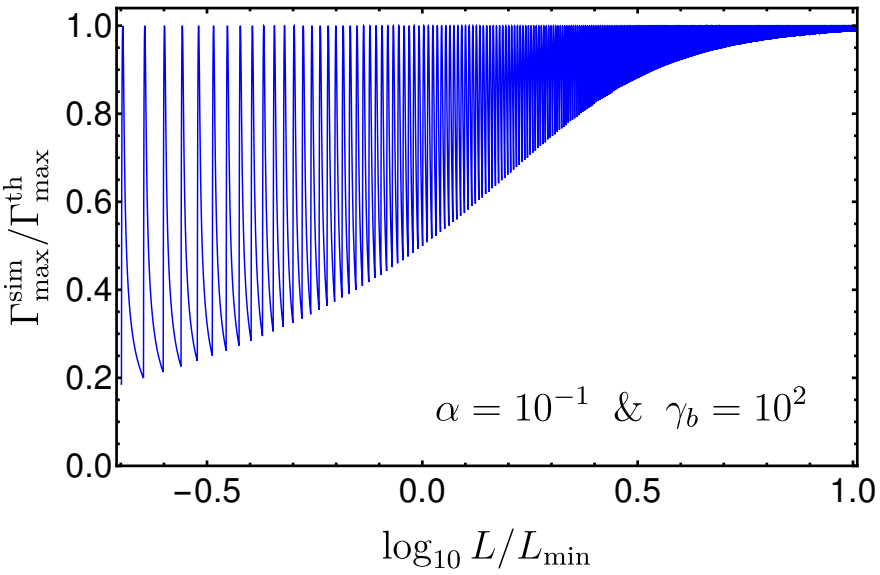

Figure 3.5 The dependence of the maximum growth rate in simulations on the box size for the case of $\alpha/\gamma_b^3 = 10^{-7}$.

the total momentum exactly. Using SHARP with W^5 is essential to avoid the excessive numerical heating typical in most available PIC codes (see Shalaby et al., 2017, for illustration). The predictions of the maximum growth in different simulations is given in Table 3.1 (green points in Figures 3.4 and 3.6). Here, we show a quantitative agreement between simulations' results and these predictions for the case of $\alpha = 0.1$ and $\gamma_b = 100$.

We fix both spatial and momentum resolutions in all simulations: $\Delta x = 0.05 c/\omega_p$ and $N_{\rm pc} = 1650$, where Δx is the grid cell size and $N_{\rm pc}$ is the number of computational particles per cell.[4] We start all simulations with a uniform distribution of both electron and positron beam particles, propagating with $\gamma_b = 100$ (in the same direction) through an initially uniform background of electrons and a fixed background of ions. The initial normalized temperature of the background electrons is $\theta_g = k_B T_g/mc^2 = 10^{-3}$, and both types of beam particles have an initial co-moving temperature of $\theta_b = k_B T_b/mc^2 = 4\times10^{-3}$, where, mc^2 is the rest mass energy of a computational particle. The rest of the simulation parameters for the different simulations are given in Table 3.1.

Using the solution of the cold-limit dispersion relation, Equation (3.9), we find that

[4]Note, the total plasma frequency ω_p is related to the background plasma frequency ω_g as, $\omega_p/\omega_g = \sqrt{1+\alpha}$.

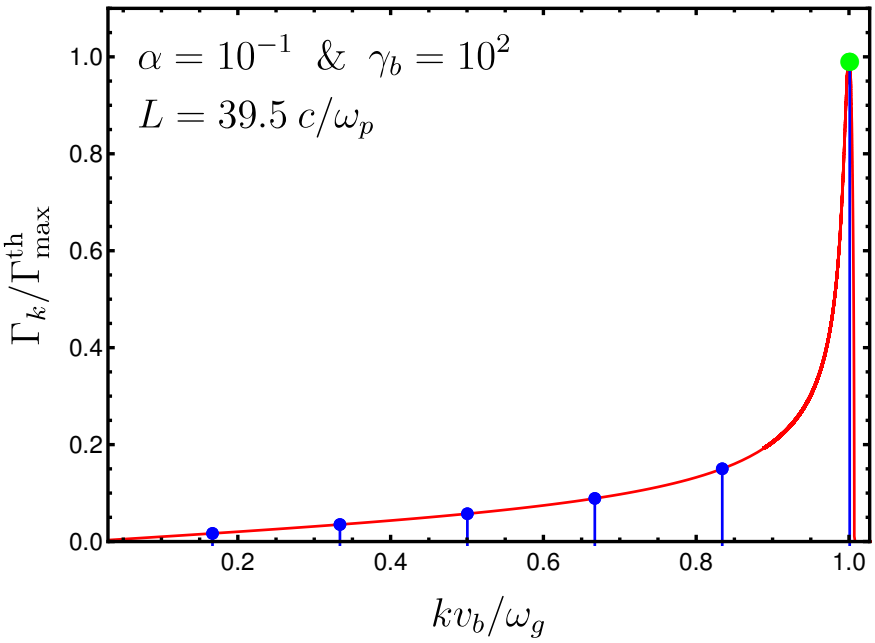

Figure 3.6 Tuning spectral resolution in simulation: the normalized growth rates $\Gamma_k/\Gamma^{\rm th}_{\rm max}$, of the unstable wave modes when $\alpha/\gamma_b^3 = 10^{-7}$ (red curve). The blue dots are the growth rates of the wave modes resolved by a simulation with box size $L = 39.5\ c/\omega_p$. Green point indicates the maximum normalized growth rate in the simulation with such box size, $\Gamma^{\rm sim}_{\rm max}/\Gamma^{\rm th}_{\rm max}$.

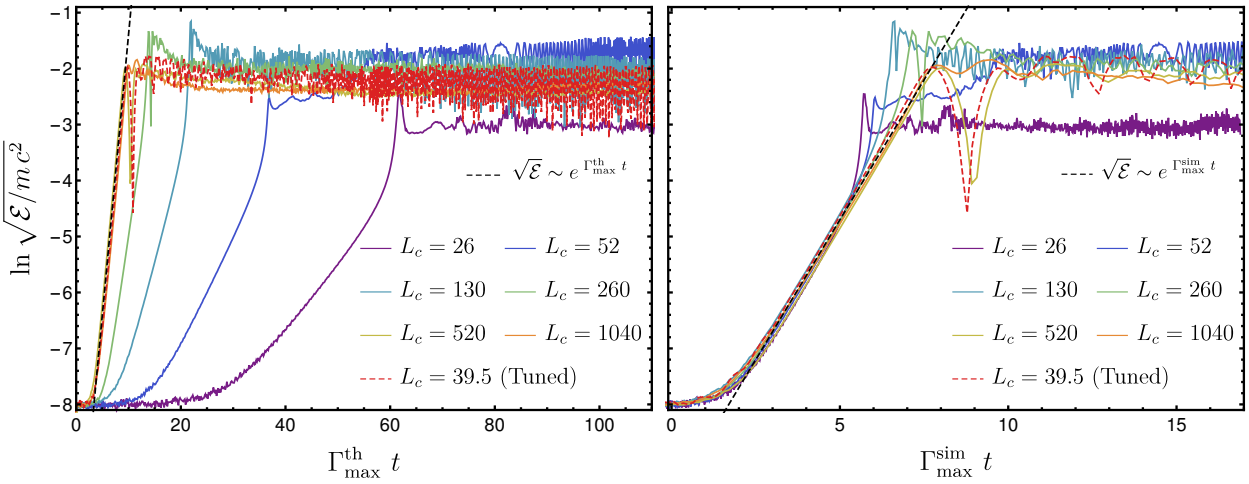

Figure 3.7 Simulation results: the growth of the total potential energy per computational particle, $\mathcal{E}$, normalized to the rest mass energy of a computational particle, mc^2. Left: time is normalized with the maximum growth rate, i.e., solution of Equation (3.9). Right: time is normalized with the maximum growth rate predicted in a simulation as shown in Figures 3.4 and 3.6. Here, $L_c = L\ \omega_p/c$. Since the growth in all simulations starts from the Poisson noise, the times are shifted in different simulations to allow for comparisons.

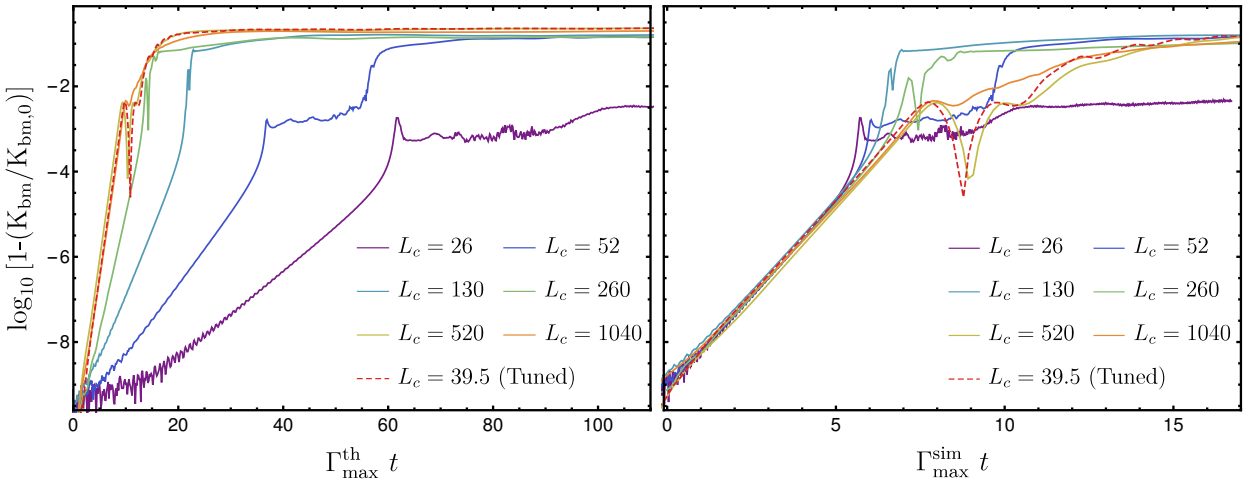

Figure 3.8 Simulation results: the evolution of the kinetic energy loss of the beam. Left: time is normalized with the maximum growth rate, i.e., solution of Equation (3.9). Right: time is normalized with the maximum growth rate predicted in a simulation as shown in Figures 3.4, 3.6. Here, $L_c = L\ \omega_p/c$. Since the growth in all simulations starts from the Poisson noise, the times are shifted in different simulations to allow for comparisons.

the fastest growing mode is $k_{\rm m}^{\rm th} = 0.95353c/\omega_p$ and its exponential growth rate is $\Gamma_{\rm max}^{\rm th} = 0.0030364\ \omega_p$. Since this mode is not typically resolved in a given simulation, simulations with different spectral resolutions will have different maximally growing wave modes $k_{\rm m}^{\rm sim}$ and, thus, a non-unity $\Gamma_{\rm max}^{\rm sim}/\Gamma_{\rm max}^{\rm th}$ (listed in Table 3.1).

In Figures 3.7 and 3.8, we show the evolution of the electric potential energy and beam energy loss respectively. In the left panels, time is normalized with the maximum growth rate, i.e., solution of Equation (3.9). In the right panels, time is normalized with the maximum growth rate predicted in simulations. Since the growth in all simulations starts from the Poisson noise, the times are shifted in different simulations such that the linear growth are aligned. These are shown on a linear scale in Figure 3.9 to better show the impact on the saturation of different box sizes.

It is difficult to make general statements regarding the impact of insufficient spectral resolution on the nonlinear saturation of the beam plasma system. However, it is clear from the late-time evolution in Figures 3.7–3.9, that both the saturation of the mode amplitudes and the energy transfer to the background can be severely reduced if the instability is badly under-resolved. Clearly visible in Figure 3.9 is the wide variation in the nonlinear saturation of the instabilities; we didn't identify any general relationship between the error

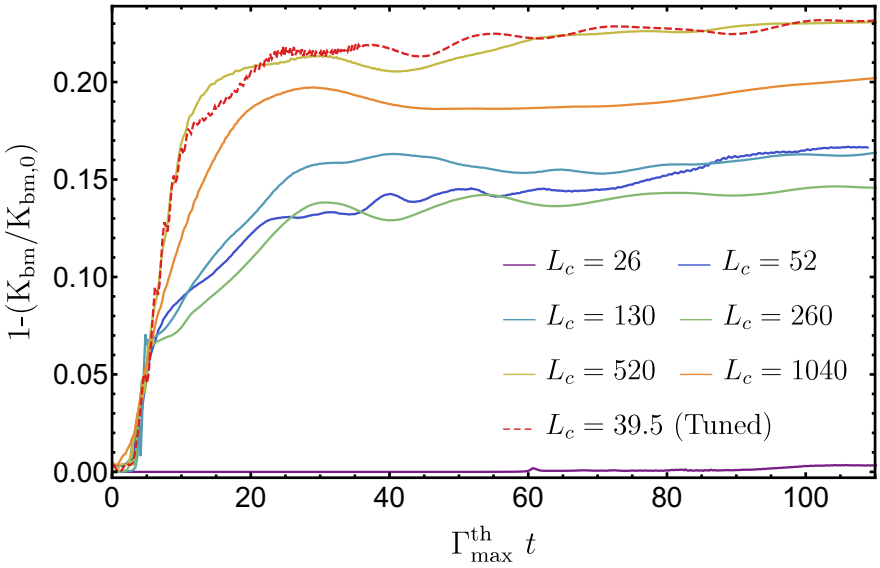

Figure 3.9 The evolution of the beam energy loss on a linear scale to better show the impact on the nonlinear saturation. The times are shifted in different simulations to allow for comparisons. The saturated energy transfer varies over three orders of magnitude and is not monotonically related to the box size (i.e., degree of under-resolution).

in the saturated energy transfer with the degree of under-resolution. We would anticipate that this would be even more severe in cases where the beams are also energetically subdominant, and thus incapable of heating the background to relativistic temperatures (which typically broaden the instabilities under consideration).

Both tuning and using large box sizes result in similar evolutions in the linear regime. The reasons for this are, first, the longitudinal unstable modes are insensitive to the background heating resulting from the energy exchange due to these instabilities, i.e., despite the physical heating, the simulation box will still be able to resolve a wave mode growing with at a rate comparable to the $\Gamma^{\rm th}_{\rm max}$. Second, the very narrow spectral support shown in Figure 3.4 means that the linear-regime evolution of the system will largely be dictated by the fastest growing wave mode.

3.4 Conclusions

A large subset of astrophysically important plasma instabilities, notably the beam plasma instabilities, have narrow spectral support, i.e., only a small subset of linearly unstable wave numbers grow with rates comparable to the maximum growth rate. This is especially true for the unstable longitudinal components of relativistic, dilute beam-plasma systems.

Accurately resolving these in numerical simulations, even in the linear regime, places stringent requirements on the spectral resolutions of the simulations. This, in turn, places *lower* limits on the size of the simulation box. Typically, for dilute, relativistic plasma beams this requires simulation boxes much larger than the typical unstable mode wavelengths. That is, requiring that the simulation has sufficient spectral resolution to resolve the full-width, half-max of the beam-plasma instability necessitates box sizes many orders of magnitude larger than the wavelength of the fastest growing modes.

Alternatively, smaller simulation boxes can be used, but they would need to be tuned. We note that while this was possible in 1D, it is unlikely to be the case in 2D and 3D. The impact of beam temperature on the maximally growing mode was studied by Bret et al. (2010a) for longitudinal, transverse, and oblique instabilities. For the relativistic, dilute case the fastest growing longitudinal mode is surprisingly insensitive to the temperature (see Figure 16 of Bret et al. 2010a); this explains the success of our tuned simulation. However, the fastest growing transverse and oblique modes are much more sensitive to temperature. Therefore, even moderate heating can lead to significant evolution in the wave number of the fastest growing mode, precluding tuning.

Using explicit PIC simulations, we have demonstrated that insufficient spectral resolution fully explains the reduced linear growth rates in 1D beam-plasma systems. That is, it is possible to quantitatively reproduce the simulated growth rates with those anticipated by the limited compliment of oscillation modes present in a simulation associated with fixed box size. These compare well with results of similar simulations in the literature (see, e.g., Gremillet et al., 2007; Bret et al., 2010b; Sironi & Giannios, 2014; Kempf et al., 2016), where the maximum growth rates are found to be smaller than anticipated by the linear theory, in some cases by up to an order of magnitude. This suggests that the reduced linear growth rates are a consequence of insufficient spectral resolution, i.e., simulation boxes that are too small.

While an extensive study of the impact of insufficient spectral resolution on the nonlinear saturation of the beam-plasma system has yet to be performed, it is clear that it does have an effect. The lowest-resolution simulation that we ran, under-predicting the linear growth rate by nearly an order of magnitude, transferred two orders of magnitude

less energy than the simulations that did spectrally resolve the instability. Thus, this raises concerns with the robustness of the conclusions that may be drawn from published simulations of relativistic beam-plasma systems.

For multidimensional (2D or 3D) simulations, in the cold limit, the width of the instability of the oblique modes is, typically, larger than that for the longitudinal modes. However, when finite temperature effects are included, the growth maps of the instabilities become much narrower (see, e.g., the various panels in Figure 17 of Bret et al., 2010b). Hence, the spectral resolution requirements imposed on box size are likely to be exacerbated in the warm cases.

Another related issue when considering the multidimensional simulations is that resolving only the oblique modes is know to be insufficient. In practice, all unstable modes grow simultaneously and impact the subsequent nonlinear evolution. This has also been shown in Bret et al. (2010b, see especially the discussion in Section V.D). Therefore, if the longitudinal instability imposes a stronger restriction on the simulation setup, it must continue to be respected in higher dimensions as well. That is, our 1D analysis is essential to ensure that the linear evolution and the nonlinear saturation are correctly captured in higher dimensional simulations as well.

Chapter 4

Growth of beam-plasma instabilities in presence of inhomogeneity

We explore how the background plasma inhomogeneity alters the growth of electrostatic unstable wave modes of beam-plasma systems. We show that the growth of the instability is local i.e. regions with almost homogeneous background density will the support the growth of the Langmuir waves there, even when they are separated by strongly inhomogeneous regions. We also show that if the background density is continuously varying, this lowers the spatial-growth rate of the instability. However, in such cases, the system grows within the linear regime longer, and upon saturation the beam has lost approximately the same fraction of its initial kinetic energy as found in the uniform case. Thus, inhomogeneities in the IGM are unlikely to suppress the growth of blazar-driven beam-plasma instabilities.

4.1 Introduction

Most, if not all, analytical studies of the beam-plasma instabilities, including those presented here, assume that the plasma is uniformly distributed. This is true, e.g., when the growth rates for oblique modes are computed (Section 1.2.1) and also when higher order perturbative calculations were used to assess the non-linear effects on the linear regime growth rates (Section 1.3.1). In reality the IGM is not uniform. Thus, assessing how the inhomogeneity affects the growth of the unstable wavemodes is essential to determining if beam-plasma instabilities dominate the inverse Compton cooling of blazar-driven pair beams in practice.

A relevant characterization of the inhomogeneity in the beam-plasma system is the inhomogeneity scale length along the beam direction, $\lambda_{\parallel}$. This is typically defined as the length scale over which the number density, n, change by one e-fold along the beam direction, i.e., $\lambda_{\parallel} \equiv |n/(\vec{\nabla} n)_{\parallel}|$. Using cosmological simulations, this scale was estimated for the IGM by Miniati & Elyiv (2013) at different redshifts, z. They find that at mean density $\lambda_{\parallel} \sim 25$, 100, and 400 kpc for $z = 3$, 1 and 0, respectively. The distance travelled by the blazar-induced pair-beams is estimated to be about 1 kpc in one growth time (one e-folding) Miniati & Elyiv (2013). Therefore, the pair beams experience a slowly varying IGM number density.

In presence of the background plasma inhomogeneities, there are two time scales that are important to determine the effect of the inhomogeneity on the growth of the unstable wavemodes. First, the time scale for the growing wave to feel the inhomogeneity, $\tau_{\rm inh}$, and, second, the time scale over which the linear regime growth occurs, $\tau_{\rm g}$, i.e., the time scale after which non-linear effects become important. The growth rates found for the homogeneous background plasma are, then, applicable if $\tau_{\rm inh} \gg \tau_{\rm g}$. When this condition is violated (Breĭzman & Ryutov, 1971), i.e., $\tau_{\rm inh} \lesssim \tau_{\rm g}$, the growth of wavemodes can still occur but at lower rates[1].

We note that, numerical studies (numerical simulations and numerical solutions of the Zakharov equations – approximate evolution equations) for the electrostatic modes (1D) beam plasma instabilities has been already explored in the context of solar radio burst. The motivation for these studies is that simulations for the relaxation of the beams in a homogeneous plasma shows that they form a plateau-type distribution at about 1 Au. However, the detected electron beam at 1 Au (associated with type III radio bursts for example) do not contain any plateau-type features in their momentum distribution. Strong inhomogeneities in the background plasma in such situations are used to account for the longer length of relaxation (slower growth of the instabilities), which is necessary to explain the lack of these plateau-like features at 1 AU Voshchepynets & Krasnoselskikh (2013). These studies are done for diluted ($\alpha \sim 10^{-4}$) but for non-relativistic ($v_b \sim 10^{-2}c$) beams (see, e.g., Thurgood & Tsiklauri, 2016; Voshchepynets & Krasnoselskikh, 2013; Krasnoselskikh et al., 2007; Voshchepynets et al., 2015; Krafft et al., 2013, 2015; Krafft & Volokitin, 2017).

[1] Miniati & Elyiv (2013) incorrectly assumed that the unstable wavemodes do not grow when $\tau_{\rm inh} \lesssim \tau_{\rm g}$. They cited (Breĭzman & Ryutov, 1971) for reference, however, in (Breĭzman & Ryutov, 1971) it is stated explicitly that if this condition is violated the growth can still occur but with slower rates (without any quantification of how much slower).

4.2 Non-uniform background plasmas: complications

For a beam-plasma system with a fixed neutralizing background, we denote phase space distribution function of the beam electron/positron by $f^{\pm}$ and for background electrons by g. The linearized (first-order) Vlasov-Maxwell equations to describe the longitudinal evolution of a linear perturbation are given by

$$\partial_t f_1^{\pm}(x,t,u) + v\partial_x f_1^{\pm}(x,t,u) \pm \frac{e}{m_e} E_1(x,t)\partial_u f_0^{\pm}(u) = 0, \tag{4.1}$$

$$\partial_t g_1(x,t,u) + v\partial_x g_1(x,t,u) - \frac{e}{m_e} E_1(x,t)\partial_u g_0(x,u) = 0, \tag{4.2}$$

$$\partial_x E_1(x,t) = \frac{e}{\epsilon_0}\int \left[f_1^{+}(x,t,u) - f_1^{-}(x,t,u) - g_1(x,t,u)\right] du, \tag{4.3}$$

where, e and m_e are the elementary charge and mass of electrons, $f_0^{\pm}$ and $f_1^{\pm}$ are, respectively, the equilibrium and the first order perturbation of the phase space distribution function of pair-beam plasma particles, g_0 and g_1 are, respectively, the equilibrium and the first order perturbation of the phase space distribution function of background electron plasma, and E_1 is the first order perturbation in the electric field.

Due to the inhomogeneity in the background electrons, the equilibrium distribution function g depends on x. Therefore, trying to solve these equations as an initial value problem using landau procedure (Landau, 1946; Boyd & Sanderson, 2003), i.e. by taking Fourier/Laplace transform for x/t and assuming an initial perturbations for pair-beams plasmas $f_{\rm ini}^{\pm} = f^{\pm}(x,u,t=0)$ and for the electron background plasma $g_{\rm ini} = g(x,u,t=0)$, we get the following equations.

$$-i(\omega - kv) f_1^{\pm}(x,t,u) \pm \frac{e\partial_u f_0^{\pm}(u)}{m_e} E_1(k,\omega) = f_{\rm ini}^{\pm}(k), \tag{4.4}$$

$$-i(\omega - kv) g_1(x,t,u) - \frac{e}{m_e}\int dk^{'} E_1(k-k^{'},\omega)\partial_u g_0(k^{'},u) = g_{\rm ini}(k), \tag{4.5}$$

$$ikE_1(k,\omega) = \frac{e}{\epsilon_0}\int \left[f_1^{+}(k,\omega,u) - f_1^{-}(k,\omega,u) - g_1(k,\omega,u)\right] du. \tag{4.6}$$

Using Equations (4.4, 4.5), we can write that

$$f_1^{+}(k,\omega,u) - f_1^{-}(k,\omega,u) = -i\frac{e}{m_e}\frac{\partial_u(f_0^{+} + f_0^{-})}{\omega - kv} E_1(k,\omega) + i\frac{f_{\rm ini}^{+}(k) - f_{\rm ini}^{-}(k)}{\omega - kv} \tag{4.7}$$

$$g_1(k,\omega,u) = i\frac{e}{m_e}\int dk^{'} E_1(k-k^{'},\omega)\frac{\partial_u g_0(k^{'},u)}{\omega - kv} + i\frac{g_{\rm ini}(k)}{\omega - kv} \tag{4.8}$$

The convolution in Equation (4.8) corresponds to coupling of all Fourier modes of $E_1(k,\omega)$ with all Fourier modes in the background plasma equilibrium number density inhomogeneities. That is, the evolution of the linear perturbation can not be found analytically using the Fourier expansion approach since the Fourier modes coupling with that of the density inhomogeneity is, in general, non-linear.

4.3 Validity of linear growth rate of homogeneous plasma

Here, we quantify the time scales that determine whether the homogeneous plasma linear growth rates are applicable: The time scale for the growing wave to be affected by the inhomogeneity, $\tau_{\rm inh}$, and the time scale on which the linear regime growth occurs, $\tau_{\rm g}$, i.e., the time scale after which non-linear effects become important. To simplify, we here consider only inhomogeneities along the pair-beam direction.

The time scale on which inhomogeneity affects the growing mode can be found using the geometric optics approximation, i.e.,

$$\frac{dk}{dt} = \frac{d\omega}{dx} \sim \frac{\omega_g}{2\lambda_\parallel}, \tag{4.9}$$

where $\lambda_\parallel$ is the inhomogeneity scale length in the pair-beams direction and ω_g is the background plasma frequency at mean density. Therefore, if the width of the oblique modes along the beam direction is $\Delta k_\parallel$, then the inhomogeneity time scale is given by

$$\tau_{\rm inh} \equiv \frac{\Delta k_\parallel}{|dk/dt|} \sim \frac{\Delta k_\parallel 2\lambda_\parallel}{\omega_g}. \tag{4.10}$$

The time scale of oblique modes linear growth is given by

$$\tau_{\rm obl} \equiv \frac{\Lambda^{\rm obl}}{\Gamma^{\rm obl}}, \tag{4.11}$$

where $\Lambda^{\rm obl}$ is the number of e-folding growth for oblique modes before the non-linear effects become important and $\Gamma^{\rm obl}$ is the maximum growth rate of oblique modes.

Therefore, the condition for the validity of linear homogeneous growth rate when background plasmas contains some inhomogeneities, $\tau_{\rm inh} \gg \tau_{\rm obl}$ is

$$\lambda_\parallel \gg \lambda_{\rm min} \equiv \frac{\Lambda^{\rm obl}}{2}\frac{\omega_g}{\Gamma^{\rm obl}}\frac{1}{\Delta k_\parallel}. \tag{4.12}$$

Here, we show using a series of 1D numerical simulations that when the condition is violated, the maximum growth rate is slower than predicted for the homogeneous case but the unstable wave modes still grow and the pair beam energy loss, during the linear regime growth, is approximately the same as that of the homogeneous plasma case.

4.4 Numerical verification

Here we will use 1D simulation to study the effect of the inhomogeneity on the growth of longitudinal unstable modes. For these modes, the width of the instability along the beam direction, using Equation 3.10, is given by

$$\Delta k_{\parallel} \sim \Delta k_{1/2} \sim \frac{2\pi}{1.15008} \left(\frac{\alpha}{\gamma_b^3}\right)^{1/3} \omega_g/c, \tag{4.13}$$

where, α is the beam-to-background number density ratio. The maximum growth rate for the longitudinal unstable modes is given by (Bret et al., 2010b)

$$\Gamma^{\mathrm{L}} \sim \frac{\sqrt{3}}{2^{4/3}} \left(\frac{\alpha}{\gamma_b^3}\right)^{1/3} \omega_g. \tag{4.14}$$

Therefore, for the longitudinal unstable modes

$$\lambda_{\min} = \frac{\Lambda^{\mathrm{L}}}{2} \frac{2^{4/3}}{\sqrt{3}} \frac{1.15008}{2\pi} \left(\frac{\alpha}{\gamma_b^3}\right)^{-2/3} \frac{c}{\omega_g} = 1.33 \left(\frac{\Lambda^{\mathrm{L}}}{10}\right) \left(\frac{\alpha}{\gamma_b^3}\right)^{-2/3} c/\omega_g. \tag{4.15}$$

In the series of 1D simulations presented by Thurgood & Tsiklauri (2016), the pair-beams were dilute with $\alpha = 2.5 \times 10^{-4}$ but moving at non-relativistic speeds, $v_b/c \sim 0.06$. In these simulations, the condition in Equation 4.12 is marginally violated and the growth of the instabilities was shown to occur at lower rates. Here, we will study the case of relativistic dilute pair-beams.

4.4.1 Simulation setup

Here, we present simulations where the background plasmas (electrons and immobile ions) are initially inhomogeneous, and the initial spatial distribution of both ions and electrons of the background is the same. The pair-beam plasmas (electrons and positrons) are initially

Table 4.1. Electrostatic beam-plasma instability simulations with $\alpha = 0.02$, $\gamma_b = 100$, and an initially inhomogeneous background plasmas.

Simulation	L_c [a]	$\Gamma^{\rm sim}/\Gamma^{\rm th}_{\rm uniform}$ [b]	$N_{\rm pc}$ [c]	$\lambda_{\parallel}$ [d]
"Bump"	861	0.75	3491.3	$\sim 80\ c/\omega_p$
"Cosine"	128	0.20	3914.0	$\sim 200\ c/\omega_p$
"Exponential"	125	0.10	4008.0	$\sim 62.5\ c/\omega_p$

[a]The box size, L, in units of skin depth, i.e., $L_c = L\ \omega_p/c$, where, ω_p is the plasma frequency associated with all plasma particles: beam and background particles.

[b]The maximum growth rate found in simulations $\Gamma^{\rm sim}$ normalized to the maximum growth rate predicted theoretically for uniform plasma, $\Gamma^{\rm th}_{\rm uniform} = 8.647 \times 10^{-4}\ \omega_p$, found by solving the dispersion relation in Equation (3.9).

[c]Total number of macro-particles (background electrons and beam electrons and positrons) divided by the total number of computational cells.

[d]The inhomogeneity scale length; the scale length on which the background plasma number density increase by one e–fold. To obtain the degree of violation for the condition of the validity of homogeneous growth rates ($\lambda_{\parallel} \ll \lambda_{\rm min}$), this should be compared to $\lambda_{\rm min} \sim 8.38 \times 10^5\ c/\omega_p$, i.e., this condition is violated by about three order of magnitudes in all simulations.

spatially uniform and moving with $\gamma_b = 100$. In all simulations presented in this section, we set $\alpha = n_b/n_g = 0.002$, where, n_b is the number density of beam particles (both electrons and positrons), and n_g is the number density of background electron plasma. Therefore, for all simulations, $\lambda_{\rm min} \sim 8.38 \times 10^5\ c/\omega_p$.

For all simulations here, we use SHARP-1D (Shalaby et al., 2017) with fifth order interpolation, W^5, to improve the conservation of energy in simulations while conserving the total momentum exactly. Using SHARP with W^5 is essential to avoid the excessive numerical heating typical in most available PIC codes (see chapter 2).We resolve the plasma skin depth c/ω_p by 20 cells, i.e., the cell size is $\Delta x = 0.05\ c/\omega_p$ and use a time step that satisfy the Courant-Friedrichs-Lewy (CFL) stability condition; we used $c\ \Delta t/\Delta x = 0.4$.

Here we analyze the effect of two distinct ways the background inhomogeneity is initialized. First, the "Bump" simulation; a simulation with a bump-in-middle, where the

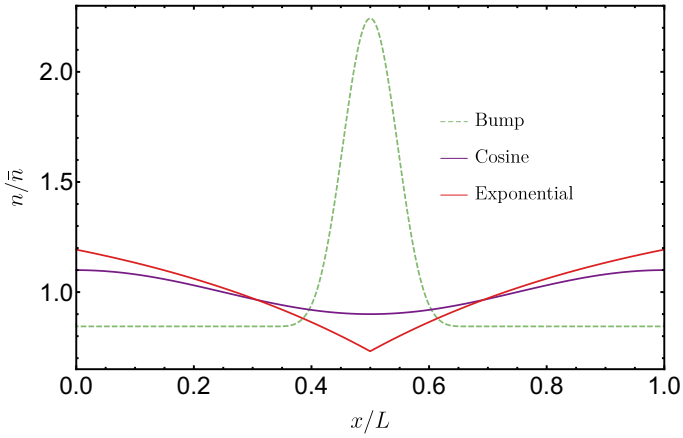

Figure 4.1 Initialization of inhomogeneous background (electrons and fixed ions) plasmas in different simulations in a 1D computational domains of length L. The number density n is normalized by the average number density $\bar{n}$ in different simulations.

periodic simulation domain is divided into three parts, in the first and last part the number density is uniform, while in the middle part, the number density follows a Gaussian distribution (see dashed green curve in Figure 4.1).

Second, a continuously varying background density, for this we present two simulations where, in the first, the background plasma number density is varying as a Cosine wave through the box (with amplitude, $A = 0.1$); purple curve in Figure 4.1. We call this the "Cosine" simulation. In the second, the variation is much faster; the number density at the computational domain is about 1.2 of the average number density, $\bar{n}$, and drops exponentially fast until it reaches $0.7\,\bar{n}$ in the middle of the computational domain and then increases exponentially fast afterwards to reach $1.2\,\bar{n}$ at the other edge of the computational domain(see red curve in Figure 4.1). We call this the "Exponential" simulation.

The momentum distributions (in all simulations) of beam (in the comoving frame) and background plasmas are initialized using thermal distribution with normalized temperatures $\theta_g = \theta_b = 4 \times 10^{-3}$, where, $\theta = k_B T/mc^2$. Other simulation parameters can be found in Table 4.1.

4.4.2 Simulation Results

Figure 4.2 shows the growth of unstable plasma wavemodes even when the condition is severely violated. In Figure 4.3, we show the evolution of the electric potential energy (top) and beam energy loss (bottom). The potential energies grows at smaller rates of about 0.75, 0.2, and 0.1 of the maximum growth rate for uniform plasmas for "Bump", "Cosine" and "Exponential" simulations, respectively.

In all simulations, the level at which the beam energy loss stops occurring with rates comparable to the linear growth rates is the same, i.e., about 20% energy loss. This is also the same level of saturation we obtained from simulations of uniform background density at the same beam parameters.

4.5 Conclusions

In this chapter, we have shown that application of linear growth rates to the cooling of the blazars induced pair-beams can be limited due to the level of the inhomogeneity of the intergalactic medium (IGM). We find the condition for the validity of the uniform growth rates, i.e., the condition that determines whether the unstable modes will feel the effect of background plasmas inhomogeneities during their linear growth.

By means of 1D PIC simulations, we show that even in the presence of severe inhomogeneity, unstable wavemodes instabilities continue to grow. The growth these modes while occurs at lower rates, the system in presence of inhomogeneity stays in the linear regime for longer times and the beam energy loss at the end of linear regime growth occurs at approximately at the same level as in the uniform plasma case. This suggests that blazar-driven beams will remain subject to virulent linear instabilities even in the presence of realistic levels of the inhomogeneity in the IGM.

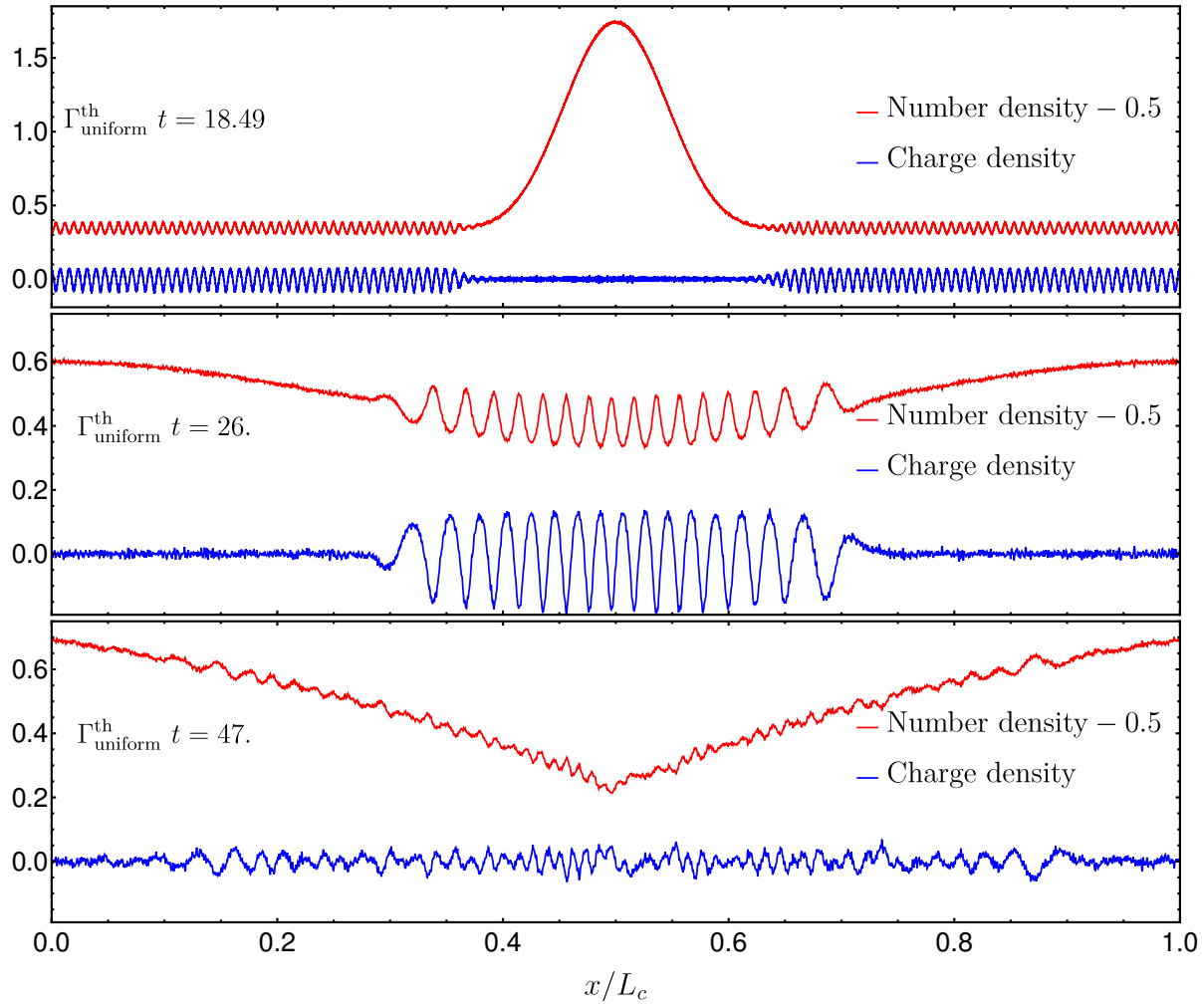

Figure 4.2 Snap shot for the Charge density (red) and number density (blue) in the "Bump" simulations (Top),"Cosine" simulation (middle), and "Exponential" simulations (bottom).

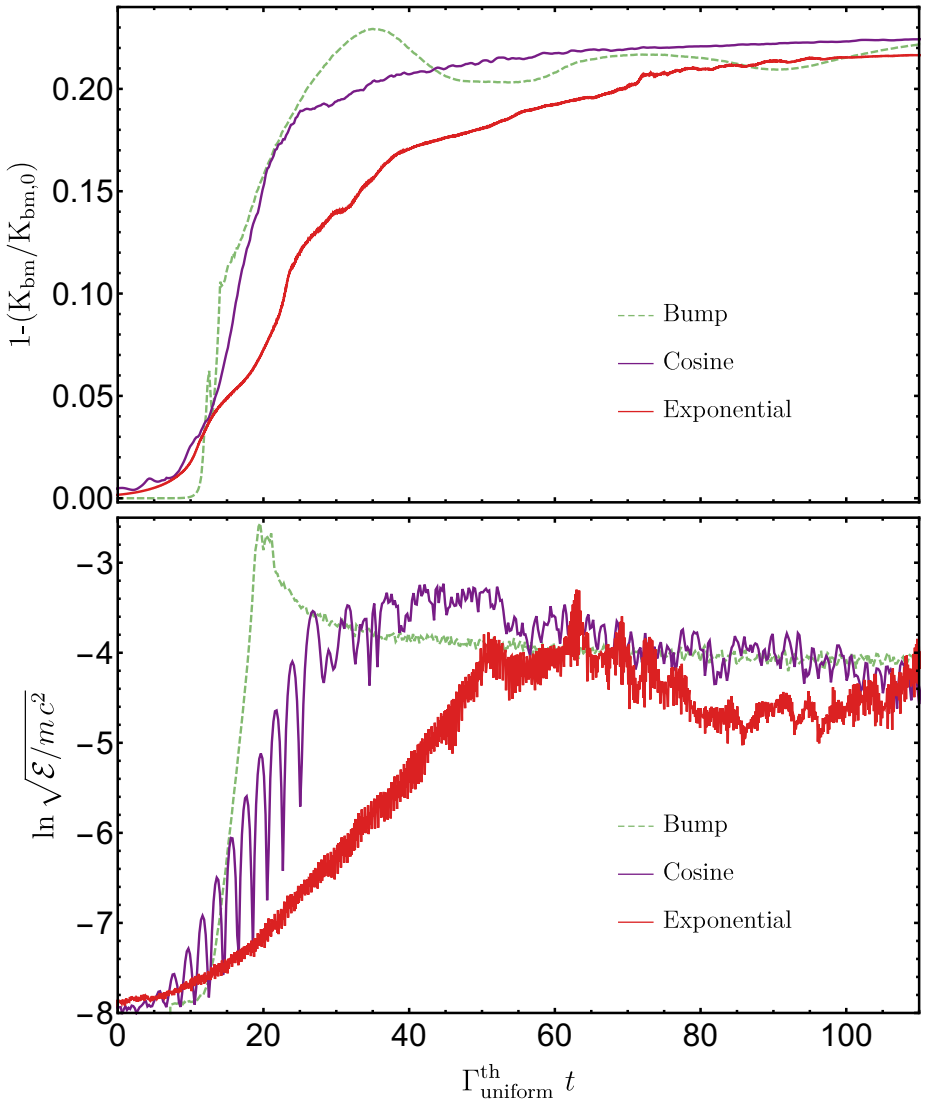

Figure 4.3 Top: Evolution of beam particles fractional energy loss in different simulations with inhomogeneous background plasmas. Bottom: Evolution of the total potential energy per computational particle, $\mathcal{E}$, normalized to the rest mass energy of a computational particle, mc^2. Since the growth in all simulations starts from the Poisson noise, the times are shifted in different simulations to allow for comparisons.

Chapter 5

Conclusions

The extragalactic very high energy gamma-rays sky is dominated by Blazars. The gamma rays produced by Blazars annihilate on the extragalactic background light, producing electron-positron pair beams with TeV energies, i.e., collimated population of ultra-relativistic pairs. The blazar induced pair beams are streaming through the intergalactic medium, itself a cold plasma by the time of the epoch of active galactic nuclei. Together is the Intergalactic medium (fully ionized plasma), the pair-beams constitute a beam-plasma system with extreme parameters, the pair beams are are very dilute, $\alpha \sim 10^{-15}$, ultra-relativistic, $\gamma \sim 10^{6}$, and energetically sub-dominant ($\gamma\alpha \sim 10^{-9}$) Broderick et al. (2012). Any small perturbation in such beam-plasma system is prone to powerful cosmological scale linear beam-plasma instabilities, i.e., a subset of wavemodes propagating at all angle with respect to the beam will grow leading to slowing the pair beam particles. The associated instability growth rates suggest that at least initially these overwhelmingly dominate inverse Compton cooling, currently the only alternative mechanism by which the pair beams lose energy.

These plasmas and general astrophysical plasmas differ from laboratory plasmas in key aspects. They are typically cold $k_B T \ll m_e c^2$, collisionless, and usually contain relativistic sub-populations, e.g, intergalactic medium, interstellar medium, accretion disk. To study the evolution of such plasmas, typically, it is necessary to employ a fully kinetic treatment of the plasmas, as described by Boltzmann equation coupled with Maxwell's equations. Often, linear and quasi-linear analyses for such coupled system are insufficient to understand the full non-linear evolution and saturation of these plasmas, because they study only for the evolution of small perturbations.

Numerical simulations present a key alternative to study the non-linear evolution for

such plasmas. Often, this is accomplished via Particle-in-cell (PIC) algorithms, which combine Eulerian and Lagrangian methods to efficiently solve for plasmas full evolution. However, existing PIC simulations, typically, suffer from a number of fundamental limits. Chief among these is uncontrolled numerical heating. This arises from a number of possible sources, including the accuracy order of most PIC schemes and inconsistent coupling of the Eulerian (cell) and Lagrangian (particle) portions of the code leading to non-vanishing self forces, and physical requirements upon the resolution. Of the latter, the most limiting is the need to resolve the Debye length, which imposes severe limits on the temperatures and timescales PIC simulations can resolve. Therefore, using current implementations of PIC schemes, it is usually not possible to make direct contact with observations or other magneto-hydrodynamics or hydrodynamics simulations for astrophysically relevant plasmas.

Here, we present a number of foundational developments for PIC algorithms. By studying different sources of error, having consistent order of accuracy when approximating different equations and increasing the accuracy of coupling between the grid and the particles, we have developed a new momentum conserving, Spatially Higher-order Accurate, Relativistic PIC code in one dimension (SHARP-1D), that *overcomes* limitations mentioned above. SHARP-1D vastly reduced energy errors and has virtually no numerical heating over very long simulation run times (millions of ω_p^{-1}) without the need to explicitly resolve the Debye length. Therefore, for the first time, it is possible to run simulations relevant for *realistic* plasmas in astrophysical environments. Equally important issue, when numerical schemes are used, is the validation and the convergence of results. The current ways for testing for convergence were shown to be insufficient. A motivation and a demonstration for a new method to check for the convergence for different results in plasma simulations were, also, given: the complement of physical modes captured by the simulation, i.e., lie above the Poisson noise, must grow commensurately with the resolution.

Direct kinetic simulations via existing PIC codes is not possible due to the extreme parameters of the Blazar-induced pair beams. Recent attempts (Sironi & Giannios, 2014; Kempf et al., 2016) to study the evolution of these instabilities at less extreme parameters, using existing PIC implementation, reproduced the linear growth rates only qualitatively due to the high spectral resolution necessary to capture the narrow spectral features of the linearly unstable modes. Moreover, it is clear that the development of the numerical heating in such simulations severely limit the effective instability growth times, likely qualitatively impacting the results.

The spectral resolution presents a new convergence criteria: it should be varied alongside with both spatial and momentum resolutions when convergence studies are performed. The spectral resolution is a general criteria that should be correctly incorporated also in

non-PIC convergence studies when plasma instabilities are important in determining the full evolution of plasmas. We also quantify the required box size in order to correctly capture the narrow features of longitudinal beam plasma instabilities. Using SHARP-1D, we show that failing to have enough spectral resolutions give a slower growth rates that is in quantitative agreement with the prediction of linear theory for such lower spectral resolution. We also show that lower spectral resolution simulations result in lower level of non-linear saturation and potentially lead to wrong physical conclusions. Longitudinal beam plasma instability is not sensitive to plasma (beam or background) temperatures, hence, the quantitative agreement between numerical simulation and the solution for the growth rates when cold-plasma approximation is used.

For electromagnetic (multidimensional) instabilities, the oblique modes are subject to the most virulent instability for parameters relevant to blazars induced pair-beams. The spectral support of the oblique instability is very sensitive to the temperatures of both background and beam plasmas (Bret et al., 2010b). Therefore, a detailed study of the dependence of the width of the oblique instability is essential to determine the required spectral resolution to perform simulations that correctly capture the linear evolution of the instability, however, the maximum growth rate is almost insensitive to the temperatures (Chang et al., 2016). In Appendix B, a study of the effect of temperatures is presented when the fluid approximation of the plasmas is employed, i.e. by computing the fluid growth rates. However, for plasmas with high/relativistic temperature, the fluid approximation is not valid, and thus a complete study of the oblique instability spectral width necessarily requires the solution of the dispersion relation when the kinetic description is employed, i.e., computing the kinetic growth rates.

In this case, the temperatures of the plasmas represent the width of Maxwell-Jüttner distribution employed for different plasma species. Computing the kinetic growth rates is more complicated: the dispersion relation involves complicated integral that typically need to be solved numerically and thus solving the dispersion relation to find the growth rates is much more complicated than in the case of fluid growth rates where the dispersion relation can be written as polynomial. Recently, I got access to the MATLAB code that was used by Bret et al. (2010a) to find the kinetic growth rates. Quantifying the spectral width of the kinetic growth rates as a function of temperature parameters of plasmas is currently a work in progress.

Another important complication is that the linear growth rates can be calculated theoretically only for spatially uniform beam and background plasmas, however, the IGM can not be approximated as a uniform plasma on scales relevant for these growth rates. Therefore, we motivated a condition for the validity of the uniform plasma growth rated; the inhomogeneity scale length (scale length on which the background plasmas number

density increases by one e-fold) has to be much bigger than the length scale on which the plasma waves grows, i.e., the growing plasma wavemodes do not feel the effect of the inhomogeneity. This condition is typically violated for the IGM.

We showed, using 1D PIC simulations, that when this condition is violated, the level of non-linear saturation is similar to the uniform case, and the effect of the inhomogeneity is only pronounced in the growth rates; growth rates found in simulations are smaller than the growth rated predicted for the uniform background plasma. Moreover, we found that when the inhomogeneity is localized, the region where the background plasmas are uniform, wavemodes growth with rates comparable to the uniform plasma growth rates. Therefore, inhomogeneities in the IGM are unlikely to suppress the growth of blazar-driven beam-plasma instabilities as previously claimed.

References

Ackermann, M., Ajello, M., Allafort, A., et al. 2011, ApJ, 743, 171

—. 2012, Science, 338, 1190

—. 2013, ApJ, 765, 54

Ackermann, M., Ajello, M., Atwood, W. B., et al. 2015, ApJ, 810, 14

Ackermann, M., Ajello, M., Albert, A., et al. 2016, Physical Review Letters, 116, 151105

Ardaneh, K., Cai, D., & Nishikawa, K.-I. 2016, ApJ, 827, 124

Ardaneh, K., Cai, D., Nishikawa, K.-I., & Lembége, B. 2015a, ApJ, 811, 57

—. 2015b, ApJ, 811, 57

Besse, N., & Sonnendrücker, E. 2003, Journal of Computational Physics, 191, 341

Birdsall, C. K., & Langdon, A. B. 1991, Plasma Physics via Computer Simulation

Birdsall, C. K., & Maron, N. 1980, Journal of Computational Physics, 36, 1

Bolton, J. S., & Becker, G. D. 2009, MNRAS, 398, L26

Böttcher, M. 2007, Ap&SS, 309, 95

Boyd, T. J. M., & Sanderson, J. J. 2003, The Physics of Plasmas, 544

Brackbill, & J. Forslund, D. 1985, in Multiple time scales, ed. J. U. Brackbill & B. I. Cohen, Vol. 3

Brackbill, J. U. 2016, Journal of Computational Physics, 317, 405

Brambilla, M., ed. 1998, Kinetic theory of plasma waves : homogeneous plasmas, 107

Bret, A. 2006, EPL (Europhysics Letters), 74, 1027

—. 2007, Computer Physics Communications, 176, 362

Bret, A., & Deutsch, C. 2006, Physics of Plasmas, 13, 042106

Bret, A., Gremillet, L., & Bénisti, D. 2010a, Phys. Rev. E, 81, 036402

Bret, A., Gremillet, L., & Dieckmann, M. E. 2010b, Physics of Plasmas, 17, 120501

Breĭzman, B. N., & Ryutov, D. D. 1971, Soviet Journal of Experimental and Theoretical Physics, 33, 220

Breĭzman, B. N., Ryutov, D. D., & Chebotaev, P. Z. 1972, Soviet Journal of Experimental and Theoretical Physics, 35, 741

Broderick, A. E., Chang, P., & Pfrommer, C. 2012, ApJ, 752, 22

Broderick, A. E., Pfrommer, C., Puchwein, E., & Chang, P. 2014, ApJ, 790, 137

Broderick, A. E., Tiede, P., Shalaby, M., et al. 2016, ApJ, 832, 109

Buneman, O. 1959, Physical Review, 115, 503

Buneman, O., Nishikawa, K.-I., & Neubert, T. 1993, in Plasma Physics and Controlled Nuclear Fusion (ITC-4), ed. H. T. D. Guyenne & J. J. Hunt

Caprioli, D., & Spitkovsky, A. 2013, ApJ, 765, L20

Chang, P., Broderick, A. E., & Pfrommer, C. 2012, ApJ, 752, 23

Chang, P., Broderick, A. E., Pfrommer, C., et al. 2014, ApJ, 797, 110

—. 2016, ApJ, 833, 118

Chen, G., Chacón, L., & Barnes, D. C. 2011, Journal of Computational Physics, 230, 7018

Courant, R., Friedrichs, K., & Lewy, H. 1967, IBM Journal of Research and Development, 11, 215

Dawson, J. 1962, Physics of Fluids, 5, 445

de Jager, O. C., Stecker, F. W., & Salamon, M. H. 1994, Nature, 369, 294

Dermer, C. D., Cavadini, M., Razzaque, S., et al. 2011, ApJ, 733, L21

Dieckmann, M. E., Drury, L. O. C., & Shukla, P. K. 2006, 1

Dolag, K., Kachelriess, M., Ostapchenko, S., & Tomàs, R. 2011, ApJ, 727, L4

Domínguez, A., Finke, J. D., Prada, F., et al. 2013, ApJ, 770, 77

Domínguez, A., Primack, J. R., Rosario, D. J., et al. 2011, MNRAS, 410, 2556

Eastwood, J. W. 1991, Computer Physics Communications, 64, 252

Esirkepov, T. Z. 2001, Computer Physics Communications, 135, 144

Faĭnberg, Y. B., Shapiro, V. D., & Shevchenko, V. I. 1969, Soviet Journal of Experimental and Theoretical Physics, 30, 528

Ghisellini, G., Celotti, A., Fossati, G., Maraschi, L., & Comastri, A. 1998, MNRAS, 301, 451

Gilmore, R. C., Somerville, R. S., Primack, J. R., & Domínguez, A. 2012, MNRAS, 422, 3189

Godfrey, B. B. 1974, Journal of Computational Physics, 15, 504

—. 1975, Journal of Computational Physics, 19, 58

Godfrey, B. B., & Vay, J.-L. 2014, Journal of Computational Physics, 267, 1

Gould, R. J., & Schréder, G. P. 1967, Physical Review, 155, 1408

Gremillet, L., Bénisti, D., Lefebvre, E., & Bret, A. 2007, Physics of Plasmas, 14, 040704

H. E. S. S. Collaboration, Abramowski, A., Aharonian, F., et al. 2014, A&A, 562, A145

Haugbølle, T., & Frederiksen, J. T. & Nordlund, A. 2013, Physics of Plasmas, 20, 062904

Hockney, R. W., & Eastwood, J. W. 1988, Computer simulation using particles

Kaplan, S. A., & Tsytovich, V. N. 1968, Soviet Ast., 11, 956

Kempf, A., Kilian, P., & Spanier, F. 2016, A&A, 585, A132

Kneiske, T. M., Bretz, T., Mannheim, K., & Hartmann, D. H. 2004, A&A, 413, 807

Krafft, C., & Volokitin, A. 2017, Journal of Plasma Physics, 83, 705830201

Krafft, C., Volokitin, A. S., & Krasnoselskikh, V. V. 2013, ApJ, 778, 111

—. 2015, ApJ, 809, 176

Krasnoselskikh, V. V., Lobzin, V. V., Musatenko, K., et al. 2007, Journal of Geophysical Research (Space Physics), 112, A10109

Lamberts, A., Chang, P., Pfrommer, C., et al. 2015, ApJ, 811, 19

Landau, L. D. 1946, J. Phys.(USSR), 10, 25, [Zh. Eksp. Teor. Fiz.16,574(1946)]

Langdon, A. B. 1973, Journal of Computational Physics, 12, 247

Lapenta, G. 2016, ArXiv e-prints, arXiv:1602.06326

Lapenta, G., & Markidis, S. 2011, Physics of Plasmas, 18, 072101

Lehe, R., Kirchen, M., Godfrey, B. B., Maier, A. R., & Vay, J.-L. 2016, Phys. Rev. E, 94, 053305

Lewis, H. R. 1970, Journal of Computational Physics, 6, 136

Lipatov, A. S. 2002, The hybrid multiscale simulation technology an introduction with application to astrophysical and laboratory plasmas

Lyutikov, M., Sironi, L., Komissarov, S., & Porth, O. 2016, ArXiv e-prints, arXiv:1603.05731

Mannheim, K. 1993, A&A, 269, 67

Markidis, S., & Lapenta, G. 2011, Journal of Computational Physics, 230, 7037

McKinstrie, C. J., Giacone, R. E., & Startsev, E. A. 1999, Physics of Plasmas, 6, 463

McQuinn, M., Lidz, A., Zaldarriaga, M., et al. 2009, ApJ, 694, 842

Melrose, D. B. 1986, Instabilities in Space and Laboratory Plasmas, 288

Miller, K. A., & Stone, J. M. 1999, in Bulletin of the American Astronomical Society, Vol. 31, American Astronomical Society Meeting Abstracts, 1510

Miniati, F., & Elyiv, A. 2012, ArXiv e-prints, arXiv:1208.1761

—. 2013, ApJ, 770, 54

Neronov, A., & Semikoz, D. V. 2009, Phys. Rev. D, 80, 123012

Neronov, A., Semikoz, D. V., Tinyakov, P. G., & Tkachev, I. I. 2011, A&A, 526, 90

Neronov, A., & Vovk, I. 2010, Science, 328, 73

Nishikawa, K.-I., Frederiksen, J. T., Nordlund, Å., et al. 2016, ApJ, 820, 94

Nuter, R., & Tikhonchuk, V. 2016, Journal of Computational Physics, 305, 664

Park, J., Caprioli, D., & Spitkovsky, A. 2015, Physical Review Letters, 114, 085003

Philippov, A. A., Spitkovsky, A., & Cerutti, B. 2015, ApJ, 801, L19

Prokhorov, D. A., & Moraghan, A. 2016, MNRAS, 457, 2433

Ramirez-Ruiz, E., Nishikawa, K.-I., & Hededal, C. B. 2007, ApJ, 671, 1877

Riquelme, M. A., Quataert, E., & Verscharen, D. 2016, ApJ, 824, 123

Riquelme, M. A., & Spitkovsky, A. 2009, ApJ, 694, 626

Rossmanith, J. A., & Seal, D. C. 2011, Journal of Computational Physics, 230, 6203

Salamon, M. H., & Stecker, F. W. 1998, ApJ, 493, 547

Schlickeiser, R., Ibscher, D., & Supsar, M. 2012, ApJ, 758, 102

Schlickeiser, R., Krakau, S., & Supsar, M. 2013a, ArXiv e-prints, arXiv:1308.4594

—. 2013b, ApJ, 777, 49

Shalaby, M., Broderick, A. E., Chang, P., et al. 2017, ApJ, 841, 52

Sironi, L., & Giannios, D. 2014, ApJ, 787, 49

Sironi, L., Spitkovsky, A., & Arons, J. 2013, ApJ, 771, 54

Smith, D. F., & Fung, P. C. W. 1971, Journal of Plasma Physics, 5, 1

Spitkovsky, A. 2005, in American Institute of Physics Conference Series, Vol. 801, Astrophysical Sources of High Energy Particles and Radiation, ed. T. Bulik, B. Rudak, & G. Madejski, 345–350

Spitkovsky, A. 2008, ApJ, 682, L5

Stecker, F. W., de Jager, O. C., & Salamon, M. H. 1992, ApJ, 390, L49

Stockem Novo, A., Bret, A., Fonseca, R. A., & Silva, L. O. 2016, Plasma Physics and Controlled Fusion, 58, 014005

Takahashi, K., Mori, M., Ichiki, K., & Inoue, S. 2012, ApJ, 744, L7

Tavecchio, F., Ghisellini, G., Bonnoli, G., & Foschini, L. 2011, MNRAS, 414, 3566

Tavecchio, F., Ghisellini, G., Foschini, L., et al. 2010, MNRAS, 406, L70

Taylor, A. M., Vovk, I., & Neronov, A. 2011, A&A, 529, A144

Thurgood, J. O., & Tsiklauri, D. 2016, Journal of Plasma Physics, 82, 905820604

Tiede, P., Broderick, A. E., Shalaby, M., et al. 2017a, ArXiv e-prints, arXiv:1702.02585

—. 2017b, ArXiv e-prints, arXiv:1702.02586

Umeda, T., Omura, Y., Tominaga, T., & Matsumoto, H. 2003, Computer Physics Communications, 156, 73

Urry, C. M., & Padovani, P. 1995, PASP, 107, 803

Villasenor, J., & Buneman, O. 1992, Computer Physics Communications, 69, 306

Voshchepynets, A., & Krasnoselskikh, V. 2013, Annales Geophysicae, 31, 1379

Voshchepynets, A., Krasnoselskikh, V., Artemyev, A., & Volokitin, A. 2015, ApJ, 807, 38

Vovk, I., Taylor, A. M., Semikoz, D., & Neronov, A. 2012, ApJ, 747, L14

Xu, X., Yu, P., Martins, S. F., et al. 2013, Computer Physics Communications, 184, 2503

Yu, P., Xu, X., Decyk, V. K., et al. 2015, Computer Physics Communications, 192, 32

Zhu, Q., Hernquist, L., & Li, Y. 2015, ApJ, 800, 6

APPENDICES

Appendix A

SHARP-1D appendices

A.1 Momentum conservation

For the purpose of comparison, we start by calculating the correct interaction force for point particles in 1D, by using

$$q_0\mathbb{E}_0 = m_0\epsilon_0\omega_0 \quad \& \quad hN_{cp} = \frac{\omega_0 L/c}{\sum_s(\bar{Q}_s^2 N_s)/\bar{M}_s} = \frac{\omega_0 q_0^2}{m_0 c\epsilon_0\omega_0^2} = \frac{q_0^2}{\epsilon_0 q_0\mathbb{E}_0} \quad \Longrightarrow \quad \frac{1}{\epsilon_0 q_0\mathbb{E}_0} = \frac{hN_{cp}}{q_0^2}. \tag{A.1}$$

Therefore, the correct interaction term in 1D for point-particles ($m = 0$) (in code units) is given by

$$\bar{F}_{\rm int} = \frac{Q_1 Q_2}{2\epsilon_0}\frac{1}{q_0\mathbb{E}_0}\begin{cases}+1 & x_2 > x_1 \\ -1 & x_2 < x_1\end{cases} = \frac{\bar{Q}_1\bar{Q}_2 h}{2}N_{cp}\begin{cases}+1 & x_2 > x_1 \\ -1 & x_2 < x_1\end{cases}. \tag{A.2}$$

On the other hand, the force on a macro-particle, with charge q_α and centered at $x_\alpha\epsilon[0, L]$ on a periodic box, is given by $\bar{F}_\alpha \equiv F_\alpha/(q_0\mathbb{E}_0) = \bar{Q}_\alpha\bar{E}_\alpha$, where

$$\bar{E}_\alpha = \int_0^L \bar{E}(x)S^m[(x - x_\alpha)/\Delta x]dx = \sum_{k=0}^{N_c-1}\int_{x_{k-1/2}}^{x_{k+1/2}} \bar{E}(x)S^m dx = \sum_{k=0}^{N_c-1}\int_{x_k}^{x_{k+1}} \bar{E}(x)S^m dx \tag{A.3}$$

By defining

$$N_{cp} \equiv \frac{N_c}{\sum_s(\bar{Q}_s^2 N_s)/\bar{M}_s} = \frac{1}{n_0\Delta x} \qquad \& \qquad N_{pc} \equiv \frac{1}{N_{cp}} \qquad \& \qquad W_{k,i}^m \equiv W^m\left[(\bar{x}_k - \bar{x}_i)/h\right]. \tag{A.4}$$

The exact equations for the fields on the grid edges are given by Equations (2.35, 2.36), these can be written as

$$\bar{E}_{k+1} = \bar{E}_k + h\bar{\rho}_{k+\frac{1}{2}} \qquad \& \qquad \bar{\rho}_{k+\frac{1}{2}} = N_{cp} \sum_s \bar{Q}_s \sum_{i_s} W^m_{k+\frac{1}{2},i_s}. \tag{A.5}$$

The solution of Equation (A.5) can be expressed as

$$\begin{aligned} \bar{E}_k &= \bar{E}_0 + h\sum_{j=0}^{k-1} \bar{\rho}_{j+\frac{1}{2}} = \bar{E}_0 - h\sum_{j=k}^{N_c-1} \bar{\rho}_{j+\frac{1}{2}} = \bar{E}_0 + \frac{h}{2}\sum_{j=0}^{k-1} \bar{\rho}_{j+\frac{1}{2}} - \frac{h}{2}\sum_{j=k}^{N_c-1} \bar{\rho}_{j+\frac{1}{2}} \\ &= \bar{E}_0 - \frac{h}{2}\bar{\rho}_{k+\frac{1}{2}} + \frac{h}{2}\sum_{j=0}^{N_c-1} A_{jk}\bar{\rho}_{j+\frac{1}{2}}, \end{aligned} \tag{A.6}$$

where A_{jk} is anti-symmetric matrix given by

$$A_{jk} = \begin{cases} +1 & j < k, \\ 0 & j = k, \\ -1 & j > k. \end{cases} \tag{A.7}$$

Two possible, second order accurate, approximations for Equation (A.3) can be written as follows

$$\bar{F}_{i_s} \approx \begin{cases} \bar{Q}_s \sum_{k=0}^{N_c-1} \bar{E}_k W^m_{k,i_s}. & \text{(A.8)} \\ \frac{\bar{Q}_s}{2} \sum_{k=0}^{N_c-1} \left[\bar{E}_k + \bar{E}_{k+1}\right] W^m_{k+\frac{1}{2},i_s} = \frac{\bar{Q}_\alpha}{2} \sum_{k=0}^{N_c-1} \bar{E}_k \left[W^m_{k+\frac{1}{2},i_s} + W^m_{k-\frac{1}{2},i_s}\right]. & \text{(A.9)} \end{cases}$$

A.1.1 Non momentum conserving second order scheme: approximation (A.8)

If we use (A.6) and net-charge neutrality, i.e., $\sum_k \bar{\rho}_k = \sum_k \bar{\rho}_{k+\frac{1}{2}} = 0$, then the total force on all macro-particles is given by

$$\begin{aligned} \bar{F}_{Net} &= \sum_s \sum_{i_s} \bar{F}_{i_s} = \sum_k \bar{E}_k \sum_s \bar{Q}_s \sum_{i_s} W^m_{k,i_s} = N_{pc} \sum_k \bar{E}_k \bar{\rho}_k \\ &\quad - N_{pc}\frac{h}{2}\sum_k \bar{\rho}_k \bar{\rho}_{k+1/2} + N_{pc}\frac{h}{2}\sum_{j,k} A_{jk}\bar{\rho}_k\bar{\rho}_{j+\frac{1}{2}}. \end{aligned} \tag{A.10}$$

Therefore, the net-force on the system does not depend on the choice of E_0 (because of charge neutrality), and since using higher interpolation functions makes the variation in the interpolated density smoother, it decreases both terms in Equation (A.10), i.e., using higher order interpolation *improves* the momentum conservation.

Origin of momentum non-conservation: self-forces and wrong interaction forces

To see that, we examine the interpolated force in case of having only two macro-particles. Using $\bar{Q}_1 + \bar{Q}_2 = 0$, $\sum_k W^m_{k,i_s} = 1$, and

$$\bar{\rho}_{j+\frac{1}{2}} = N_{cp}\left[\bar{Q}_1 W^m_{j+\frac{1}{2},1} + \bar{Q}_2 W^m_{j+\frac{1}{2},2}\right],$$

the force on macro-particle at x_1 is given by

$$\begin{aligned}
\bar{F}_1 &= \bar{Q}_1 \sum_{k=0}^{Nc-1}\left(\bar{E}_0 - \frac{h}{2}\bar{\rho}_{k+\frac{1}{2}} + \frac{h}{2}\sum_{j=0}^{Nc-1} A_{jk}\bar{\rho}_{j+\frac{1}{2}}\right) W^m_{k,1} \\
&= \bar{Q}_1 E_0 - \frac{\bar{Q}_1 h}{2} N_{cp} \sum_k \left[\bar{Q}_1 W^m_{k+\frac{1}{2},1} + \bar{Q}_2 W^m_{k+\frac{1}{2},2}\right] W^m_{k,1} \\
&\quad + \frac{\bar{Q}_1 h}{2} N_{cp} \sum_{j,k} A_{jk}\left[\bar{Q}_1 W^m_{k+\frac{1}{2},1} + \bar{Q}_2 W^m_{k+\frac{1}{2},2}\right] W^m_{k,1} \\
&= \bar{Q}_1 E_0 + \frac{\bar{Q}_1^2 h}{2} N_{cp}\left[\sum_{j,k} A_{jk} W^m_{j+\frac{1}{2},1} W^m_{k,1} - \sum_k W^m_{k+\frac{1}{2},1} W^m_{k,1}\right] \\
&\quad + \frac{\bar{Q}_2 \bar{Q}_1 h}{2} N_{cp}\left[\sum_{j,k} A_{jk} W^m_{j+\frac{1}{2},2} W^m_{k,1} - \sum_k W^m_{k+\frac{1}{2},2} W^m_{k,1}\right].
\end{aligned} \tag{A.11}$$

Therefore, the non-vanishing self-force, $\bar{F}_{\text{self}}$, and the numerical interaction force, $\bar{F}_{\text{int}}$, are given by

$$\bar{F}_{\text{self}} = \frac{\bar{Q}_1^2 h}{2} N_{cp}\left[\sum_{j,k} A_{jk} W^m_{j+\frac{1}{2},1} W^m_{k,1} - \sum_k W^m_{k+\frac{1}{2},1} W^m_{k,1}\right] \neq 0 \tag{A.12}$$

$$\bar{F}_{\text{int}} = \frac{\bar{Q}_2 \bar{Q}_1 h}{2} N_{cp}\left[\sum_{j,k} A_{jk} W^m_{j+\frac{1}{2},2} W^m_{k,1} - \sum_k W^m_{k+\frac{1}{2},2} W^m_{k,1}\right]. \tag{A.13}$$

Therefor, the self-force ($\sim h/N_{pc} = L/N_p$) here vanishes only in the limit of infinite number of macro-particles $N_p \to \infty$.

A.1.2 Momentum conserving second order scheme: approximation (A.9)

If we use (A.6) and net-charge neutrality, i.e., $\sum_k \bar{\rho}_k = \sum_k \bar{\rho}_{k+1/2} = 0$, and

$$\bar{E}_k + \bar{E}_{k+1} = 2\bar{E}_0 + h\sum_{j=0}^{k-1} \bar{\rho}_{j+\frac{1}{2}} - h\sum_{j=k+1}^{N_c-1} \bar{\rho}_{j+\frac{1}{2}} = 2\bar{E}_0 + h\sum_{j=0}^{N_c-1} A_{jk}\bar{\rho}_{j+\frac{1}{2}}. \quad (A.14)$$

The net-force is, then, given by

$$\begin{aligned} \bar{F}_{Net} &= \sum_s \sum_{i_s} \bar{F}_{i_s} = \sum_k \frac{\bar{E}_k + \bar{E}_{k+1}}{2} \sum_s \bar{Q}_s \sum_{i_s} W^m_{k+\frac{1}{2},i_s} = N_{pc} \sum_k \frac{\bar{E}_k + \bar{E}_{k+1}}{2} \bar{\rho}_{k+\frac{1}{2}} \\ &= \frac{hN_{pc}}{2} \sum_{j,k} A_{jk}\bar{\rho}_{j+\frac{1}{2}}\bar{\rho}_{k+1/2} = 0. \end{aligned} \quad (A.15)$$

Therefore, the net-force on the system, again, does not depend on the choice of E_0 (because of charge neutrality), and it is always exactly zero, therefore, the momentum is exactly conserved. Hence we call this a momentum conserving scheme.

Vanishing of the self-forces exactly

To see that, we examine the interpolated force in case of having only two macro-particles. Using $\bar{Q}_1 + \bar{Q}_2 = 0$, $\sum_k W^m_{k,i_s} = 1$ and

$$\bar{\rho}_{j+\frac{1}{2}} = N_{cp}\left[\bar{Q}_1 W^m_{j+\frac{1}{2},1} + \bar{Q}_2 W^m_{j+\frac{1}{2},2}\right],$$

the force on macro-particle at x_1 is given by

$$\begin{aligned} \bar{F}_1 &= \bar{Q}_1 \sum_{k=0}^{Nc-1} \frac{\bar{E}_k + \bar{E}_{k+1}}{2} W^m_{k+\frac{1}{2},1} = \bar{Q}_1 \sum_{k=0}^{Nc-1} \left[E_0 + \frac{h}{2}\sum_{j=0}^{Nc-1} A_{jk}\bar{\rho}_{j+\frac{1}{2}}\right] W^m_{k+\frac{1}{2},1} \\ &= \bar{Q}_1\bar{E}_0 + \frac{\bar{Q}_1 h}{2} N_{cp} \sum_{j,k} A_{jk}\left[\bar{Q}_1 W^m_{j+\frac{1}{2},1} + \bar{Q}_2 W^m_{j+\frac{1}{2},2}\right] W^m_{k+\frac{1}{2},1} \\ &= \bar{Q}_1\bar{E}_0 + \frac{\bar{Q}_1\bar{Q}_2 h}{2} N_{cp} \sum_{j,k} A_{jk} W^m_{j+\frac{1}{2},2} W^m_{k+\frac{1}{2},1}. \end{aligned} \quad (A.16)$$

Therefore, the vanishing self-force, $\bar{F}^{\rm self}$, and the numerical interaction force, $\bar{F}^{\rm int}$, are given by

$$\bar{F}^{\rm self} = \frac{\bar{Q}_1^2 h}{2} N_{cp} \sum_{j,k} A_{jk} W^m_{j+\frac{1}{2},1} W^m_{k+\frac{1}{2},1} = 0 \tag{A.17}$$

$$\bar{F}^{\rm int} = \frac{\bar{Q}_1 \bar{Q}_2 h}{2} N_{cp} \sum_{j,k} A_{jk} W^m_{j+\frac{1}{2},2} W^m_{k+\frac{1}{2},1}. \tag{A.18}$$

We can see from comparing Equations (A.2) and (A.17) that the numerically calculated interaction force is shorter in range, and that the usage of higher order interpolation (larger macro-particles) results in smoothing the interaction forces.

A.1.3 Filtering for momentum conserving scheme: non-vanishing self-forces

Here, we show that filtering of the grid charge densities, e.g. 1D equivalence of filtering implemented in TRISTAN-MP, lead to a non-vanishing self-forces and a violation of momentum conservation.

After one-filter, the filtered charge densities $\bar{\rho}^{\rm f}_k$ are given by

$$\bar{\rho}^{\rm f}_{k+\frac{1}{2}} = \frac{\bar{\rho}_{k-\frac{1}{2}} + 2\bar{\rho}_{k+\frac{1}{2}} + \bar{\rho}_{k+\frac{3}{2}}}{4}. \tag{A.19}$$

Therefore, for a momentum conserving scheme, e.g., Equation (A.9), if we used (A.14) and replaced $\rho_{k+1/2}$ by $\rho^{\rm f}_{k+1/2}$, the net force is given by

$$\begin{aligned} \bar{F}_{Net} &= \sum_k \frac{\bar{E}_k + \bar{E}_{k+1}}{2} \sum_s \bar{Q}_s \sum_{i_s} W^m_{k+\frac{1}{2},i_s} \\ &= \frac{N_{pc} h}{2} \sum_{k,j} A_{jk} \bar{\rho}^{\rm f}_{k+\frac{1}{2}} \bar{\rho}_{k+\frac{1}{2}} \\ &= \frac{N_{pc} h}{8} \sum_{k,j} A_{jk} \left(\bar{\rho}_{k-\frac{1}{2}} + \bar{\rho}_{k+\frac{3}{2}} \right) \bar{\rho}_{k+\frac{1}{2}} \neq 0. \end{aligned} \tag{A.20}$$

Which shows that filtering the grid deposited moment (grid charge density) leads to violation of momentum conservation in otherwise a momentum conserving scheme.

To see the origin of such violation we look, as we did before, at the interpolated force in case of having only two macro-particles, using $\bar{Q}_1 + \bar{Q}_2 = 0$, $\sum_k W^m_{k,i_s} = 1$ and

$$\bar{\rho}_{j+\frac{1}{2}} = N_{cp}\left[\bar{Q}_1 W^m_{j+\frac{1}{2},1} + \bar{Q}_2 W^m_{j+\frac{1}{2},2}\right]. \tag{A.21}$$

Therefore,

$$\bar{\rho}^{\rm f}_{j+\frac{1}{2}} = \frac{N_{cp}}{4}\left[\bar{Q}_1\left(W^m_{j-\frac{1}{2},1} + 2W^m_{j+\frac{1}{2},1} + W^m_{j+\frac{3}{2},1}\right) + \bar{Q}_2\left(W^m_{j-\frac{1}{2},2} + 2W^m_{j+\frac{1}{2},2} + W^m_{j+\frac{3}{2},2}\right)\right], \tag{A.22}$$

the force on macro-particle at x_1 is given by

$$\begin{aligned}
\bar{F}_1 &= \bar{Q}_1 \sum_{k=0}^{Nc-1} \frac{\bar{E}_k + \bar{E}_{k+1}}{2} W^m_{k+\frac{1}{2},1} = \bar{Q}_1 \sum_{k=0}^{Nc-1}\left[E_0 + \frac{h}{2}\sum_{j=0}^{Nc-1} A_{jk}\bar{\rho}^{\rm f}_{j+\frac{1}{2}}\right] W^m_{k+\frac{1}{2},1} \\
&= \bar{Q}_1\bar{E}_0 + \frac{\bar{Q}_1 h}{4} N_{cp}\sum_{j,k} A_{jk}\left[\bar{Q}_1 W^m_{j+\frac{1}{2},1} + \bar{Q}_2 W^m_{j+\frac{1}{2},2}\right] W^m_{k+\frac{1}{2},1} \\
&\quad + \frac{\bar{Q}_1 h}{8} N_{cp}\sum_{j,k} A_{jk}\left[\bar{Q}_1\left(W^m_{j+\frac{3}{2},1} + W^m_{j-\frac{1}{2},1}\right) W^m_{k+\frac{1}{2},1} + \bar{Q}_2\left(W^m_{j+\frac{3}{2},2} + W^m_{j-\frac{1}{2},2}\right) W^m_{k+\frac{1}{2},1}\right] \\
&= \bar{Q}_1\bar{E}_0 + \frac{\bar{Q}_1\bar{Q}_2 h}{4} N_{cp}\left[\sum_{j,k} A_{jk} W^m_{j+\frac{1}{2},2} W^m_{k+\frac{1}{2},1} + \frac{1}{2}\sum_{j,k} A_{jk}\left(W^m_{j+\frac{3}{2},2} + W^m_{j-\frac{1}{2},2}\right) W^m_{k+\frac{1}{2},1}\right] \\
&\quad + \frac{\bar{Q}_1^2 h}{8} N_{cp}\sum_{j,k} A_{jk}\left(W^m_{j+\frac{3}{2},1} + W^m_{j-\frac{1}{2},1}\right) W^m_{k+\frac{1}{2},1}.
\end{aligned} \tag{A.23}$$

Therefore, filtering leads to wrong interaction forces and a non-vanishing self force given by

$$\bar{F}_1^{\rm \ self} = \frac{\bar{Q}_1^2 h}{8} N_{cp}\sum_{j,k} A_{jk}\left(W^m_{j+\frac{3}{2},1} + W^m_{j-\frac{1}{2},1}\right) W^m_{k+\frac{1}{2},1} \neq 0.$$

A.2 Shape and weight functions explicit form

If we define $y = (x - x_i)/\Delta x = (\bar{x} - \bar{x}_i)/h$, the shape functions, $S^m(y)$, assumed for the macro-particles and the corresponding weight functions, $W^m(y)$, used in the interpolation steps in the code are given in Table A.1.

Table A.1. Shape and weight functions implemented in SHARP-1D.

m	$S^m(y)$	$W^m(y)$
0	$\delta(y)$	$\begin{cases} 1 & 0 \le \lvert y\rvert \le \frac{1}{2} \\ 0 & \text{Otherwise} \end{cases}$
1	$\frac{1}{\Delta x}\begin{cases} 1 & 0 \le \lvert y\rvert \le \frac{1}{2} \\ 0 & \text{Otherwise} \end{cases}$	$\begin{cases} 1-\lvert y\rvert & 0 \le \lvert y\rvert < 1 \\ 0 & \text{Otherwise} \end{cases}$
2	$\frac{1}{\Delta x}\begin{cases} 1-\lvert y\rvert & 0 \le \lvert y\rvert < 1 \\ 0 & \text{Otherwise} \end{cases}$	$\begin{cases} \frac{3}{4}-y^2 & 0 < \lvert y\rvert < \frac{1}{2} \\ \frac{1}{8}(3-2\lvert y\rvert)^2 & \frac{1}{2} \le \lvert y\rvert < \frac{3}{2} \\ 0 & \text{Otherwise} \end{cases}$
3	$\frac{1}{\Delta x}\begin{cases} \frac{3}{4}-y^2 & 0 < \lvert y\rvert < \frac{1}{2} \\ \frac{1}{8}(3-2\lvert y\rvert)^2 & \frac{1}{2} \le \lvert y\rvert < \frac{3}{2} \\ 0 & \text{Otherwise} \end{cases}$	$\begin{cases} \frac{2}{3}-y^2+\lvert y\rvert^3/2 & 0 < \lvert y\rvert < 1 \\ \frac{1}{6}(2-\lvert y\rvert)^3 & 1 \le \lvert y\rvert < 2 \\ 0 & \text{Otherwise} \end{cases}$
4	$\frac{1}{\Delta x}\begin{cases} \frac{2}{3}-y^2+\lvert y\rvert^3/2 & 0 < \lvert y\rvert < 1 \\ \frac{1}{6}(2-\lvert y\rvert)^3 & 1 \le \lvert y\rvert < 2 \\ 0 & \text{Otherwise} \end{cases}$	$\begin{cases} \frac{115}{192}-\frac{5y^2}{8}+\frac{y^4}{4} & 0 < \lvert y\rvert < \frac{1}{2} \\ \frac{1}{96}\left[55+20\lvert y\rvert-120y^2+80\lvert y\rvert^3-16y^4\right] & \frac{1}{2} \le \lvert y\rvert < \frac{3}{2} \\ \frac{1}{384}(5-2\lvert y\rvert)^4 & \frac{3}{2} \le \lvert y\rvert < \frac{5}{2} \\ 0 & \text{Otherwise} \end{cases}$
5	$\frac{1}{\Delta x}\begin{cases} \frac{115}{192}-\frac{5y^2}{8}+\frac{y^4}{4} & 0 < \lvert y\rvert < \frac{1}{2} \\ \frac{1}{96}\left[55+20\lvert y\rvert-120y^2 \right. & \\ \left. +80\lvert y\rvert^3-16y^4\right] & \frac{1}{2} \le \lvert y\rvert < \frac{3}{2} \\ \frac{1}{384}(5-2\lvert y\rvert)^4 & \frac{3}{2} \le \lvert y\rvert < \frac{5}{2} \\ 0 & \text{Otherwise} \end{cases}$	$\begin{cases} \frac{11}{20}-\frac{y^2}{2}+\frac{y^4}{4}-\frac{\lvert y\rvert^5}{12} & 0 \le \lvert y\rvert \le 1 \\ \frac{17}{40}+\frac{5\lvert y\rvert}{8}-\frac{7y^2}{4}+\frac{5\lvert y\rvert^3}{4}-\frac{3y^4}{8}+\frac{\lvert y\rvert^5}{24} & 1 < \lvert y\rvert < 2 \\ \frac{1}{120}(3-\lvert y\rvert)^5 & 2 \le \lvert y\rvert < 3 \\ 0 & \text{Otherwise} \end{cases}$

A.3 Aliasing

The Fourier components of grid quantities, in 1D, g_k are such that $g_k = g_{k+pk_g}$, where p is some integer and $k_g = 2\pi/\Delta x$ is the wave mode associated with the cell-size Δx on that physical grid. Therefore, for a continuous particles number density $n(x)$, the Fourier component of the grid charge density is given by (Birdsall & Langdon, 1991)

$$\tilde{\rho}_k = \sum_{p=-\infty}^{\infty} \tilde{n}(k - pk_g)\, \tilde{S}(k - pk_g), \tag{A.24}$$

where $\tilde{S}(k)$ is Fourier transform of our interpolation function and $\tilde{n}(k)$ is Fourier transform of $n(x)$. Therefore, all aliases of k (wave modes that differ from k by integer number of k_g) contribute when grid-quantities are calculated. Clearly, this will feedback on the particle quantities, when the grid-quantities are used to calculate the force on the particles to evolve them. The strength of the coupling between aliases (the source of this error) depends on how fast $\tilde{S}^m(k)$ falls off for large k, as can be seen in Equation (A.24).

The Fourier transform of our interpolation functions (spline functions of order m, see Table A.1) is given by

$$\tilde{S}^m(k) = \left[\frac{\sin(k\Delta x/2)}{k\Delta x/2}\right]^m. \tag{A.25}$$

Therefore, Using higher order interpolation functions (larger m) in our code leads to a decrease in the strength of the couplings between grid wave modes and their aliases), which results in improvements in energy conservation as seen in Section 2.4.1.

A.4 Poisson noise

Here we calculate the noise when a finite number of computational particles are used to represent a uniform distribution function. We calculate the total energy density due to such noise in Appendix A.4.1 and then find the power spectrum for such noise in Appendix A.4.2. In Appendix A.4.3, we calculate the temperature, θ_p, set by the energy in such noise.

A.4.1 Average potential energy from uniformly distributed macro-particles

Using Equation (2.10) and the first equation in (2.2), we can write the electric field associated with plasma particles on a periodic box of length L, i.e., $x_{i_s} \in [0, L)$ as follows

$$E(x) - E_0 = \sum_s \frac{Q_s}{\epsilon_0} \sum_{i_s}^{N_s} q^m(x, x_{i_s}). \tag{A.26}$$

Where, $q^m(x, x_{i_s}) = \int_0^x dx^{'} S^m(x^{'}, x_{i_s})$. The periodicity of the box implies that the plasma is neutral. Therefore,

$$E_L - E_0 = 0 = \frac{1}{\epsilon_0} \sum_s Q_s \sum_{i_s}^{N_s} q^m(L, x_{i_s}) = \frac{1}{\epsilon_0} \sum_s Q_s N_s. \tag{A.27}$$

The spatial averaging of q^m, for uniformly distributed macro-particles, is

$$\langle q^m(x, x_{i_s}) \rangle = \int_0^L \frac{du}{L} q^m(x, u) = \int_0^x dx^{'} \int_0^L \frac{du}{L} S^m(x^{'}, u) = \int_0^x \frac{dx^{'}}{L}(1) = \frac{x}{L}. \tag{A.28}$$

For such macro-particles the average of the electric field is zero:

$$\begin{aligned} \langle E(x) - E_0 \rangle &= \sum_s \left\langle \frac{Q_s}{\epsilon_0} \sum_{i_s}^{N_s} q^m(x, x_{i_s}) \right\rangle \\ &= \sum_s \frac{Q_s}{\epsilon_0} N_s \int_0^L \frac{du}{L} q^m(x, u) \\ &= \sum_s \frac{Q_s}{\epsilon_0} N_s \frac{x}{L} = \frac{x}{\epsilon_0 L} \sum_s Q_s N_s = 0. \end{aligned} \tag{A.29}$$

However, due to the finite number of macro-particles, the average potential energy is

non-zero, to calculate such energy we need to calculate

$$
\begin{aligned}
\left\langle E^2(x) - E_0^2 \right\rangle &= \left\langle (E(x) - E_0)^2 \right\rangle = \left\langle \left(\sum_s \frac{Q_s}{\epsilon_0} \sum_{i_s}^{N_s} q^m(x, x_{i_s}) \right)^2 \right\rangle \\
&= \left\langle \sum_s \left(\frac{Q_s}{\epsilon_0} \sum_{i_s}^{N_s} q^m(x, x_{i_s}) \right)^2 \right\rangle \\
&\quad + \left\langle \sum_{s \neq s'} \left(\frac{Q_s}{\epsilon_0} \sum_{i_s}^{N_s} q^m(x, x_{i_s}) \right) \left(\frac{Q_{s'}}{\epsilon_0} \sum_{i_{s'}}^{N_{s'}} q^m(x, x_{i_{s'}}) \right) \right\rangle \\
&= \frac{1}{\epsilon_0^2} \sum_s \left\langle \left(Q_s \sum_{i_s}^{N_s} q^m(x, x_{i_s}) \right)^2 \right\rangle \\
&\quad + \frac{1}{\epsilon_0^2} \sum_{s \neq s'} \left\langle \left(Q_s \sum_{i_s}^{N_s} q^m(x, x_{i_s}) \right) \right\rangle \left\langle \left(Q_{s'} \sum_{i_{s'}}^{N_{s'}} q^m(x, x_{i_{s'}}) \right) \right\rangle \\
&= \frac{1}{\epsilon_0^2} \sum_s Q_s^2 \left\langle \sum_{i_s}^{N_s} [q^m(x, x_{i_s})]^2 + \sum_{i_s \neq j_s}^{N_s} q^m(x, x_{i_s}) q^m(x, x_{j_s}) \right\rangle \\
&\quad + \frac{1}{\epsilon_0^2} \frac{x^2}{L^2} \sum_{s \neq s'} Q_s N_s Q_{s'} N_{s'} \\
&= \sum_s \frac{Q_s^2}{\epsilon_0^2} \left[N_s \int_0^L \frac{du}{L} [q^m(x, u)]^2 + N_s(N_s - 1) \left[\int_0^L \frac{du}{L} q^m(x, u) \right]^2 \right] \\
&\quad + \frac{1}{\epsilon_0^2} \frac{x^2}{L^2} \sum_{s \neq s'} Q_s N_s Q_{s'} N_{s'} \\
&= \frac{1}{\epsilon_0^2} \frac{x^2}{L^2} \left(\sum_{s \neq s'} Q_s N_s Q_{s'} N_{s'} + \sum_s N_s^2 Q_s^2 \right) + \sum_s \frac{Q_s^2 N_s}{\epsilon_0^2} \left[\int_0^L \frac{du}{L} [q^m(x, u)]^2 - \frac{x^2}{L^2} \right] \\
&= \frac{x^2}{\epsilon_0^2 L^2} \left(\sum_s Q_s N_s \right)^2 + \sum_s \frac{Q_s^2 N_s}{\epsilon_0^2} \left[\int_0^L \frac{du}{L} [q^m(x, u)]^2 - \frac{x^2}{L^2} \right] \\
&= \sum_s \frac{Q_s^2 N_s}{\epsilon_0^2} \left[\int_0^L [q^m(x, u)]^2 \frac{du}{L} - \frac{x^2}{L^2} \right]. \qquad \text{(A.30)}
\end{aligned}
$$

For the shape functions implemented in SHARP-1D (their explicit forms are given in Appendix A.2), the integral in (A.30) is given by

$$\int_0^L \frac{du}{L}[q^m(x,u)]^2 \;=\; \frac{x}{L} - \frac{\Delta x}{L} f_m \qquad \textit{and} \qquad f_m = \frac{1}{6}\begin{cases} 0 & m=0 \\ 1 & m=1 \\ 1.4 & m=2 \\ 1.70714 & m=3 \\ 1.96693 & m=4 \\ 2.19624 & m=5 \end{cases}. \tag{A.31}$$

Therefore,

$$\left\langle E^2(x) - E_0^2 \right\rangle \;=\; \sum_s \frac{N_s Q_s^2}{\epsilon_0^2}\left[\frac{x}{L} - \frac{x^2}{L^2} - \frac{\Delta x}{L} f_m\right]. \tag{A.32}$$

The average electrostatic potential energy due to the finite number of macro-particles is, then, given by

$$\begin{aligned} \mathcal{E}^m \;&=\; \frac{\epsilon_0}{2}\int_0^L dx \left\langle E^2(x) - E_0^2 \right\rangle = \sum_s \frac{N_s Q_s^2}{2\epsilon_0}\left[\frac{L}{6} - \Delta x f_m\right] \\ &=\; \frac{L}{12\epsilon_0}\left[1 - \frac{6 f_m}{N_c}\right]\sum_s N_s Q_s^2 \end{aligned} \tag{A.33}$$

Here, $N_c = L/\Delta x$ is the number of macro-cells. If we assume that all plasma species have the same mass, and absolute value of charge, we then make the choice of our fiducial units as, $q_0^2 = Q_s^2$ and $m_0 = M_s$ (that implies $n_0 = \sum_s n_s$). Therefore,

$$\begin{aligned} \left\langle \bar{\mathcal{E}}^m \right\rangle \;&=\; \frac{\langle \mathcal{E}^m \rangle}{m_0 c^2} = \frac{L^2}{12c^2}\frac{q_0^2 n_0}{\epsilon_0 m_0}\left[1 - \frac{6 f_m}{N_c}\right] \\ &=\; \frac{L^2\omega_0^2}{12c^2}\left[1 - \frac{6 f_m}{N_c}\right] = \frac{\bar{L}^2}{12}\left[1 - \frac{6 f_m}{N_c}\right] \end{aligned} \tag{A.34}$$

Equation (A.34) shows that using higher order shape functions decrease the noise coming from the fact that we are using a finite number of macro-particles. The decrease that we gain in the potential energy noise is $f_m \bar{L}^2/2N_c$. For a given box size, this improvement is lowered, if we increase the number of cells N_c because it means a decreases in cell size which means also a decrease in the size of the macro-particles. On the other hand, if we increase the number of cells while keeping the cell size fixed, i.e., by increasing the box-size $\bar{L}$, that improvement due to using higher order interpolation functions increases.

A.4.2 Spectrum of the Poison noise

To find the spectrum of such noise, we do so by averaging the Fourier transform of the grid electric fields. Using Equation (A.26), the Fourier components of the electric field are given by

$$\begin{aligned}\tilde{E}_n &= \int_0^L \frac{dx}{L}\left[E_0 + \sum_s \frac{Q_s}{\epsilon_0}\sum_{i_s}^{N_s} q^m(x, x_{i_s})\right] e^{-2\pi i n x/L} \\ &= E_0\delta_{n,0} + \sum_s \frac{Q_s}{\epsilon_0}\sum_{i_s}^{N_s}\int_0^L \frac{dx}{L}\left[q^m(x, x_{i_s})\right] e^{-2\pi i n x/L}. \end{aligned} \tag{A.35}$$

By defining

$$Z(x_{i_s}, n) \equiv \int_0^L \frac{dx}{L} q^m(x, x_{i_s}) e^{-2\pi i n x/L} \quad \Rightarrow \quad Z(x_{i_s}, 0) = \frac{x_{i_s}}{L}, \tag{A.36}$$

and using the fact that $E(x)$ is a real valued function, the absolute value for such Fourier components are given by

$$\begin{aligned}|\tilde{E}_n|^2 &= \tilde{E}_n\tilde{E}_{-n} = E_0^2\delta_{n,0} + 2E_0\delta_{n,0}\sum_s \frac{Q_s}{\epsilon_0}\sum_{i_s}^{N_s} Z(x_{i_s}, 0) \\ &\quad + \left[\sum_s \frac{Q_s}{\epsilon_0}\sum_{i_s}^{N_s} Z(x_{i_s}, n)\right]\left[\sum_s \frac{Q_s}{\epsilon_0}\sum_{i_s}^{N_s} Z(x_{i_s}, -n)\right] \\ &= E_0\left[E_0 + 2\sum_s \frac{Q_s}{\epsilon_0}\sum_{i_s}^{N_s}\frac{x_{i_s}}{L}\right]\delta_{n,0} + \sum_s \frac{Q_s^2}{\epsilon_0^2}\left[\sum_{i_s}^{N_s} Z(x_{i_s}, n)\sum_{j_s}^{N_s} Z(x_{j_s}, -n)\right] \\ &\quad + \sum_{s\neq s'}\frac{Q_s Q_{s'}}{\epsilon_0^2}\left[\sum_{i_s}^{N_s} Z(x_{i_s}, n)\sum_{i_{s'}}^{N_{s'}} Z(x_{i_{s'}}, -n)\right] \\ &= E_0\left[E_0 + 2\sum_s \frac{Q_s}{\epsilon_0}\sum_{i_s}^{N_s}\frac{x_{i_s}}{L}\right]\delta_{n,0} + \sum_{s\neq s'}\frac{Q_s Q_{s'}}{\epsilon_0^2}\left[\sum_{i_s}^{N_s} Z^m(x_{i_s}, n)\sum_{i_{s'}}^{N_{s'}} Z^m(x_{i_{s'}}, -n)\right] \\ &\quad + \sum_s \frac{Q_s^2}{\epsilon_0^2}\left[\sum_{i_s}^{N_s} Z^m(x_{i_s}, n)Z^m(x_{i_s}, -n) + \sum_{i_s\neq j_s}^{N_s} Z^m(x_{i_s}, n)Z(x_{j_s}, -n)\right]. \end{aligned} \tag{A.37}$$

Averaging over such periodic box and assuming the macro-particles are uniformly distributed, we can write

$$\begin{aligned}
\langle|\tilde{E}_n|^2\rangle &= E_0\left[E_0+2\sum_s\frac{Q_sN_s}{2\epsilon_0}\right]\delta_{n,0}+\sum_{s\neq s'}\frac{Q_sN_sQ_{s'}N_{s'}}{\epsilon_0^2}\int_0^L\frac{du}{L}Z^m(u,n)\int_0^L\frac{du}{L}Z^m(u,-n)\\
&\quad+\sum_s\frac{Q_s^2}{\epsilon_0^2}\left[N_s\int_0^L\frac{du}{L}\left[Z^m(u,n)Z^m(u,-n)\right]\right.\\
&\quad\left.+(N_s^2-N_s)\int_0^L\frac{du}{L}Z^m(u,n)\int_0^L\frac{du}{L}Z^m(u,-n)\right]\\
&= E_0^2\delta_{n,0}+\left[\sum_{s\neq s'}Q_sN_sQ_{s'}N_{s'}+\sum_sQ_s^2N_s^2\right]\int_0^L\frac{du}{L}Z^m(u,n)\int_0^L\frac{du}{L}Z^m(u,-n)\\
&\quad+\sum_s\frac{Q_s^2N_s}{\epsilon_0^2}\left[\int_0^L\frac{du}{L}\left[Z^m(u,n)Z^m(u,-n)\right]-\int_0^L\frac{du}{L}Z^m(u,n)\int_0^L\frac{du}{L}Z^m(u,-n)\right]\\
&= E_0^2\delta_{n,0}+\sum_s\frac{Q_s^2N_s}{\epsilon_0^2}\left[\int_0^L\frac{du}{L}\left[Z^m(u,n)Z^m(u,-n)\right]-\int_0^L\frac{du}{L}Z^m(u,n)\int_0^L\frac{du}{L}Z^m(u,-n)\right].
\end{aligned}\tag{A.38}$$

By using Equations (A.36, A.28)

$$\begin{aligned}
\int_0^L\frac{du}{L}Z^m(u,n) &= \int_0^L\frac{du}{L}\int_0^L\frac{dx}{L}q^m(x,u)e^{-2\pi inx/L}=\int_0^L\frac{dx}{L}\frac{x}{L}e^{-2\pi inx/L}\\
&= \begin{cases}1/2, & n=0,\\ i/(2\pi n), & n\neq 0,\end{cases}
\end{aligned}\tag{A.39}$$

$$\int_0^L\frac{du}{L}Z^m(u,n)Z^m(u,-n) = \begin{cases}1/3, & n=0,\\ \dfrac{1}{(2\pi n)^2}\left[1+\left(\dfrac{\sin(\pi n/N_c)}{\pi n/N_c}\right)^{2m}\right], & n\neq 0.\end{cases}\tag{A.40}$$

Therefore, the averaged magnitude for the Fourier components can be written as

$$\langle|\tilde{E}_n|^2\rangle = \begin{cases}E_0^2+\sum_s\dfrac{Q_s^2N_s}{12\epsilon_0^2}, & n=0,\\ \sum_s\dfrac{Q_s^2N_s}{(2\pi n)^2\epsilon_0^2}\left[\dfrac{\sin(\pi n/N_c)}{\pi n/N_c}\right]^{2m}, & n\neq 0.\end{cases}\tag{A.41}$$

If all plasma species have the same mass, and absolute value of charges, such average can be written in code units as

$$\langle|\bar{\tilde{E}}_n|^2\rangle = \frac{\langle|\tilde{E}_n|^2\rangle}{\mathbb{E}_0^2} = \begin{cases} \bar{E}_0^2 + \dfrac{\bar{L}^2}{12N_\mathrm{t}}, & n = 0. \\ \dfrac{1}{(2\pi n)^2}\left[\dfrac{\sin(\pi n/N_c)}{\pi n/N_c}\right]^{2m}\dfrac{\bar{L}^2}{N_\mathrm{t}}, & n \neq 0. \end{cases} \tag{A.42}$$

A.4.3 Heating due to noise

If the energy due to Poisson noise is converted to heat that puts a floor in the temperature PIC scheme can simulate. Here we estimate such temperature floor θ_p. The energy due to Poisson noise is calculate in Appendix A.4.1. It is given by

$$\langle\bar{\mathcal{E}}^m\rangle = \frac{\langle\mathcal{E}^m\rangle}{m_0c^2} = \frac{\bar{L}^2}{12}\left[1 - \frac{6f_m}{N_c}\right], \tag{A.43}$$

where f_m is defined in (A.31). This noise is due to the finite number of macro-particles used in the simulations. If this energy is converted to thermal energy, it would lead to heating of the plasma up to a temperature θ_p. If the plasmas are at thermal equilibrium, the momentum distribution is given by Maxwell-Jüttner distribution, and hence the temperature of plasmas is related to the kinetic energy, $\bar{\mathcal{K}}$, as follows

$$\begin{aligned} \langle\bar{\mathcal{K}}\rangle &= \frac{\langle\mathcal{K}\rangle}{m_0c^2} = \sum_s \langle(\gamma-1)\rangle = \sum_s N_s\left[\theta_s + \frac{K_0[1/\theta_s]}{K_1[1/\theta_s]} - 1\right] \\ &= N\left[\theta + \frac{K_0[1/\theta]}{K_1[1/\theta]} - 1\right] = \begin{cases} N\theta/2, & \theta \ll 1, \\ N\theta, & \theta \gg 1. \end{cases} \end{aligned} \tag{A.44}$$

Here, $\theta_s = k_BT_s/m_0c^2$ is the normalized temperature of species s with N_s of macro-particles, N is the total number of macro-particles from all species and K_0, K_1 are the Bessel functions of zeroth and first kind respectively. Therefore,

$$\theta_p = \frac{\bar{L}^2}{12N}\left[1 - \frac{6f_m}{N_c}\right]\begin{cases} 2, & \theta_p \ll 1, \\ 1, & \theta_p \gg 1. \end{cases} \tag{A.45}$$

Hence, if a plasmas of macro-particles starts with temperatures below θ_p the Poisson noise will non-physically heat such plasmas.

A.5 Dispersion relation for non-relativistic warm plasma

For non-relativistic ($\gamma^3 \approx 1$) warm plasma, i.e., $0 < \theta \ll 1$, we can write

$$\begin{aligned} f_0(u)du &= f_0(v)dv = \frac{n_0 d(v/c)}{\sqrt{2\pi\theta}} e^{-(v/c)^2/2\theta} = \frac{n_0 d\bar{v}}{\sqrt{2\pi\theta}} e^{-\bar{v}^2/2\theta} \quad \text{and} \\ \theta &= \frac{k_B T}{mc^2}. \end{aligned} \tag{A.46}$$

If we assume no net current in the plasmas, i.e., the momentum distribution of all species is such that $\sum_s Q_s \int v f_0^s(v) dv = 0$, then the linear dispersion relation of uniformly distributed plasma is given by

$$1 = \sum_s \chi_s(v_p), \tag{A.47}$$

where $v_p = \hat{\omega}/\hat{k}$, $\hat{\omega} = \omega/\omega_p$, $\hat{k} = kc\sqrt{\theta}/\omega_p$, i.e., $v_p = \omega/kc\sqrt{\theta}$, $\omega_p^2 = \sum_s \omega_{ps}^2$, $\omega_{ps}^2 = Q_s^2 n_s/\epsilon_0 M_s$, and $\bar{v} = v/c$.

If we assume that $\Im(\hat{\omega}) > 0$, i.e., $\Im(\omega) > 0$, then

$$\begin{aligned} \chi_s(v_p) &= \frac{Q_s^2}{\epsilon_0 M_s k^2} \int_{-\infty}^{\infty} \frac{f_0(v)dv}{(v-\omega/k)^2} = \frac{\omega_{ps}^2}{k^2c^2} \int_{-\infty}^{\infty} \frac{d\bar{v}}{\sqrt{2\pi\theta}} \frac{e^{-\bar{v}^2/2\theta}}{(\bar{v}-\omega/kc)^2} = \\ &= \frac{\omega_{ps}^2/\omega_p^2}{\hat{\omega}^2} \int_{-\infty}^{\infty} \frac{dz}{\sqrt{2\pi}} \frac{e^{-z^2/2}}{(z-v_p)^2}, \end{aligned} \tag{A.48}$$

where $z \equiv \bar{v}/\sqrt{\theta}$. Extending the definition of $\chi_s(v_p)$ to the entire complex plane can be done as follows (Brambilla, 1998)

$$\chi_s(v_p) = \frac{\hat{\omega}_s^2}{\hat{k}^2} \int_{-\infty}^{\infty} \frac{dz}{\sqrt{2\pi}} \frac{e^{-z^2/2}}{(z-v_p)^2} - \frac{\hat{\omega}_s^2}{\hat{k}^2} \sqrt{\frac{\pi}{2}} v_p \begin{cases} 0 & \text{if } \Im(v_p) > 0 \\ ie^{-v_p^2/2} & \text{if } \Im(v_p) = 0 \\ 2ie^{-v_p^2/2} & \text{if } \Im(v_p) < 0 \end{cases}, \tag{A.49}$$

where $\hat{\omega}_s \equiv \omega_{ps}/\omega_p$. Therefore, for $\Im(v_p) \neq 0$, we can then write

$$
\begin{aligned}
\chi_s(v_p) &= \frac{\hat{\omega}_s^2}{\hat{k}^2}\left[\begin{cases} -1+\sqrt{\frac{\pi}{2}}v_p\left[\mathrm{Erfi}\left(v_p/\sqrt{2}\right)-i\right]e^{-\frac{v_p^2}{2}} & \text{if } \Im(v_p)>0 \\ -1+\sqrt{\frac{\pi}{2}}v_p\left[\mathrm{Erfi}\left(v_p/\sqrt{2}\right)+i\right]e^{-\frac{v_p^2}{2}} & \text{if } \Im(v_p)<0 \end{cases}\right. \\
&\qquad\qquad \left. -\sqrt{\frac{\pi}{2}}v_p\begin{cases} 0 & \text{if } \Im(v_p)>0 \\ 2ie^{-v_p^2/2} & \text{if } \Im(v_p)<0 \end{cases}\right] \\
&= \frac{\hat{\omega}_s^2}{\hat{k}^2}\left[-1+\sqrt{\frac{\pi}{2}}v_p\left[\mathrm{Erfi}\left(v_p/\sqrt{2}\right)-i\right]e^{-\frac{v_p^2}{2}}\right], \qquad \text{(A.50)}
\end{aligned}
$$

where Erfi is the complex error function which is defined as $\mathrm{Erfi}(v_p) = -i\ \mathrm{Erf}(iv_p)$.

A.5.1 Standing linear plasma waves

In the case of thermal electrons with fixed neutralizing background ($\hat{\omega}_s = 1$), the dispersion relation is then given by

$$
\hat{k}^2+1 = \sqrt{\frac{\pi}{2}}v_p\left[\mathrm{Erfi}\left(v_p/\sqrt{2}\right)-i\right]e^{-\frac{v_p^2}{2}} \qquad \text{(A.51)}
$$

A.5.2 Two-stream instability

In the case of two population of thermal electrons (both have the same number density), propagating in two opposite directions with speed v_b, with fixed neutralizing background, therefore $\hat{\omega}_s^2 = 1/2$, and the linear dispersion relation is then given by ($z_b \equiv v_b/c\sqrt{\theta}$)

$$
\begin{aligned}
\hat{k}^2+1 &= \frac{1}{2}\sqrt{\frac{\pi}{2}}(v_p+z_b)\left[\mathrm{Erfi}\left(\frac{v_p+z_b}{\sqrt{2}}\right)-i\right]e^{-\frac{(v_p+z_b)^2}{2}} \\
&\quad +\frac{1}{2}\sqrt{\frac{\pi}{2}}(v_p-z_b)\left[\mathrm{Erfi}\left(\frac{v_p-z_b}{\sqrt{2}}\right)-i\right]e^{-\frac{(v_p-z_b)^2}{2}} \\
&= \sqrt{\frac{\pi}{8}}\left((v_p+z_b)\left[\mathrm{Erfi}\left(\frac{v_p+z_b}{\sqrt{2}}\right)-i\right]e^{-v_pz_b}+\right. \\
&\qquad \left.(v_p-z_b)\left[\mathrm{Erfi}\left(\frac{v_p-z_b}{\sqrt{2}}\right)-i\right]e^{v_pz_b}\right)e^{-(v_p^2+z_b^2)/2}. \qquad \text{(A.52)}
\end{aligned}
$$

Appendix B

Beam-plasma instabilities using fluid description

As we noted in Chapter 3, when the finite temperature effects are included the growth maps are becomes much narrower as compared to the cold-limit growth maps. Here, we show this explicitly using the fluid description of plasmas. We begin by deriving the linearized fluid equations and the dispersion relation for beam-plasma system. We, then, present detailed studies of the dependence of the growth map width (width of unstable oblique modes) on the temperature parameter of both beam and background plasmas at different values of the parameters that characterize the beam-plasma system.

B.1 Relativistic kinetic theory

The correct canonical co-ordinates in the relativistic case are $\{\vec{x}, \vec{u}\}$, where, $\vec{u} = \gamma\vec{v}$. Therefore, the distribution function for particles of species s is $g_s(t, \vec{x}, \vec{u})$ and such distribution function evolves according to Vlasov-equation (V.E.)

$$\partial_t g_s + \frac{u^i}{\gamma}\partial_i g_s + a^i \partial_{u^i} g_s = 0, \quad \text{where,} \quad a^i \equiv \frac{q_s}{m_s} E^i(\vec{x}, t) + \epsilon^{ijk}\frac{u^j}{\gamma} B^k(\vec{x}, t). \tag{B.1}$$

Here, q_s and m_s are the elementary charge and mass of species s, respectively. The self-consistent electric and magnetic fields evolve according to Maxwell's equations

$$\nabla \cdot \vec{E} = \rho/\epsilon_0 \quad \& \quad \nabla \cdot \vec{B} = 0 \quad \& \quad \nabla \times \vec{E} = -\partial_t \vec{B} \quad \& \quad \nabla \times \vec{B} = \mu_0 \vec{J} + \partial_t \vec{E}/c^2, \tag{B.2}$$

with charge and current densities (ρ, $\vec{J}$), the source terms, given by

$$\rho = \sum_s q_s \int g_s \; d^3u \quad \& \quad \vec{J} = \sum_s q_s \int \vec{v} \; g_s \; d^3u. \tag{B.3}$$

The derivation of the fluid equations is done by computing the moments of equation (B.1) and now being concerned with the evolution of these moments in space-time.

B.2 Derivation of fluid equations

Moments of Vlasov-equation

Let's first define the following

$$n_s(\vec{x},t) \equiv \int g_s \; d^3u \tag{B.4}$$

$$n_s(\vec{x},t)\; v_s^i(\vec{x},t) \equiv \int v^i \; g_s \; d^3u \tag{B.5}$$

$$n_s(\vec{x},t)\; u_s^i(\vec{x},t) \equiv \int u^i \; g_s \; d^3u \tag{B.6}$$

$$\begin{aligned} n_s(\vec{x},t)\; P_s^{ji}(\vec{x},t) &\equiv \int \left[u^j - u_s^j\right]\left[v^i - v_s^i\right] \; g_s \; d^3u \\ &= \int \left[u^j v^i - u^j v_s^i - v^i u_s^j + v_s^i u_s^j\right] \; g_s \; d^3u \\ &= \int u^i v^i \; g_s \; d^3u - n_s u_s^j v_s^i - n_s v_s^i u_s^j + n_s v_s^i u_s^j \\ &= \int u^j v^i \; g_s \; d^3u - n_s u_s^j v_s^i \end{aligned} \tag{B.7}$$

$$n_s a_s^j \equiv \int a^j g_s \; d^3u = \frac{q_s}{m_s} n_s \left[E^j + \epsilon^{jkl} v_s^k B^l\right] \tag{B.8}$$

Zeroth moment: $\int (\text{V.E.}) d^3u = 0$, Therefore,

$$0 = \partial_t \int g_s d^3u + \partial_i \int v^i g_s d^3u = \partial_t n_s + \partial_i \left[n_s v_s^i\right] \tag{B.9}$$

$$\partial_t n_s + (\vec{v}_s \cdot \nabla) n_s + n_s \nabla \cdot \vec{v}_s = 0 \tag{B.10}$$

First moment: $\int u^j (\text{V.E.}) d^3u = 0$, Therefore,

$$\begin{aligned} 0 &= \partial_t \int u^j g_s d^3u + \partial_i \int u^j v^i g_s d^3u + \int u^j \partial_{u^i}(a^i g_s) d^3u \\ &= \partial_t \left[n_s u_s^j \right] + \partial_i \left[n_s P^{ji} + n_s u_s^j v_s^i \right] - \int a^j g_s d^3u \\ &= n_s \partial_t u_s^j + \partial_i \left[n_s P_s^{ji} \right] + n_s v_s^i \partial_i \left[u_s^j \right] - n_s a_s^j \end{aligned} \tag{B.11}$$

$$\partial_t u_s^j + (\vec{v}_s \cdot \nabla) u_s^j + \partial_i \left[n_s P_s^{ji} \right] = \frac{q_s}{m_s} \left[\vec{E} + \vec{v}_s \times \vec{B} \right]^j \tag{B.12}$$

To summarize, the fluid-evolution equations are, *for each species* s, given by

$$\partial_t n_s + \nabla \cdot [n_s \vec{v}_s] = 0 \tag{B.13}$$

$$\partial_t u_s^j + (\vec{v}_s \cdot \nabla) u_s^j + \partial_i \left[n_s P_s^{ji} \right] = \frac{q_s}{m_s} \left[\vec{E} + \vec{v}_s \times \vec{B} \right]^j \tag{B.14}$$

Fields evolution is given by:

$$\nabla \cdot \vec{E} = \rho/\epsilon_0 \qquad \& \qquad \nabla \cdot \vec{B} = 0 \tag{B.15}$$

$$\nabla \times \vec{E} = -\partial_t \vec{B} \qquad \& \qquad \nabla \times \vec{B} = \mu_0 \vec{J} + \partial_t \vec{E}/c^2 \tag{B.16}$$

$$\rho = \sum_s q_s n_s \qquad \& \quad \vec{J} = \sum_s q_s n_s \vec{v}_s \tag{B.17}$$

B.3 Linear dispersion relation from fluid equations

Linearization for the evolution equations

To find the dispersion tensor, we need first to linearize the equations, and then take the Fourier transforms for the linear terms.

Linearized Maxwell-equations

Using the following expansions

$$\vec{E} = \vec{E}_0 + \vec{E}_1 \quad \& \quad \vec{B} = \vec{B}_0 + \vec{B}_1 \quad \& \quad \vec{J} = \vec{J}_0 + \vec{J}_1 \quad \& \quad \rho = \rho_0 + \rho_1 \quad \& \quad |E_1/E_0| \ll 0 \ \forall \vec{x}, t \cdots \text{ etc}$$

The linearlized equation are given by

Zeroth order

$$\nabla \cdot \vec{E}_0 = \rho_0/\epsilon_0 \qquad \& \qquad \nabla \cdot \vec{B}_0 = 0 \tag{B.18}$$
$$\nabla \times \vec{E}_0 = -\partial_t \vec{B}_0 \qquad \& \qquad \nabla \times \vec{B}_0 = \mu_0 \vec{J}_0 + \partial_t \vec{E}_0/c^2 \tag{B.19}$$
$$\rho_0 = \sum_s q_s n_{s,0} \qquad \& \quad \vec{J}_0 = \sum_s q_s n_{s,0} \vec{v}_{s,0} \tag{B.20}$$

First order

$$\nabla \cdot \vec{E}_1 = \rho_1/\epsilon_0 \qquad \& \qquad \nabla \cdot \vec{B}_1 = 0 \tag{B.21}$$
$$\nabla \times \vec{E}_1 = -\partial_t \vec{B}_1 \qquad \& \qquad \nabla \times \vec{B}_1 = \mu_0 \vec{J}_1 + \partial_t \vec{E}_1/c^2 \tag{B.22}$$
$$\rho_1 = \sum_s q_s n_{s,1} \qquad \& \quad \vec{J}_1 = \sum_s q_s \left[n_{s,1} \vec{v}_{s,0} + n_{s,0} \vec{v}_{s,1} \right] \tag{B.23}$$

First order: Fourier transform

For simplicity, we drop ˜ on the first order quantities, which indicates that the quantities are function of $(\vec{k}, \omega)$. Therefore,

$$i\vec{k} \cdot \vec{E}_1 = \rho_1/\epsilon_0 \qquad \& \qquad \vec{k} \cdot \vec{B}_1 = 0 \tag{B.24}$$
$$\vec{k} \times \vec{E}_1 = \omega \vec{B}_1 \qquad \& \qquad i\vec{k} \times \vec{B}_1 = \mu_0 \vec{J}_1 - i\omega \vec{E}_1/c^2 \tag{B.25}$$
$$\rho_1 = \sum_s q_s n_{s,1} \qquad \& \quad \vec{J}_1 = \sum_s q_s \left[n_{s,1} \vec{v}_{s,0} + n_{s,0} \vec{v}_{s,1} \right] \tag{B.26}$$

Therefore,

$$\vec{k} \cdot \vec{J}_1 = \omega \rho_1 \quad \& \quad i\vec{k} \times \left(\vec{k} \times \vec{B}_1 \right) = -ik^2 \vec{B}_1 = \mu_0 \vec{k} \times \vec{J} - i\omega^2 \vec{B}_1/c^2 \quad \Rightarrow \quad \boxed{\vec{B}_1 = i \frac{\mu_0 \vec{k} \times \vec{J}_1}{k^2 - \omega^2/c^2}}$$

$$i\vec{k} \times \vec{B}_1 = \frac{i\vec{k}}{\omega} \times \vec{k} \times \vec{E}_1 = \frac{i\vec{k}}{\omega} \vec{k} \cdot \vec{E}_1 - \frac{ik^2}{\omega} \vec{E}_1 = \mu_0 \vec{J}_1 - \frac{i\omega}{c^2} \vec{E}_1 \quad \Rightarrow \quad \boxed{\vec{J}_1 = \frac{i\omega}{\mu_0 c^2} \left[1 - \frac{k^2 c^2}{\omega^2} \right] \vec{E}_1 + \frac{i\vec{k}}{\mu_0 \omega} \vec{k} \cdot \vec{E}_1}$$

If we define $\vec{q} \equiv \vec{k}c/\omega$, we can write

$$\vec{J}_1 = \frac{i\omega}{\mu_0 c^2} \left[1 - q^2 \right] \vec{E}_1 + \frac{i\omega}{\mu_0 c^2} \vec{q}\vec{q} \cdot \vec{E}_1 \quad \Rightarrow \quad \boxed{J_1^i = i\epsilon_0 \omega \left[(1 - q^2)\delta^{ij} + q^i q^j \right] E_1^j}$$

Linearized equations for uniform fluid at equilibrium

Using the following expansions

$$\begin{aligned} n_s = n_{s,0} + n_{s,1} \qquad \& \qquad \vec{v}_s = \vec{v}_{s,0} + \vec{v}_{s,1} \qquad \& \qquad \vec{u}_s = \vec{u}_{s,0} + \vec{u}_{s,1} \\ P_s^{ji} = P_{s,0}^{ji} + P_{s,1}^{ji} \qquad \& \qquad |n_{s,1}/n_{s,0}| \ll 0 \ \forall \vec{x}, t \cdots \text{ etc} \end{aligned} \tag{B.27}$$

Therefore, the linearized equations are given by

Zeroth order

$$\partial_t n_{s,0} + \nabla \cdot [n_{s,0}\, \vec{v}_{s,0}] = 0 \tag{B.28}$$

$$\partial_t u_{s,0}^j + (\vec{v}_{s,0} \cdot \nabla) u_{s,0}^j + \partial_i \left[n_{s,0} P_{s,0}^{ji} \right] = \frac{q_s}{m_s} \left[\vec{E}_0 + \vec{v}_{s,0} \times \vec{B}_0 \right]^j \tag{B.29}$$

First order

$$\partial_t n_{s,1} + \nabla \cdot [n_{s,1}\, \vec{v}_{s,0} + n_{s,0}\, \vec{v}_{s,1}] = 0 \tag{B.30}$$

$$\partial_t u_{s,1}^j + (\vec{v}_{s,0} \cdot \nabla) u_{s,1}^j + (\vec{v}_{s,1} \cdot \nabla) u_{s,0}^j + \partial_i \left[n_{s,1} P_{s,0}^{ji} + n_{s,0} P_{s,1}^{ji} \right] = \frac{q_s}{m_s} \left[\vec{E}_1 + \vec{v}_{s,1} \times \vec{B}_0 + \vec{v}_{s,0} \times \vec{B}_1 \right]^j \tag{B.31}$$

In the case of uniform fluid at equilibrium and with no external electric field, for all species s, we have

$$n_{s,0}(\vec{x}, t) = n_{s,0}, \quad \vec{v}_{s,0}(\vec{x}, t) = \vec{v}_{s,0}, \quad \vec{u}_{s,0}(\vec{x}, t) = \vec{u}_{s,0}, \quad P_{s,0}^{ji}(\vec{x}, t) = P_{s,0}^{ji}, \quad E_0(\vec{x}, t) = 0. \tag{B.32}$$

Therefore, the linearized equations are given by

Zeroth order

$$0 = \frac{q_s}{m_s} \left[\vec{v}_{s,0} \times \vec{B}_0 \right] \tag{B.33}$$

Therefore, if external magnetic field $\vec{B}_0 \neq 0$, then it has to be parallel to $\vec{v}_{s,0}$ for all species.

First order (Here, we assume that $P_{s,1}^{ji} = 0$)

$$\partial_t n_{s,1} + \vec{v}_{s,0} \cdot \nabla n_{s,1} + n_{s,0} \nabla \cdot \vec{v}_{s,1} = 0 \tag{B.34}$$

$$\left[\partial_t + \vec{v}_{s,0} \cdot \nabla \right] \vec{u}_{s,1} + P_{s,0}^{ji}\, \partial_i n_{s,1} = \frac{q_s}{m_s} \left[\vec{E}_1 + \vec{v}_{s,1} \times \vec{B}_0 + \vec{v}_{s,0} \times \vec{B}_1 \right] \tag{B.35}$$

First order: Fourier transform

For simplicity, we drop ˜ on the first order quantities, which indicates that the quantities are function of $(\vec{k}, \omega)$. Therefore,

$$-i\left[\omega - \vec{k}\cdot\vec{v}_{s,0}\right] n_{s,1} + i\vec{k}\cdot\vec{v}_{s,1} n_{s,0} = 0 \quad \Rightarrow \quad \boxed{n_{s,1} = n_{s,0}\frac{k^m v^m_{s,1}}{\omega - \vec{k}\cdot\vec{v}_{s,0}}} \tag{B.36}$$

$$-i\left[\omega - \vec{k}\cdot\vec{v}_{s,0}\right] u^j_{s,1} + ik_i P^{ji}_{s,0} n_{s,1} = \frac{q_s}{m_s}\left[\vec{E}_1 + \vec{v}_{s,1}\times\vec{B}_0 + \vec{v}_{s,0}\times\vec{B}_1\right]^j \tag{B.37}$$

To solve for $v_{s,1}$ using Equation (B.37), $\vec{u}_{s,1}$ need to be expressed in terms of $\vec{v}_{s,0}$ and $\vec{v}_{s,1}$. This can be done by substituting $v^i = v^i_{s,0} + \delta v^i$ in $u^i = v^i/\sqrt{1 - v^j v^j/c^2}$, and using this in Equation (B.6), and the definition of v_s in Equation (B.5), to the first order in δv^i, we get

$$\vec{u}_{s,1} = \gamma_{s,0}\vec{v}_{s,1} + \gamma^3_{s,0}(\vec{v}_{s,0}\cdot\vec{v}_{s,1}/c^2)\vec{v}_{s,0}, \quad \text{or} \quad u^j_{s,1} = \gamma_{s,0}\left[\delta^{jm} + \gamma^2_{s,0} v^m_{s,0} v^j_{s,0}/c^2\right] v^m_{s,1}. \tag{B.38}$$

This approximation is predicated upon the assumption that the velocity spread (the plasma temperature) for all species is non-relativistic.

Therefore, using $\omega\vec{B}_1 = \vec{k}\times\vec{E}_1$, we have

$$\frac{q_s}{m_s}\left[\vec{E}_1 + \frac{\vec{v}_{s,0}\times\vec{k}\times\vec{E}_1}{\omega}\right]^j = \left\{-i\gamma_{s,0}(\omega - \vec{k}\cdot\vec{v}_{s,0})\left[\delta^{jm} + \gamma^2_{s,0} v^m_{s,0} v^j_{s,0}/c^2\right] + i\frac{k^i k^m n_{s,0}}{\omega - \vec{k}\cdot\vec{v}_{s,0}} P^{ji}_{s,0} - \frac{q_s}{m_s}\epsilon^{jml} B^l_0\right\} v^m_{s,1} \tag{B.39}$$

Since,

$$\begin{aligned}
\left(\vec{v}_{s,0}\times\vec{k}\times\vec{E}_1\right)^j &= \epsilon^{jml} v^m_{s,0}(\vec{k}\times\vec{E}_1)^l = \epsilon^{ljm}\epsilon^{lab} v^m_{s,0} k^a E^b_1 \\
&= \left[\delta^{ja}\delta^{mb} - \delta^{jb}\delta^{ma}\right] v^m_{s,0} k^a E^b_1 = \left[k^j v^b_{s,0} - \vec{k}\cdot\vec{v}_{s,0}\,\delta^{jb}\right] E^b_1 \\
\Rightarrow \quad \left(\vec{v}_{s,0}\times\vec{k}\times\vec{E}_1\right)^j &= \left[k^j v^b_{s,0} - (\vec{k}\cdot\vec{v}_{s,0})\delta^{jb}\right] E^b_1
\end{aligned} \tag{B.40}$$

Therefore,

$$\frac{q_s}{m_s\ \omega}\left\{(\omega-\vec{k}\cdot\vec{v}_{s,0})\ \delta^{jb}+k^j v^b_{s,0}\right\}E^b_1 =$$
$$\left\{-i\gamma_{s,0}(\omega-\vec{k}\cdot\vec{v}_{s,0})\left[\delta^{jm}+\gamma^2_{s,0}v^m_{s,0}v^j_{s,0}/c^2\right]+i\frac{P^{ji}_{s,0}k^ik^mn_{s,0}}{\omega-\vec{k}\cdot\vec{v}_{s,0}}-\frac{q_s\ \ \epsilon^{jml}B^l_0}{m_s}\right\}v^m_{s,1} \tag{B.41}$$

Equation (B.41) can be solved for $\vec{v}_{s,1}$ in terms of $\vec{E}_1$.

Now we use the definition of the current to find $\vec{J}_1$ in terms of $\vec{v}_{s,1}$: using the equation for $n_{s,1}$ we can write the current for species s as

$$\vec{J}_{s,1}=q_sn_{s,0}\vec{v}_{s,1}+q_sn_{s,1}\vec{v}_{s,0}=q_sn_{s,0}\left[\vec{v}_{s,1}+\frac{\vec{k}\cdot\vec{v}_{s,1}}{\omega-\vec{k}\cdot\vec{v}_{s,0}}\vec{v}_{s,0}\right]$$
$$\text{Therefore,}\qquad J^i_{s,1}=q_sn_{s,0}\left[\delta^{im}+\frac{k^mv^i_{s,0}}{\omega-\vec{k}\cdot\vec{v}_{s,0}}\right]v^m_{s,1} \tag{B.42}$$

We define the following 3×3 matrices

$$A_s=\{A^{jm}_s\}\ \equiv\ \left\{-i\gamma_{s,0}(\omega-\vec{k}\cdot\vec{v}_{s,0})\left[\delta^{jm}+\gamma^2_{s,0}v^m_{s,0}v^j_{s,0}/c^2\right]+i\frac{P^{ji}_{s,0}k^ik^mn_{s,0}}{\omega-\vec{k}\cdot\vec{v}_{s,0}}-\frac{q_s\ \ \epsilon^{jml}B^l_0}{m_s}\right\} \tag{B.43}$$

$$B_s=\{B^{jb}_s\}\ \equiv\ \frac{q_s}{m_s}\left\{\left(1-\frac{\vec{k}\cdot\vec{v}_{s,0}}{\omega}\right)\delta^{jb}+\frac{k^jv^b_{s,0}}{\omega}\right\} \tag{B.44}$$

$$C_s=\{C^{im}_s\}\ \equiv\ q_sn_{s,0}\left\{\delta^{im}+\frac{k^mv^i_{s,0}}{\omega-\vec{k}\cdot\vec{v}_{s,0}}\right\} \tag{B.45}$$

$$F=\{F^{ij}\}\ \equiv\ i\epsilon_0\omega\left\{(1-q^2)\delta^{ij}+q^iq^j\right\} \tag{B.46}$$

Here, $\vec{q}\equiv\vec{k}c/\omega$. In terms of the above matrices, our first order equations become

$$A_s\cdot\vec{v}_{s,1}=B_s\cdot\vec{E}_1\quad\&\quad\vec{J}_{s,1}=C_s\cdot\vec{v}_{s,1}\quad\Rightarrow\quad\vec{J}_1=F\cdot\vec{E}_1=\sum_s C_s\cdot A_s^{-1}\cdot B_s\cdot\vec{E}_1 \tag{B.47}$$

Therefore,

$$\left[F-\sum_s C_s\cdot A_s^{-1}\cdot B_s\right]\cdot\vec{E}_1=0$$

And we get the dispersion relation from the determinant as follow

$$\left| F - \sum_s C_s \cdot A_s^{-1} \cdot B_s \right| = 0 \tag{B.48}$$

To get this dispersion relation two approximations were assumed on top of the relativistic kinetic theory. First, we assumed that $P_{s,1}^{i,j} = 0$, i.e., we ignored the perturbative evolution of the thermal dispersion of different species. Second, we approximated $u_{s,1}^{j}$ using $u_{s,1}^{j} = \gamma_{s,0} \left[\delta^{jm} + \gamma_{s,0}^2 v_{s,0}^m v_{s,0}^j / c^2 \right] v_{s,1}^m$, this second approximation is valid in the case of non-relativistic velocity dispersion for each species around $\vec{v}_{s,0}$.

B.4 Application to beam-plasma system

For beam-plasma system, there are 4 species: background ions and electrons, ($s = 0$, 1, respectively), and beam electrons and positrons ($s = 2$, 3, respectively). Here, we will assume that the background ions are infinitely massive, i.e., fixed neutralizing background, therefore, the background ions will not contribute to the plasma frequency and also that there is external magnetic field, i.e., $\vec{B}_0 = 0$.

Therefore, we have

- *Background electrons*: $s = 1$, $n_{s,0} = n_g$, $q_s = -e$ and $m_s = m_e$.
- *Beam electrons*: $s = 2$, $n_{s,0} = n_b = (\alpha/2) n_g$, $q_s = -e$ and $m_s = m_e$.
- *Beam positrons*: $s = 3$, $n_{s,0} = n_b = (\alpha/2) n_g$, $q_s = +e$ and $m_s = m_e$.

Here, α is the ratio of the number density of all dynamical beam particles (electrons and positrons) to the number density of all dynamical background particles (only electrons), i.e., $\alpha = 2n_b/n_g$.

To simplify the computation here, we can assume without loss of generality that the beam particles are initially moving with respect to the background plasmas in the x-direction of the background frame. Therefore we can write

$$\vec{k} = \{k_x, k_y, 0\} \quad \& \quad \vec{v}_{s,0} = \{0, 0, 0\}, \qquad s = 1 \quad \& \quad \vec{v}_{s,0} = \{v_b, 0, 0\}, \qquad s = 2, 3$$

B.4.1 Effect of background temperature

Here we consider the effect of the background temperature when the beam particles are monochromatic, i.e., have a zero equilibrium temperature in the background plasma frame. Therefore, for the beam particles, using $P^{ji}_{s,0} = 0, \quad s = 2, 3$, we can write

$$C_s \cdot A_s^{-1} \cdot B_s = \frac{2n_b q_s^2/m_e}{i\gamma_b \omega(\omega - k_x v_b)^2} \begin{pmatrix} \left(\omega^2 - k_y^2 c^2\right) v_b^2/c^2 - \omega^2 & k_y v_b \left(k_x v_b - \omega\right) & 0 \\ k_y v_b \left(k_x v_b - \omega\right) & -\left(\omega - k_x v_b\right)^2 & 0 \\ 0 & 0 & -\left(\omega - k_x v_b\right)^2 \end{pmatrix}. \tag{B.49}$$

For the background electrons, if we assume non-relativistic temperature, the perfect gas hypothesis can be used for the background to relate the background pressure term to its temperature since, in the background frame, the mean-velocity of the background plasma $v_g(\vec{x}, t)$ is non-relativistic (Bret & Deutsch, 2006). Assuming that the background temperature, T_g, is the same in all directions, i.e.,

$$n_g k^i P^{ji}_{s=1,0} = 3v_{th}^2 \{k_x, k_y, 0\} = 3\theta_g c^2 \{k_x, k_y, 0\},$$

where, $\theta_g = k_B T_g / m_e c^2 = v_{th}^2/c^2$, where, k_B is the Boltzmann constant.

Therefore, for the background electrons

$$C_s \cdot A_s^{-1} \cdot B_s = \frac{i n_g q_s^2/m_e}{\omega\left(\omega^2 - 3k^2 c^2 \theta_g\right)} \begin{pmatrix} \omega^2 - 3k_y^2 c^2 \theta_g & 3k_x k_y c^2 \theta_g & 0 \\ 3k_x k_y c^2 \theta_g & \omega^2 - 3k_x^2 c^2 \theta_g & 0 \\ 0 & 0 & \omega^2 - 3k^2 c^2 \theta_g \end{pmatrix}, \tag{B.50}$$

where, $k^2 = k_x^2 + k_y^2$.

We, then, use Equations (B.49, B.50) to compute the dispersion matrix

$$F - \sum_s C_s \cdot A_s^{-1} \cdot B_s.$$

The determinant of which implies the following the dispersion relation

$$0 = \left(\hat{\omega} - \hat{k}\hat{v}_b\right) \left[\hat{\omega}^2 - \hat{k}^2 - 1 - \alpha/\gamma_b\right] \left[A_1 + 3A_2\theta_g\right], \tag{B.51}$$

where, $\hat{k} = kc/\omega_g$, $\hat{k}_x = k_x c/\omega_g$, $\hat{k}_y = k_y c/\omega_g$, $\hat{\omega} = \omega/\omega_g$, $\hat{v}_b = v_b/c$, and the temperature

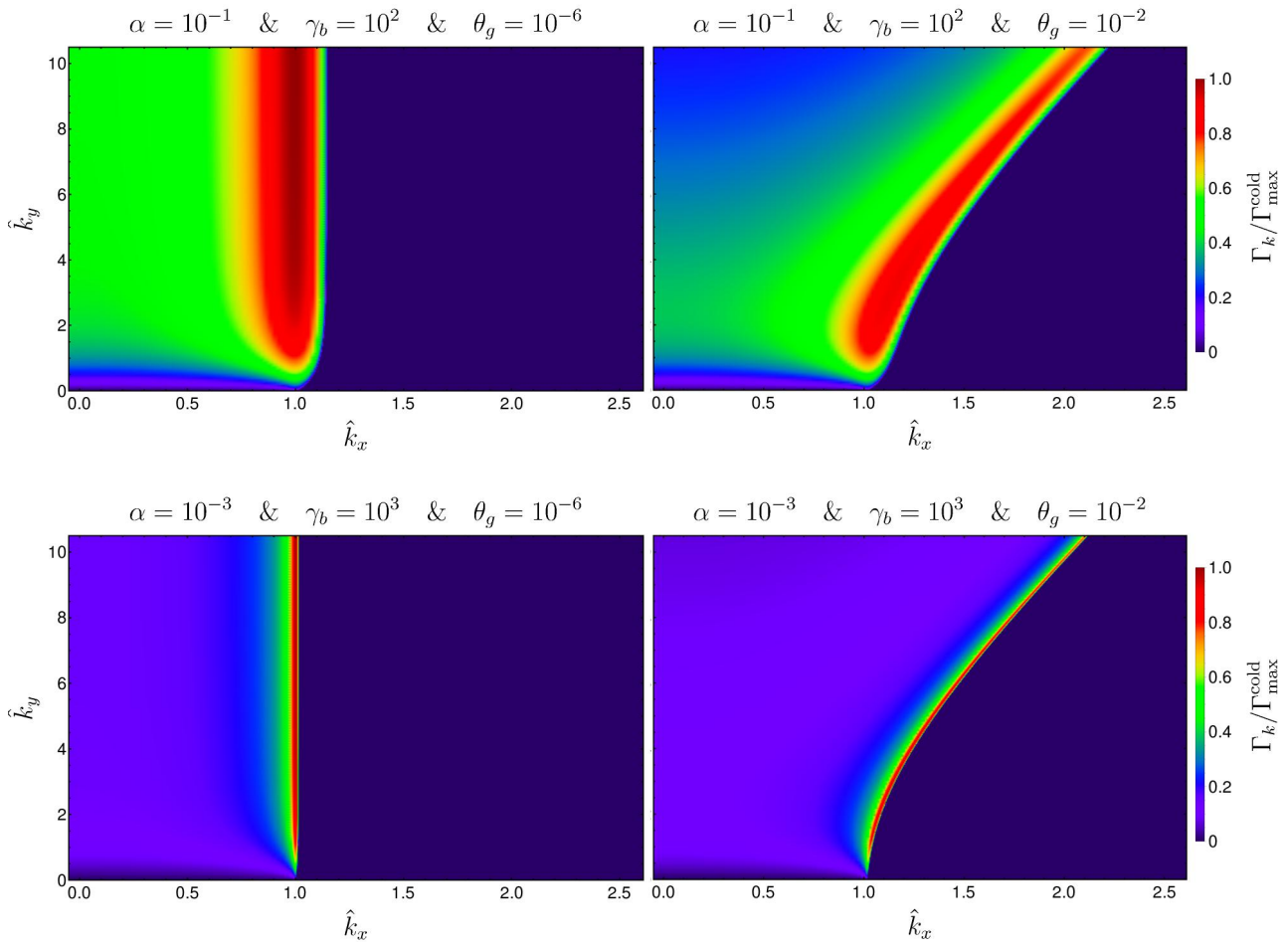

Figure B.1 The growth rate maps normalized to the maximum growth rate in the cold-limit $\Gamma_{\max}^{\rm cold} \approx \sqrt{3}\,(\alpha/\gamma_b)^{1/3}\,/2^{4/3}$.

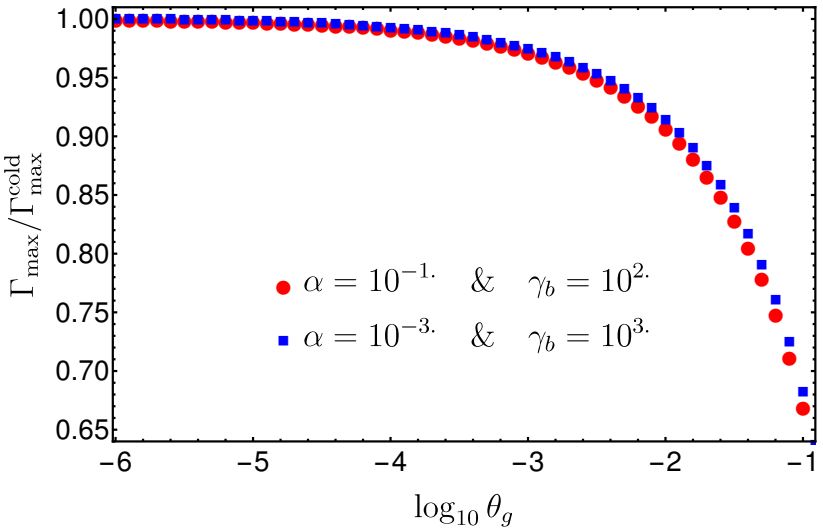

Figure B.2 The dependence of the maximum growth rate (normalized to the maximum growth rate of the cold-limit, i.e., $\theta_g = 0$) on the background temperature, θ_g, for mono-energetic beams.

independent coefficients A_1 and A_2 are given by

$$\begin{aligned} A_1 &= \alpha^2\hat{\omega}^2 + \gamma_b^4\left(\hat{\omega}^2-1\right)\left(-\hat{k}^2+\hat{\omega}^2-1\right)\left(\hat{\omega}-\hat{k}_x\hat{v}_b\right)^2 + \alpha\gamma_b\left(\left(\hat{k}^2+1\right)\hat{\omega}^2-\hat{k}_y^2-\hat{\omega}^4\right) \\ &\quad +\alpha\gamma_b^3\left(\hat{k}_y^2-\left(\hat{\omega}^2-1\right)\left(\hat{\omega}-\hat{k}_x\hat{v}_b\right)^2\right), \qquad \text{(B.52)} \\ A_2 &= \hat{k}^4\gamma_b^4\hat{v}_b\hat{k}_x(\hat{v}_b\hat{k}_x-2\hat{\omega}) - \alpha\gamma_b\left(\hat{k}_y^2(\gamma_b^2-\hat{k}_y^2-1)+\hat{k}_x^4+\hat{k}^2(2\hat{k}_y^2+1)\right) + \\ &\quad \hat{k}^2\left[\alpha\gamma_b^3\left(\hat{\omega}-\hat{v}_b\hat{k}_x\right)^2+\gamma_b^4\left(2\hat{\omega}^3\hat{v}_b\hat{k}_x-2\hat{\omega}\hat{v}_b\hat{k}_x+\hat{v}_b^2\hat{k}_x^2+\hat{\omega}^2(\hat{k}_y^2+1)-\hat{\omega}^4\right)\right. \\ &\quad \left.+\hat{\omega}^2\gamma_b^2\hat{k}_x^2-\alpha^2+\alpha\hat{\omega}^2\gamma_b\right]. \qquad \text{(B.53)} \end{aligned}$$

This dispersion relation agrees with the one found using the Mathematica notebook provided in Bret (2007) for the same setup considered here.

The roots of the first two parts of Equation (B.51) gives only real solutions for $\hat{\omega}$, with the stable electromagnetic modes comes from the root of the second part. The roots for the second part admits imaginary solutions for $\hat{\omega}$, which gives the growth rates of the unstable wave modes.

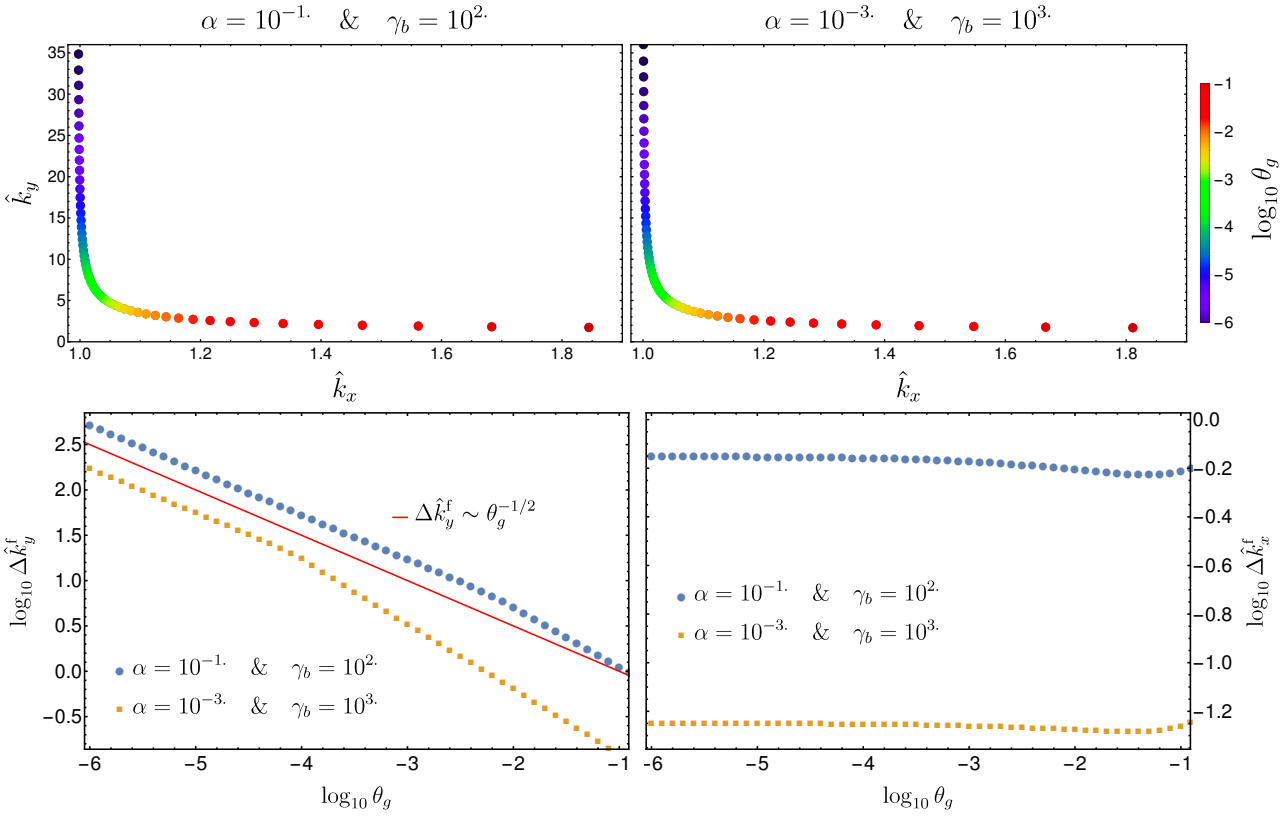

Figure B.3 For mono-energetic beams, the dependence of the position of the maximally growing wave-mode on the background temperature, θ_g is shown in the top panels. Bottom panels show the change in the full width half max of the unstable region around the fastest growing wave mode in both parallel and perpendicular directions with respect to the beam.

The dispersion relation, $A_1 + 3A_2\theta_g = 0$, is a polynomial of degree 8 and thus it does not have a general analytical solution. The growth rates maps shown in Figure B.1 are found by numerically solving the dispersion relation and finding the growth rate (solution of ω with the largest imaginary part) at different values of k_x and k_y.

As see in Figure B.1, the maximum growth rate slightly changes when the background temperature increases, but the width of the unstable regime in the perpendicular direction and the wave mode at which the maximum growth rate is located changes appreciably. The dependence of the maximum growth rate (normalized to the maximum growth rate of the cold-limit, i.e., $\theta_g = 0$) on the background temperature θ_g is shown in Figure B.2 for $\alpha = 10^{-1}$ and $\gamma_b = 10^2$ (red points) and $\alpha = 10^{-3}$ and $\gamma_b = 10^3$ (blue points).

In Figure B.3, the dependence of the position of the maximally growing wave-mode on the background temperature θ_g is shown in top panels for $\alpha = 10^{-1}$ and $\gamma_b = 10^2$ (Left) and $\alpha = 10^{-3}$ and $\gamma_b = 10^3$ (Right), while the full width half max of the unstable region is shown in bottom panels for both parallel and perpendicular directions with respect to the beam. The width unstable region in the direction parallel to the beam is independent of the background temperature, while the width in the perpendicular direction drops as $\theta_g^{-1/2}$, i.e., the background temperature stabilize the perpendicular large k (short wavelength) unstable wave modes.

B.4.2 Effect of beam temperature

To include a temperature parameter for the beam plasmas, we include non-vanishing anisotropic pressure tensor: we used

$$n_b k^i P^{ji}_{s,0} = 3\{k_x (v^{\parallel}_{th,b})^2, k_y (v^{\perp}_{th,b})^2, 0\} = 3c^2\{k_x\theta_{b,\parallel}, k_y\theta_{b,\perp}, 0\}, \qquad s = 2, 3.$$

Following the same procedure outlined in Section B.4.1, the resulting part of the dispersion relation, that has the unstable modes, is given by

$$0 \;=\; (\hat{\omega} - \hat{v}_b\hat{k}_x)\left[A_1 + 3\;A_2\theta_g\right] + 3[\hat{\omega}^2 - 3\;\theta_g\hat{k}^2 - 1]\left[A_{3,\perp}\theta_{b,\perp} + A_{3,\parallel}\theta_{b,\parallel}\right], \quad \text{(B.54)}$$

where A_1 and A_2 are given in Equations (B.52, B.53), and

$$A_{3,\parallel} \;=\; \hat{k}_x\left(\alpha\left(\hat{\omega}\hat{k}_x - \hat{k}^2\hat{v}_b\right) + \gamma_b\hat{k}_x\left(\hat{\omega}^2 - \hat{k}^2 - 1\right)\left(\hat{v}_b\hat{k}_x - \hat{\omega}\right)\right) \quad \text{(B.55)}$$

$$A_{3,\perp} \;=\; \hat{k}_y^2\left(\alpha\hat{\omega} - \gamma_b^3\left(\hat{\omega}^2 - \hat{k}^2 - 1\right)\left(\hat{\omega} - \hat{v}_b\hat{k}_x\right)\right) \quad \text{(B.56)}$$

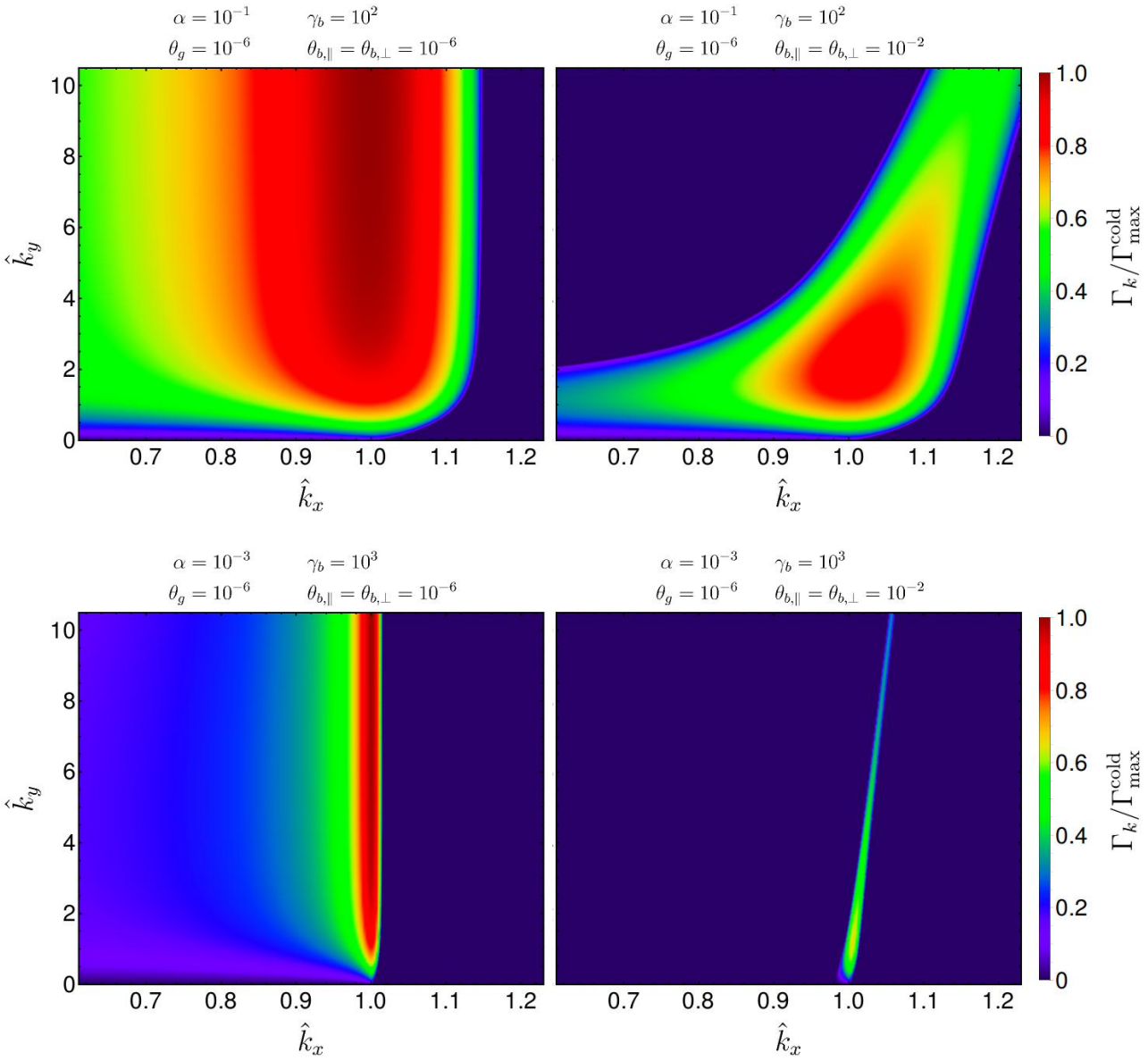

Figure B.4 The effect of beam temperature on the growth maps for low temperature background plasma, $\theta_g = 10^{-6}$. The growth rates are normalized to the maximum growth rate in the cold-limit $\Gamma_{\rm max}^{\rm cold} \approx \sqrt{3}\,(\alpha/\gamma_b)^{1/3}\,/2^{4/3}$.

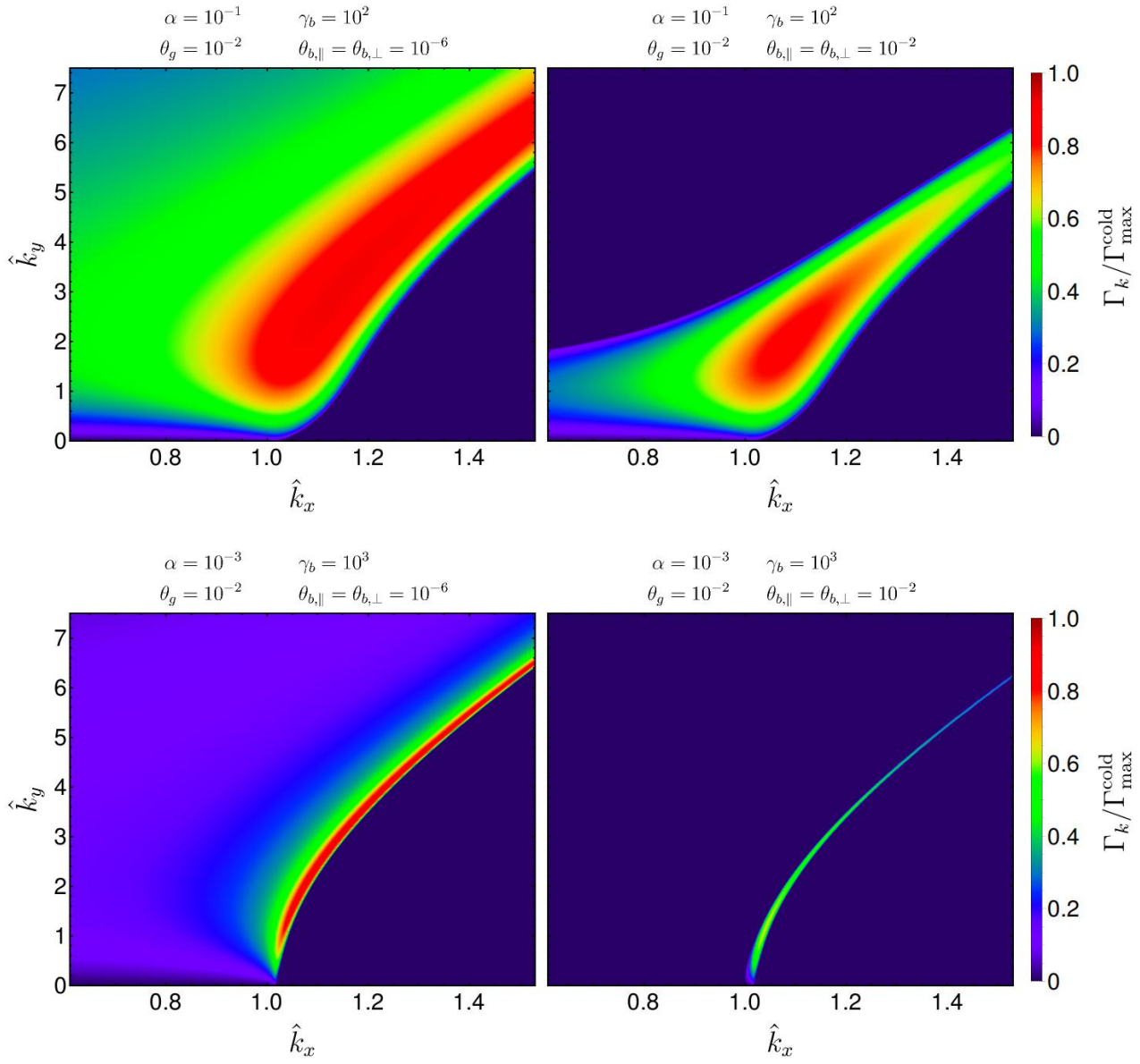

Figure B.5 The effect of beam temperature on the growth maps for hot background plasma, $\theta_g = 10^{-2}$. The growth rates are normalized to the maximum growth rate in the cold-limit $\Gamma_{\max}^{\rm cold} \approx \sqrt{3}\,(\alpha/\gamma_b)^{1/3}/2^{4/3}$.

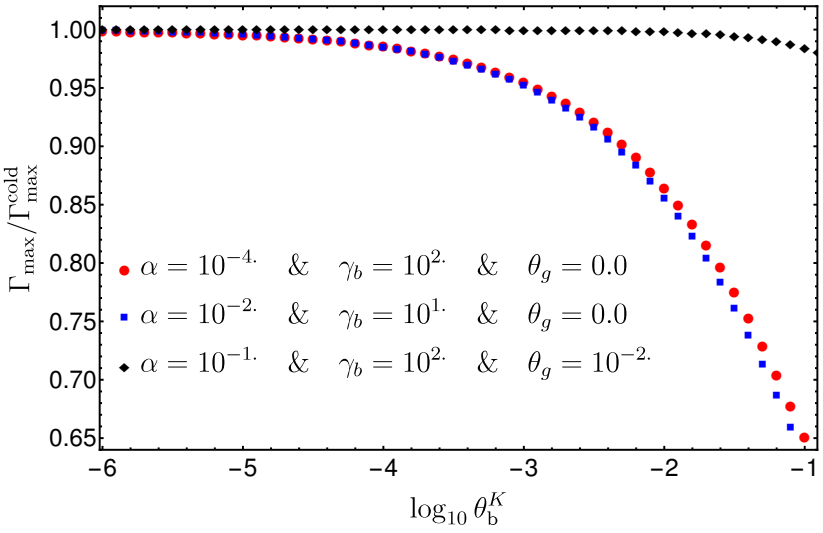

Figure B.6 The maximum growth rate (normalized to the maximum growth rate of the monochromatic beam case, i.e., $\theta_b^K = 0$) for different beam and background temperatures. The beam temperature parameters are scaled differently in the parallel and perpendicular directions (with respect to the beam direction), i.e., $\theta_{b,\parallel} = \theta_b^K/\gamma_b^3$, and $\theta_{b,\perp} = \theta_b^K/\gamma_b$.

We can see directly from the dispersion relation in Equation (B.54) that for low background temperatures $\theta_g \ll 1$, the effect of beam temperature is independent of θ_g, while in the opposite limit, the background temperature could influence the effect of the beam temperature parameters. Therefore, we will use the solution of Equation (B.54) to study the effect of the background temperature when the background temperature parameter is both zero a non-zero.

In Figures (B.4, B.5), the growth maps (growth rates found using Equation (B.54)) for different values for beam and background temperatures are shown (for two different sets of values for α and γ_b). Figure B.4, shows that at low background temperatures, the beam temperature parameters have a significant effect on the position of the maximum growth, i.e., the fastest growing wave-modes, and the spectral width of the unstable wave-modes. A small effect on the rate of maximum growth, however, this becomes more significant at more extreme parameters (lower α and higher γ_b). Figure B.5, shows that at higher background temperatures, the beam temperature parameters still have a significant effect the spectral width of the unstable wave-modes, and some what less significant effect on the position of the maximum growth, i.e., the fastest growing wave-modes. A small effect on the rate of maximum growth is also seen here, and this becomes more significant at more extreme parameters (lower α and higher γ_b) as before.

To approximately match the growth maps found by solve the dispersion relation found using the relativistic kinetic theory (which is much more complicated than the dispersion relation found here), it was argues in (Bret & Deutsch, 2006) that rescaling the beam temperature parameters can result in growth maps with the correct characteristics, the rescaling is done as follows

$$\begin{aligned} \theta_{b,\parallel} &= \theta_b^K/\gamma_b^3, \\ \theta_{b,\perp} &= \theta_b^K/\gamma_b, \end{aligned} \tag{B.57}$$

where θ_b^K is the temperature of the beam plasma in the background frame. We use this scaling to study the effect of the beam temperate θ_b^K on the maximum growth rate, the position of the maximum growing wave mode, and the full width half max of the unstable wave modes.

The maximum growth rates normalized with the cold-beam case, i.e., $\theta_b^K = 0$, is show in Figure B.6. The effect of the beam temperate parameters on the maximum growth rate are exaggerated when the background temperature is zero, this is much less significant when the background temperate is high since the background temperate has already reduced the growth rate with respect to the cold background limit as seen in Figure B.2.

The two panels of Figure B.7 show the effect of the beam temperature, θ_b^K, on the position of the fastest growing wave mode for cold (hot) background plasmas in the top

(bottom) panel for two different sets of values for α and γ_b. For cold background plasma, as the beam temperature increases, as was the case for the background temperate, the short unstable wavelength in the direction perpendicular to the beam (large $\hat{k}_y$) become stable and thus the position of the fastest growing wave significantly changes. On the other hand, when the background plasma temperature is high, the beam temperature parameters have a much less significant effect on the position of the fastest growing mode.

The effect of the beam temperate on the full width half max of the unstable region around the fastest growing wave mode in both directions (parallel to the beam on the right and perpendicular to the beam on the left) is shown in Figure B.8.

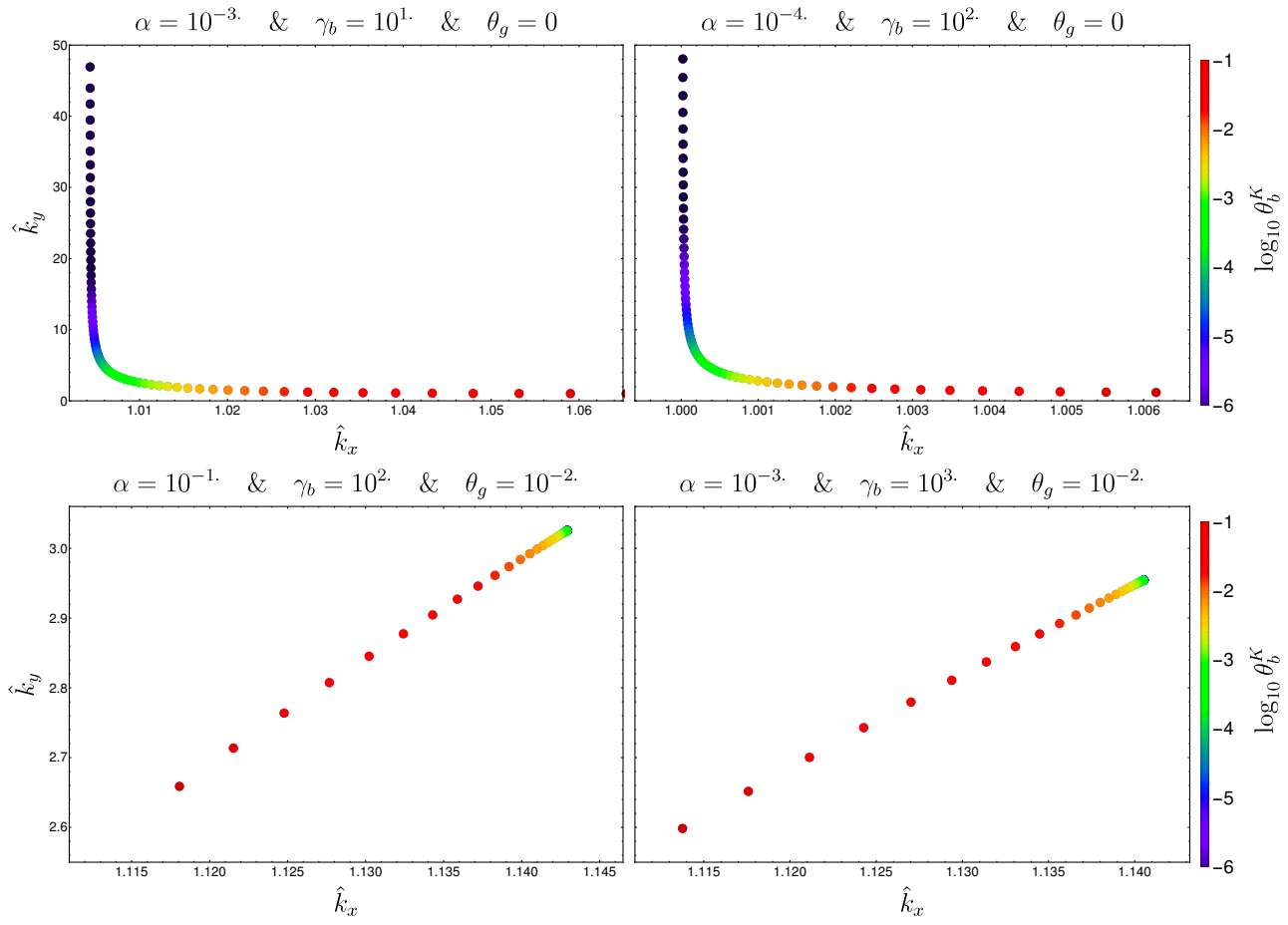

Figure B.7 The effect of the beam temperature, θ_b^K, on the position of the fastest growing wave mode for cold (hot) background plasmas in the first (second) panel for two different sets of values for α and γ_b. The beam temperature parameters are scaled differently in the parallel and perpendicular directions (with respect to the beam direction), see Equation (B.57).

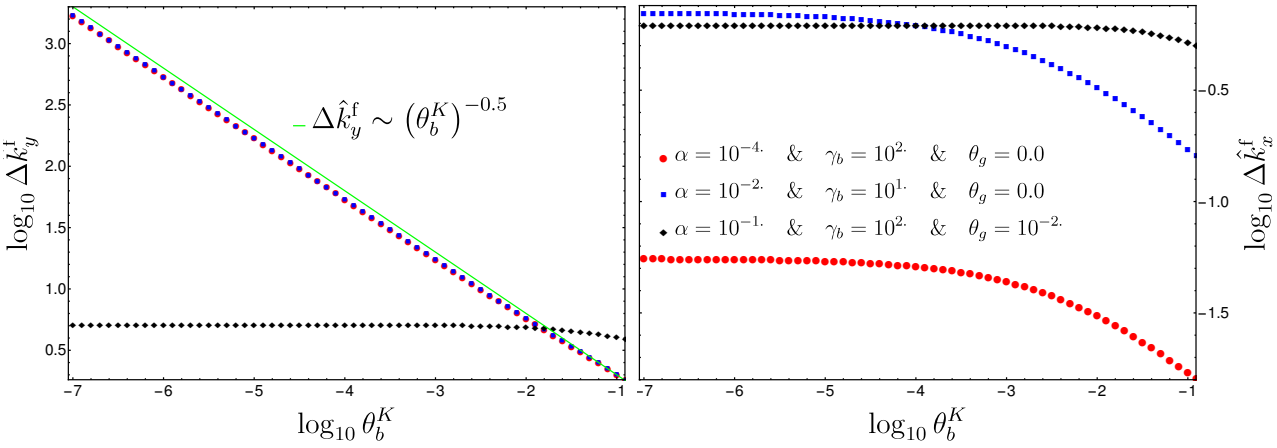

Figure B.8 The effect of the beam temperate on the full width half max of the unstable region around the fastest growing wave mode in both directions (parallel to the beam on the right and perpendicular to the beam on the left). The beam temperature parameters are scaled differently in the parallel and perpendicular directions (with respect to the beam direction), see Equation (B.57).